

AD-A193 752

RAPID-SCANNING FOURIER TRANSFORM SPECTROMETER FOR
STUDIES OF PROPAGATION O. (U) GEORGIA INST OF TECH
ATLANTA R A BOHLANDER ET AL. 01 MAR 88 GT-A-2632

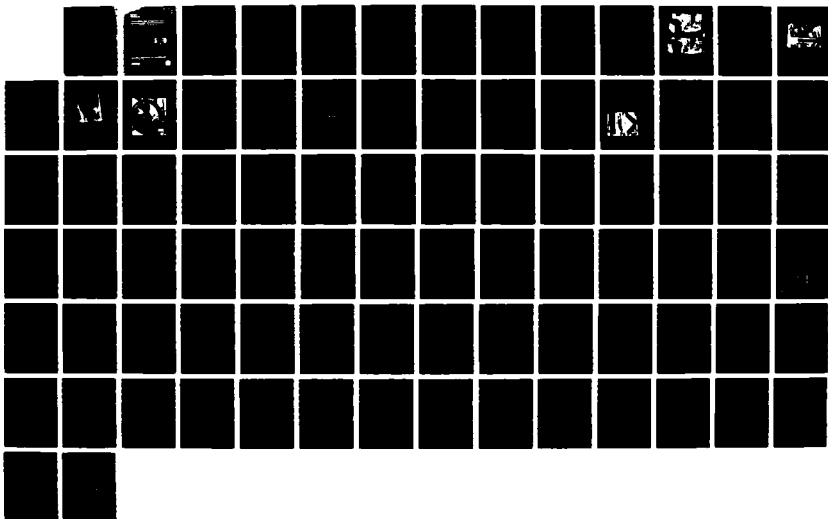
1/1

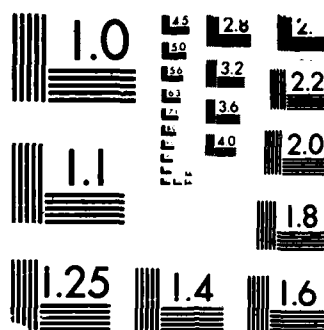
UNCLASSIFIED

ARO-17236. 5-G5 DARG29-88-K-0005

F/G 20/14

NL





MICROCOPY RESOLUTION TEST CHART
 (NBS 1963-A)

AD-A193 752

2

**RAPID-SCANNING FOURIER TRANSFORM SPECTROMETER
FOR STUDIES OF PROPAGATION OF NEAR-MILLIMETER-WAVE
RADIATION THROUGH CLEAR AIR AND FOG**

By

R. A. Bohlander, J. W. Larsen, D. R. Lamm
M. L. Blyler, D. E. Weeks, M. A. Gross, E. M. Ringer

Prepared for

U. S. ARMY RESEARCH OFFICE

P. O. Box 12211

Research Triangle Park, NC 27709-2211

Under

Contract Number DAAG29-80-K-0005

DTIC
ELECTE
APR 11 1988
S D

March 1, 1988

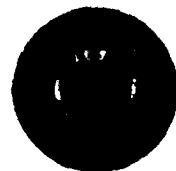
Approved for Public Release

Distribution Unlimited

GEORGIA INSTITUTE OF TECHNOLOGY

A Unit of the University System of Georgia
Atlanta, Georgia 30332

GTRI
GEORGIA TECH RESEARCH INSTITUTE



88 4 11 222

UNCLASSIFIED

SECURITY CLASSIFICATION OF THIS PAGE

A193752

REPORT DOCUMENTATION PAGE

Form Approved
OMB No. 0704-0188

1a. REPORT SECURITY CLASSIFICATION Unclassified		1b. RESTRICTIVE MARKINGS	
2a. SECURITY CLASSIFICATION AUTHORITY		3. DISTRIBUTION/AVAILABILITY OF REPORT Approved for public release; distribution unlimited.	
2b. DECLASSIFICATION/DOWNGRADING SCHEDULE			
4. PERFORMING ORGANIZATION REPORT NUMBER(S) A-2632		5. MONITORING ORGANIZATION REPORT NUMBER(S) AR4 17236.5-65	
6a. NAME OF PERFORMING ORGANIZATION Georgia Institute of Technology	6b. OFFICE SYMBOL (If applicable) GTRI	7a. NAME OF MONITORING ORGANIZATION U.S. Army Research Office	
6c. ADDRESS (City, State, and ZIP Code) Atlanta, GA 30332-0800		7b. ADDRESS (City, State, and ZIP Code) P.O. Box 12211 Research Triangle Park, NC 27709-2211	
8a. NAME OF FUNDING/SPONSORING ORGANIZATION U.S. Army Research Office	8b. OFFICE SYMBOL (If applicable)	9. PROCUREMENT INSTRUMENT IDENTIFICATION NUMBER DAAG29-80-K-0005	
8c. ADDRESS (City, State, and ZIP Code) P.O. Box 12211 Research Triangle Park, NC 27709-2211		10. SOURCE OF FUNDING NUMBERS PROGRAM ELEMENT NO. PROJECT NO. TASK NO. WORK UNIT ACCESSION NO.	
11. TITLE (Include Security Classification) Rapid-Scanning Fourier Transform Spectrometer For Studies Of Propagation Of Near-Millimeter-Wave Radiation Through Clear Air And Fog			
12. PERSONAL AUTHOR(S) R. A. Bohlander, J. W. Larsen, D. R. Lamm, M. L. Blyler, D. E. Weeks, M. A. Gross, E. M. Ringer			
13a. TYPE OF REPORT Final	13b. TIME COVERED FROM 4/28/80 to 9/30/87	14. DATE OF REPORT (Year, Month, Day) 3/1/88	15. PAGE COUNT 79
16. SUPPLEMENTARY NOTATION The view, opinions and/or findings contained in this report are those of the author(s) and should not be construed as an official Department of the Army position, policy, or decision, unless so designated by other documentation.			
17. COSATI CODES FIELD GROUP SUB-GROUP		18. SUBJECT TERMS (Continue on reverse if necessary and identify by block number) Propagation, Fourier transform spectrometer, interferometry, near-millimeter wave, rapid scanning	
19. ABSTRACT (Continue on reverse if necessary and identify by block number) A system has been developed to measure relative atmospheric transmission for the near- millimeter wave range of frequencies, 60-1000 GHz. A 400 m long propagation range has been established. A transmitter/receiver system at one end of a link incorporates a rapid-scanning Fourier transform spectrometer. It involves a novel mirror drive which moves both interferometer mirrors simultaneously. The interferometric section is a polarizing Martin-Puplett type. The grid polarizers are made photolithographically. The source is a hot mercury lamp in a cavity, and the detector, an InSb photoconductive element. Scans of 7.5 GHz resolution require about 0.2 sec. A dihedral retroreflector 200 m from the transmitter/receiver reflects the signal back and completes the link. Calibration spectra are obtained from a short path to a second retroreflector. System tests are described.			
20. DISTRIBUTION/AVAILABILITY OF ABSTRACT <input checked="" type="checkbox"/> UNCLASSIFIED/UNLIMITED <input type="checkbox"/> SAME AS RPT <input type="checkbox"/> DTIC USERS		21. ABSTRACT SECURITY CLASSIFICATION Unclassified	
22a. NAME OF RESPONSIBLE INDIVIDUAL		22b. TELEPHONE (Include Area Code)	22c. OFFICE SYMBOL

Table of Contents

1 INTRODUCTION	1
2 FOURIER TRANSFORM SPECTROMETER	2
2.1 Selection of Interferometer Type	2
2.2 Our Design	3
3 OPTICAL DESIGN	7
3.1 Transmit/Receive Layout and Polarization Control	7
3.2 Cassegrain Optics	11
3.3 Source	12
3.4 Interferometer Optics	12
3.5 Detector Optics	13
4 DETECTION	13
4.1 Detector Type	13
4.2 Dewar and Internal Optics	14
4.3 Preamplifier	14
5 ELECTRONIC CONTROL	15
6 CALIBRATION	18
7 ENERGY BUDGET	20
8 RESULTS	22
9 CONCLUSIONS	25
10 REFERENCES	26
11 APPENDICES	28
A Fabrication of Grids	28
B Theory of Grids	33
C Tests of Grids	48
D Papers Published	66

Accession For	
NTIS - GRA&I	<input checked="" type="checkbox"/>
ONIC - TAB	<input type="checkbox"/>
Unannounced	<input type="checkbox"/>
Justification	
By <i>per N.S.</i>	
Date <i>1/25/75</i>	
Availability Codes	
D-1	
A-1 25	

Table of Figures

1	Types of Martin-Puplett polarizing interferometer	3
2	Rapid-scanning Martin-Puplett type interferometer made at GTRI	4
3	Two views of the interferometer scanning mechanism	6
4	Side view of transmit/receive components	7
5	Photograph of transmit/receive components	8
6	Photograph of main retroreflector	10
7	Photograph of Cassegrain antenna	11
8	Diagram of internal detector optics	14
9	Block diagram of electronics in FTS	15
10	Initial servo-system functional diagram	16
11	Rapid scanning interferogram recorded with the initial servo-system	17
12	Rapid scanning interferogram recorded with manual scanning	18
13	Photograph of calibration retroreflector	19
14	Spectrum obtained by Fourier transformation	24

1 INTRODUCTION

At the outset of this work, a controversy had begun concerning the near-millimeter-wave (NMMW) transmission of the atmosphere. Observations of attenuation, then and since, have been reported [e.g. 1-3] which are higher than anything attributable to accepted theory. Absorption in this region, between 90 and 1000 GHz, comes primarily from rotational lines of water vapor. While it is difficult to predict absorption in the wings of lines, the referenced observations were particularly anomalous in one or more respects:

1. *Attenuation per unit water vapor concentration seemed to increase with decreasing temperature much faster than expected.* Energy levels in the water molecule and expected intermolecular interaction energies could not account for the results.
2. *Absolute attenuation coefficients were very large at frequencies between water lines where low attenuation was expected.* Instances of this occurred during conditions of high humidity, fog, and/or low temperatures. Values of extra absorption around 10 dB/km or higher, if correct, would have an adverse effect on applications of the NMMW band.
3. *Discrete absorption features appeared which were not at frequencies of known water lines or of other known atmospheric constituents.* Spectroscopic studies of pure water vapor under carefully controlled laboratory conditions have not shown such features, thereby eliminating possible equilibrium concentrations of water dimers as a potential explanation [4,5].

Although oxygen, ozone, and various trace species also absorb in this region, such phenomena cannot be assigned to them and have been termed "anomalous absorption". It has been suggested that exotic polymers of water might be responsible [2]. On the other hand, contrary results have also been reported [e.g. 6,7], and assertions made that there were errors in those observations in which anomalous absorption appeared. These matters are covered in greater detail in a review [8] published during the course of this work and included in Appendix D of this report.

The purpose of our current work was to prepare new instrumentation for improved observations of atmospheric absorption under conditions purported to be associated with anomalous phenomena. We chose a spectroscopic technique, rather than single frequency transmissions, so we could look for anomalous absorption features like those described in 3. above. The ability of the atmosphere to change significantly during time intervals of the order of a few minutes can have a significant effect on accuracy in recording spectra. Distortions due to atmospheric changes were one of the possible sources of errors cited by critics of anomalous absorption. This consideration was a primary factor in our instrumental design.

There are two basic approaches to spectroscopy in the NMMW band. Spectra can be obtained from tunable narrow-band sources. Due to their relatively high power, good signal-to-noise ratios can be attained at any given frequency. However, there is often a significant amount of time and effort devoted to tuning so that it is difficult to get a high resolution spectrum in a time which is short compared with that taken by some changes in the atmosphere. The alternative is Fourier transform spectroscopy. The disadvantage here is that wide-band, black-body sources are relatively weak. Even with a sensitive liquid-helium-cooled detector, long integration times are required. If a long time is spent recording each sequential point of the interferogram, then the total record time may be minutes to hours. During this time any changes in atmospheric transmission will have the effect of a modulation on the interferogram and will, to some degree, distort the spectrum, which is obtained by Fourier transformation. However, all frequencies are received at all points in the interferograms recorded (the multiplex advantage), and rapid-scanning techniques to obtain interferograms in a few

seconds have been devised for use at infrared wavelengths [e.g. 9,10]. When integration times of a few minutes are required to build up the signal-to-noise ratio, multiple interferograms or spectra can be averaged. Then, although the result is an average over that period of time, each spectrum in the average is practically undistorted by atmospheric change.

We elected to extend rapid-scanning FTS techniques to the NMMW band as the best way to look for all three purported aspects of anomalous absorption. In addition, we have incorporated polarizing beam splitters in the Fourier transform spectrometer (FTS) which offer much improved efficiency over ones used previously in transmission measurements. The complete system described in this report is designed to make transmission measurements over a novel two-way, 400 m path. A liquid-helium-cooled InSb detector with a short response time is incorporated. Partial tests of the instrumentation will be described, but difficulties with the detector have made it not possible to obtain atmospheric transmission measurements as of the time of writing.

2 FOURIER TRANSFORM SPECTROMETER

2.1 Selection of Interferometer Type

A two-beam interferometer (like a Michelson interferometer) is an efficient way to obtain interferograms from which spectra of signal intensity are derived by Fourier transformation. Unlike a grating spectrometer with slits, the input and output apertures can be large to promote throughput of radiation.

The history of interferometer development in the NMMW band is marked by improvements in the beam splitter. An ideal beam splitter, divides the input beam into two beams of equal intensity. Thin metal films cannot be used here due to absorption. Michelson interferometers first appeared with thin, plastic film beam splitters [11]. However, such films had less than ideal reflectivity, absorption losses, and troublesome gaps in efficiency caused by interference within the films [12]. Moreover, the angle of incidence of radiation to the films was often close to Brewster's angle, so one plane of polarization was not effectively split. In 1969, Martin and Puplett [13] introduced a type of interferometer that also restricted throughput to one plane of polarization but incorporated a beam splitter with nearly ideal performance.

This was achieved with a wire grid beam splitter that reflects one plane of polarization and transmits the orthogonal one. The reflection and transmission of the two polarizations approach ideal if the period of the grid lines g is much less than the wavelength λ . (See Appendix B.) When the grid lines are oriented at 45° with respect to the input polarization, such a beam splitter can divide the radiation into two beams of nearly equal intensity. While early grid beam splitters were made by stretching fine wires across a frame, we have since found [Ref. 14 and Appendices A-D] that high performance can more reliably be obtained with a pattern of metal strips etched on a thin plastic substrate. When the substrate is very thin with respect to λ , it is essentially invisible. Beam splitters of this type are used in the system described here.

Many versions of the Martin-Puplett polarizing interferometer have been described, two of which are illustrated in Fig. 1. Part a. shows a version with separate input and output beams like those in a traditional Michelson interferometer. The output beam takes a different direction due to the rotation of polarization caused by the dihedral mirrors [13]. Part b. shows what happens if the mirrors are planar: the output radiation goes back in the direction of the input and must be separated out with another polarizing beam splitter used as an analyzer.

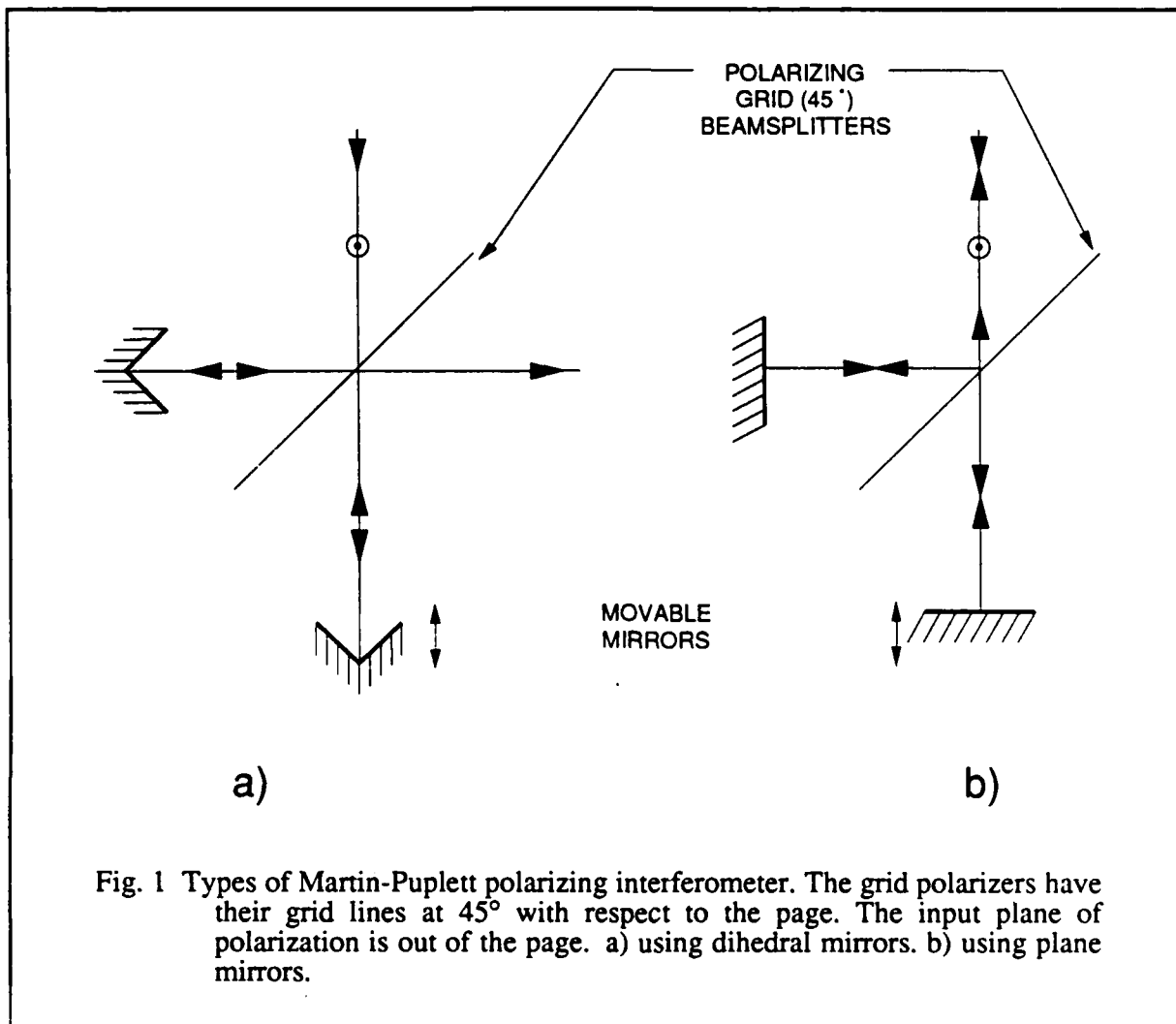


Fig. 1 Types of Martin-Puplett polarizing interferometer. The grid polarizers have their grid lines at 45° with respect to the page. The input plane of polarization is out of the page. a) using dihedral mirrors. b) using plane mirrors.

While separation of input and output beams is a nice feature of the layout in Fig. 1a, dihedral mirrors are difficult to align optically. One axis of tilt and the orientation of the dihedral roof line about the optic axis must be adjusted. The simpler system in Fig. 1b is preferred for rapid scanning [15] so that complex alignments do not complicate the delicate high speed mirror drive(s). With this design, two axes of tilt for one mirror must be aligned with respect to the other so that wave fronts returning from both mirrors will be parallel in the output beam. However, as will be seen, this function can be performed by auxiliary, non-moving mirrors. Our design for a rapid-scanning interferometer has some novel features but is closely related to the design shown in Fig. 1b.

2.2 Our Design

The arrangement of mirrors and beam splitter used in our design is shown in Fig. 2. The mirror drive is somewhat novel for this type of interferometer in that one mirror in each beam, M3 and M4, is moved. The mirrors move in opposite directions, since they are mounted on opposite sides of a parallelogram formed by the mirror carriers and the levers L1 and L2. Each

lever pivots in the middle with respect to the main interferometer drive base, which is shown. The ends of the levers connect to the mirror carriers also through pivots. The angle of L2 can be changed by the torque motor whose armature is attached to the lever and whose field is attached to the base. As a result, the scanning mirrors move in such a way that the plane of each reflecting surface is always parallel to the initial plane, and the path difference between the beams is four times the displacement of one of the mirrors from the position where they are coplanar.

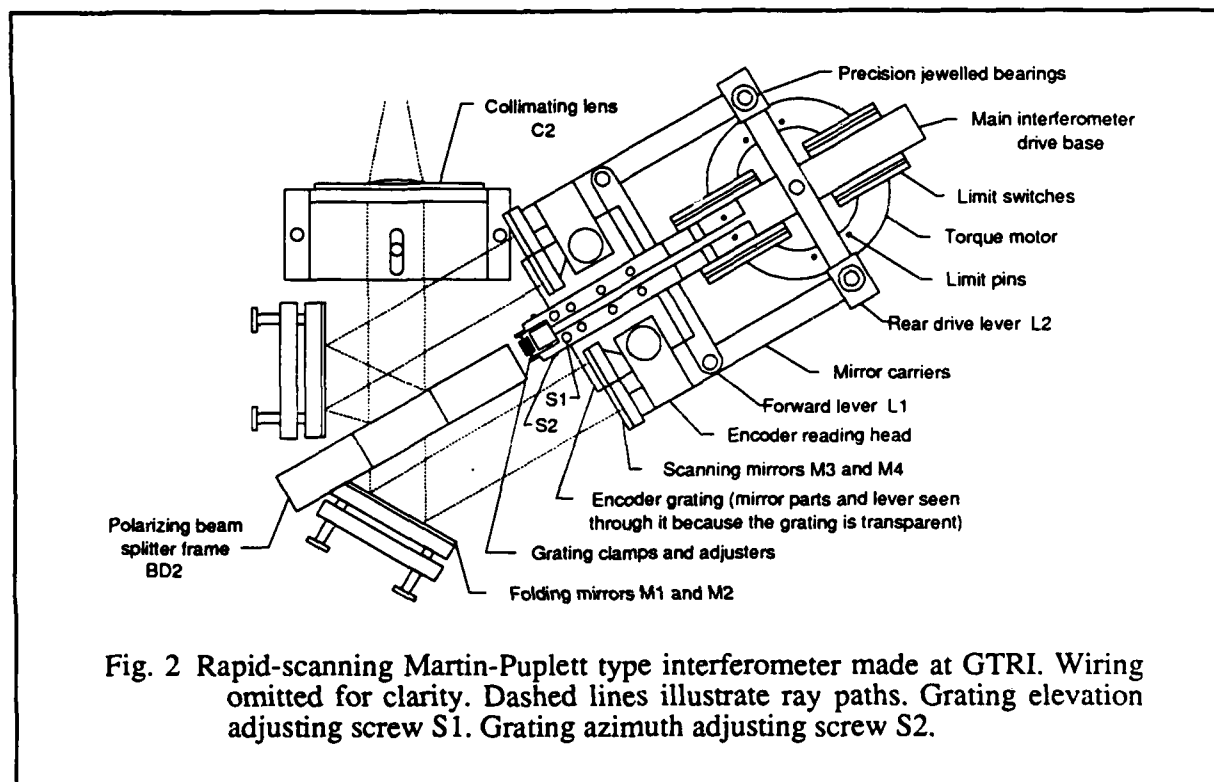


Fig. 2 Rapid-scanning Martin-Puplett type interferometer made at GTRI. Wiring omitted for clarity. Dashed lines illustrate ray paths. Grating elevation adjusting screw S1. Grating azimuth adjusting screw S2.

Path differences up to 8.2 cm can be achieved with an angular rotation of about 20° . This makes a fairly compact drive for such a resolution. It is also well-balanced which is important for keeping vibration down in rapid scanning. Mirror speeds up to 5 cm/sec can be obtained with the servo-control. For spectroscopy near sea level, absorption lines in the transmission spectrum of the atmosphere over a 400 m path are generally of a such a width that 7.5 GHz resolution is adequate. This corresponds to a path difference of 4 cm and a mirror displacement of 1 cm. Thus, a spectrum can be obtained in around 200 msec.

The mechanism of this drive has some antecedents. It is similar to a design for translating a single mirror in an interferometer developed at AFGL [9,10]. In this, only one mirror was translated by levers on one side of the base. The mirror also had a shorter range of travel since the pivots were a torsional type limited by strain failure. We tried to use a similar pivot (a model 2479167-Z Flex Pivot made by Bendix, Electric Fluid and Power Div.) which was more flexible and able to reach $\pm 25^\circ$ with indefinite life, provided there was zero load. Such pivots were attractive because there is practically no friction involved, but they proved too flexible in two respects: 1) they could not hold the armature in the center of the stator of the torque motor, and 2) the scanning motions created destructive resonant vibrations in the flexible pivots. For these

and other reasons, we found it necessary to replace the pivots with jeweled bearings and pivots, which we made to a tolerance of about $8\text{ }\mu\text{m}$ (0.0003 in). A light-weight lubricant (Synt-A-Lube, made by H. Molbius in Switzerland) was used for acceptably low friction.

As may be seen in the photographs in Fig. 3, the levers L1 and L2 connect to the base and to the mirror carriers with a top and bottom bearing/pivot set, with one exception: only one bearing/pivot is used to connect L2 and the mirror carriers. These have a special arrangement to allow for an important adjustment. If one tries to assemble the scanning mechanism without making allowance for possible imperfections in machining the parts, a bearing/pivot set might not fit in the last joint or might be seriously strained. To alleviate this, it is necessary to have some adjustment in the length of at least one of the levers or mirror carriers. However, this is not necessarily satisfactory since the assembled parts may not then form a parallelogram, and parallel motion of the mirrors may be lost. Parallelograms can be obtained on both sides of the drive if an adjustment can be made in the length of both mirror carriers and both sides of the lever L2. The adjustment is made in each case by moving the hole in which the bearing or pivot fits at the back of the mirror carriers and ends of L2. This hole is made to be the inner hole of two nested collets which are each slightly and equally eccentric. By rotating the collets with respect to the mirror carrier or lever, one can move the center line of the hole. When a position is found that makes the mirrors move properly and which relieves strain, the collets are clamped. The advantage of this method is that it resists loosening during scanning.

Motion of the mirrors is monitored by special optical grating encoders made by Teledyne Gurley. The gratings, one on each side, are mounted to the interferometer base as shown in Figs. 2 and 3, and the two reading heads to the mirror carriers. The gratings have an envelope which is a shallow arc corresponding to the arc of the levers. (While the mirrors move so that the reflecting plane is parallel to its starting position, the reader will notice that the mirrors move in and out slightly from the interferometer base due to the arc taken by the ends of the levers. The mirrors are large enough that they always reflect the radiation beams in the interferometer, so this is not a problem.)

The period of the grating in the Teledyne Gurley encoders is $20\text{ }\mu\text{m}$, and with the conditioning electronics, an electrical pulse can be derived for every $5\text{ }\mu\text{m}$ of motion of the reading head. These interpolated pulses are triggered by the zero-crossings of the two differential channels in quadrature. The accuracy of encoding depends essentially on two factors: (1) the fundamental accuracy of the ruling of the grating, and (2) the accuracy with which mechanical and electrical adjustments can be made to achieve both a uniform duty cycle between zero-crossings and the phasing between the channels nominally in quadrature. In practice, the latter controls the accuracy achievable, and the manufacturer estimates that this is about $\pm 2\text{ }\mu\text{m}$. At $\pm\lambda/150$ for the shortest wavelength of possible interest, this degree of accuracy is adequate. Encoder gratings are attached as shown in Figs. 2 and 3, and adjustments are provided for alignment of the gratings with the mirrors and with the the reading heads. Measurements from the encoders from both sides of the drive are used in reckoning path difference.

Folding mirrors M1 and M2 are provided so that the two moving mirrors can be parallel to each other instead of perpendicular, as in a conventional interferometer. These mirrors also make it possible to align the interferometer in the sense of bringing the output beams from the two moving mirrors into coincidence. This is tested by shining a helium neon laser into the input port and checking that the return beams are in coincidence on some distant target. Diffraction from the grid beam splitter is not a problem since the zero-order spots are quite distinct. In fact the diffraction patterns are useful in insuring the correct orientation of the grid lines.

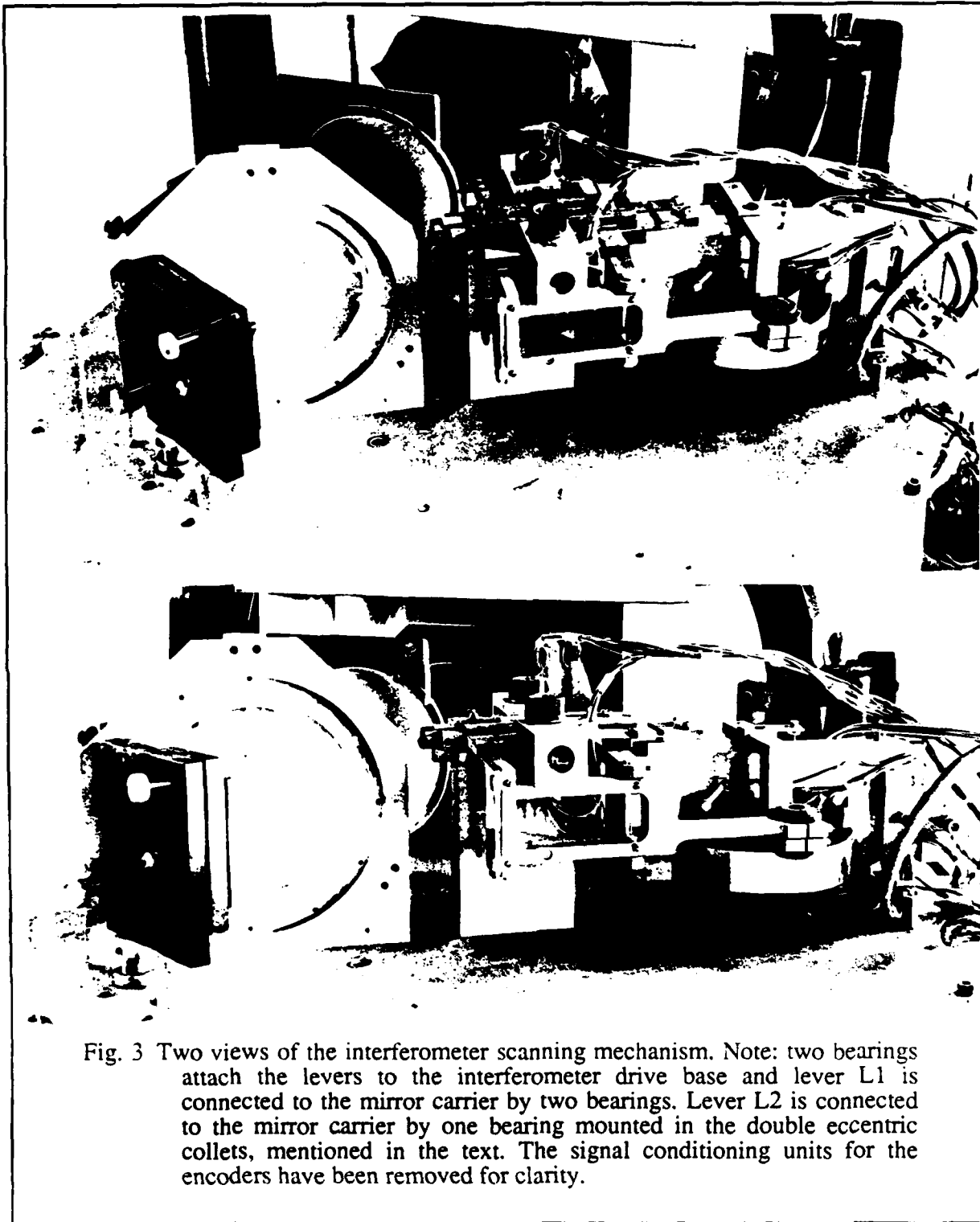


Fig. 3 Two views of the interferometer scanning mechanism. Note: two bearings attach the levers to the interferometer drive base and lever L1 is connected to the mirror carrier by two bearings. Lever L2 is connected to the mirror carrier by one bearing mounted in the double eccentric collets, mentioned in the text. The signal conditioning units for the encoders have been removed for clarity.

3 OPTICAL DESIGN

3.1 Transmit/Receive Layout and Polarization Control

An input/output polarizing beam splitter is an important ingredient, in addition to those shown in Fig. 2, for proper operation of the interferometer. This component, shown in Figs. 4 and 5, has three functions: (1) it establishes an input plane of polarization, (2) it acts as a polarization analyzer for the output from the interferometer, and (3) it makes it possible to have a monostatic antenna (for transmitting and receiving signals). This was important in making it easier to implement a short path for calibration (see Section 6).

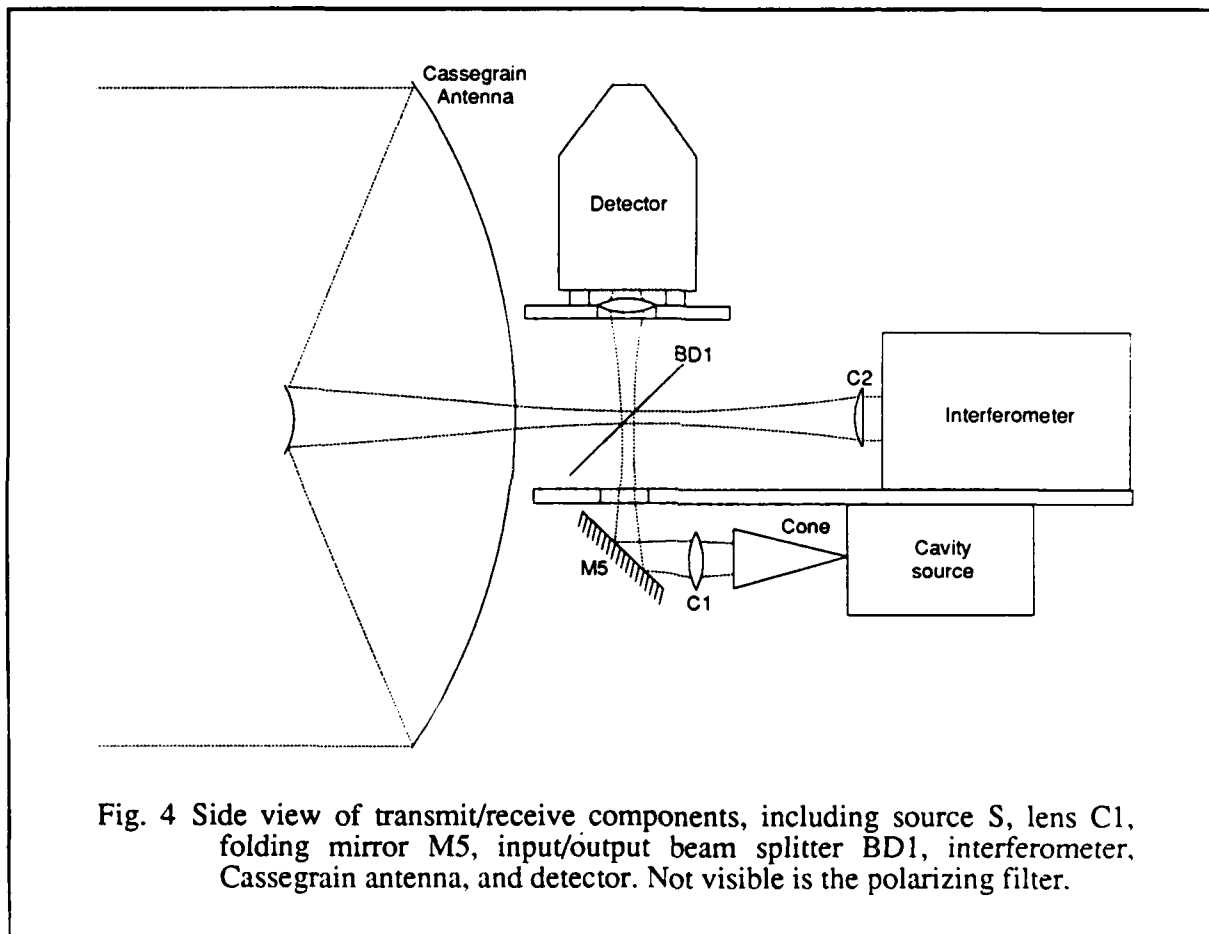




Fig. 5 Photograph of transmit/receive components

The signal from the lamp source is focused and reflected up to the input/output beam splitter. There, one plane of polarization, at 45° with respect to a vertical line, is reflected into the interferometer. The beam splitter in the interferometer has vertical grid lines, so that half the incoming radiation is split to each of the sides of the interferometer. The same polarizations return from mirrors M3 and M4. When they recombine at beam splitter BD2, there is a phase delay between the beams proportional to the path difference. When the phase difference for a given wavelength is zero or a multiple of 2π , the resultant polarization going back out the interferometer is the same as the input. For phase differences which are odd multiples of π , the outgoing polarization is perpendicular to that in the input. For intermediate phase differences, the polarization is elliptical or circular. Regardless, the input/output beam splitter acts as an analyzer: it passes only polarizations perpendicular to that from the input. With a conventional

interferometer, the output signal at zero path difference is a maximum. For the interferometer described here, interferograms are inverted but this has only a trivial effect on the extraction of spectra by Fourier transformation.

The signal leaving the input/output beam splitter has a polarization which is once again at an angle of 45° with respect to the vertical. This signal, which passes out through the Cassegrain antenna, propagates from one building to another on the Georgia Tech campus over a path 200 m long. At the end of this path, a dihedral retroreflector has been sited. Shown in Fig. 6, its roof edge is horizontal so that the plane of polarization is rotated by 90° . The retroreflector is aimed back at the transmitter/receiver where the radiation is collected by the Cassegrain antenna. The signal returns to the input/output beam splitter where it is now reflected upwards to the detector. In order for the detector to see this signal alone, a polarization filter is provided, made from two polarizing grids. Otherwise, the detector would see a large signal directly from the source. While this signal is unmodulated by the interferometer, it might overload the detector if not removed.

The retroreflector has been made from Hexcell TM honeycomb aluminum plates which were found to be flat to a few thousandths of an inch, adequate for the NMMW region. They were mounted in a machine jig to insure squareness of the roof intersection. Proper retroreflection has been verified by clamping plate glass mirrors to the retroreflector surfaces. The retroreflector assembly has been mounted to a specially constructed, large tripod assembly, which has been reinforced with guy wires and shielded from wind and weather by a scaffold clad with tarpaulin.

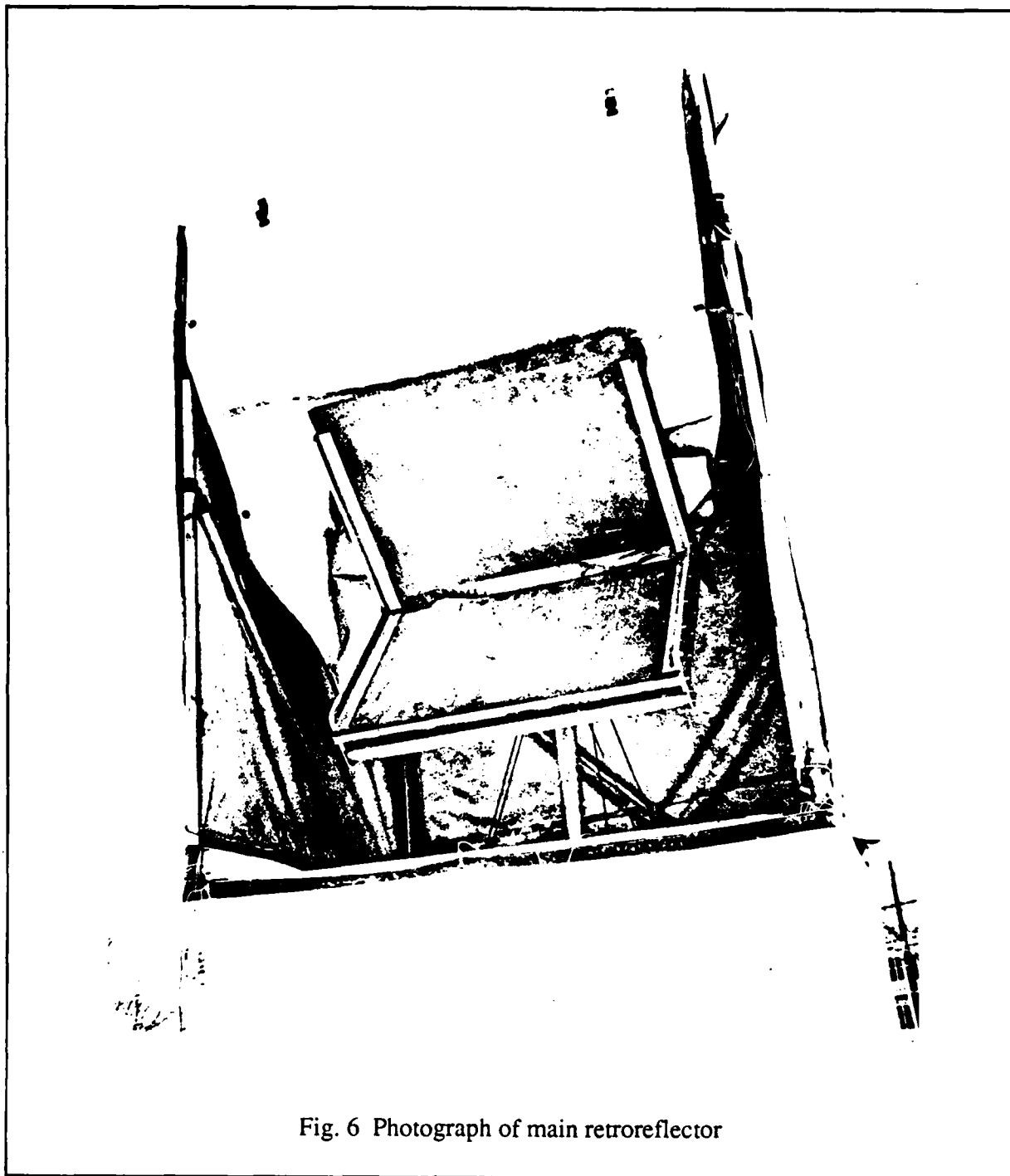


Fig. 6 Photograph of main retroreflector

3.2 Cassegrain Optics

The Cassegrain antenna consists of a 630 mm diameter electroformed primary paraboloid, with a focal ratio $f/0.28$, and a 132 mm diameter secondary hyperboloid. A photograph is given in Fig. 7. The surface of the mirror is nickel, over-coated with rhodium, chosen for weather resistance. The secondary was a nickel-coated aluminum mirror which was diamond turned by Aero-Research Corporation. This combination provided optically polished surfaces so that the antenna could be aimed at the remote retroreflector using optical images.

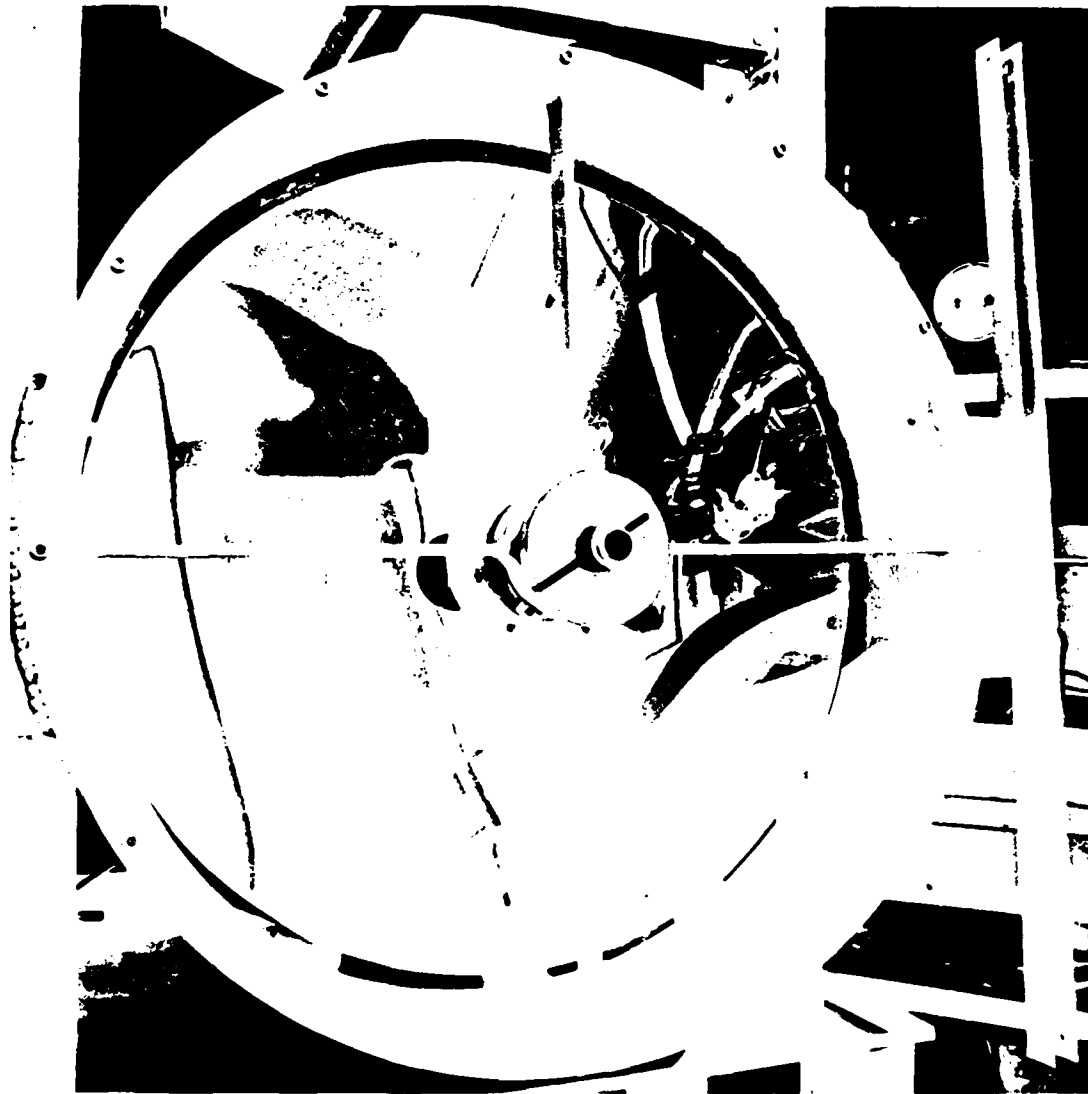


Fig. 7 Photograph of Cassegrain antenna

Construction of this type of antenna requires some care since the electroformed primary is relatively thin (0.08 in, 2 mm). With the advice of the maker (Optical Radiation Corp.), we mounted the primary in a shell that supported the back of the mirror at about 2/3 the diameter of the mirror. We fastened it to the shell using a specially selected silicone adhesive recommended as likely to minimize stress on the mirror. The shell in turn supported the secondary mirror with conventional spars. Since it was impossible to guarantee that the primary would be located accurately with respect to the secondary holder, the latter was provided with adjustments, both for centering and for tilt. Subsequent tests, however, showed that the primary had been accurately positioned and that adjustments from the neutral position of the secondary were not necessary.

The whole antenna subsystem is mounted in an Aerotech gimbal with micrometer adjustments for aiming. We built a pulley counterbalance system to stay within the static torque limitations of the gimbal.

3.3 Source

The source of radiation used in the system is a hot mercury lamp mounted in a cavity with a conical horn (or cone channel) output. Such lamps have been found to radiate in the NMMW band like a black body of 2000K [16]. The cavity is 127 mm (5 in) in diameter and integrates the signal from all parts of the lamp into an apparent source about 5.3 mm (0.25 in) in diameter at the output port of the cavity. The surface of the brass cavity has been gold-plated for high reflectivity at NMM wavelengths.

The copper electroformed cone has apertures of 5.3 mm and 43 mm and a length of 116 mm. It serves two purposes: 1) it restricts radiation to cone angles which just fill the optical train after the source, and 2) it makes the source appear to be larger in diameter [17] so that the image of the source projected on the retroreflector is large enough to fill it. We have estimated the apparent size of the source to be 33 mm in diameter and the image at the remote retroreflector to be 3.5 m in diameter. There is some vignetting expected near the outer part of this due to the sizes of the optical elements, but the central 1.6 m of the image should be free of vignetting.

As shown in Figs. 4 and 5, there is a 70 mm diameter relay lens after the cone to place an intermediate focus of the source on the input/output beam splitter BD1. The lens is double convex (hyperboloid) and made of TPX®, a plastic selected for its low losses in the NMMW band and for its transparency. The hyperboloid surfaces were made with the usual eccentricity (equal to the refractive index) [18] to minimize spherical aberration for on-axis radiation.

3.4 Interferometer Optics

The collimating lens C2 in the interferometer has an interesting dual role: 1) it forms a nearly parallel beam of radiation for entry into the interferometer, and 2) it controls the quality of the quasi-collimation by the Cassegrain antenna. It is a plano-convex (hyperboloid) lens made of TPX® and is 100 mm in diameter.

Collimation to the interferometer is not perfect due to diffraction and to the extended size of the source. Since the optical path lengths in the interferometer are not large and since the ratio of aperture to wavelength is generally better than 50:1, diffraction will be neglected in the interferometer. The mirrors of the interferometer are, however, somewhat over-sized to accommodate a small amount of diffraction. The effect of the extended source is to cause the

beam envelope in the interferometer to decrease from an approximate diameter of 83 mm at C2 to a diameter of 45 mm in the vicinity of the moving mirrors M3 and M4. The reason for this is that these mirrors were placed near a pupil which is the image of the antenna aperture behind C2.

In initial designs of the lens C2, the surface was hyperboloid with the usual eccentricity to minimize axial aberration [18]. However, it is known that off-axis, such aspheric surfaces can actually cause aberrations to be worse than for the case where spherical lens surfaces are used [19]. In our optical system there are many optical elements in the train before the beam which propagates to the retroreflector. To estimate the effects of aberration, we used computer ray tracing. We attempted to focus the Cassegrain so that there was an image formed of the source on the retroreflector. We observed that the image field was drastically curved: the position of focus for the apparent edge of the source was at 148 m range, as compared with 200 m, on axis. This might create a little wash out of the image near the edges of the retroreflector so we devised a correction. We made the eccentricity of the hyperboloid somewhat smaller, until by trial and error, the aberrations were negligible. The final eccentricity was 0.87 n , instead of the usual n , where n is the refractive index, 1.458, for TPX®. It is interesting that it was possible to correct the image curvature by adjusting the surface of only one element in a simple way. A theoretical analysis [20] of third-order aberrations in the system showed that this plano-convex lens, which radiation passes through twice, was the primary cause of the field curvature, and the special circumstances of the layout led to a fortuitously simple solution.

3.5 Detector Optics

The optics leading to the detector from the input/output beam splitter BD1 consist of a 36 mm diameter TPX® lens for relaying the signal from the retroreflector and two polarizing filters to block direct radiation from the source. The window of the detector is 13 mm in diameter.

4 DETECTION

4.1 Detector Type

The lowest noise detectors sensitive over the NMMW range at the time this work began were liquid helium-cooled composite bolometers, based on Germanium [21]. Minimum detectable power values (for a radiation band 0-1000 GHz) can be around $NEP=10^{-14} \text{ W/Hz}^{1/2}$. Regrettably, these detectors cannot be used in this application because their response rolls off at frequencies above (typically) tens of Hz. For rapid scanning of the shortest wavelengths that might be seen here, the interferometer could produce modulations of signal as high as 150 Hz in frequency. The upper limit of the detector modulation frequency response should be significantly higher to avoid phase shifts. Hot-electron InSb photoconductive detectors, on the other hand, have modulation frequency responses up to at least 500 kHz, but a higher noise level. For operation at liquid-helium temperatures, NEP values around $10^{-12} \text{ W/Hz}^{1/2}$ have been reported [22]. Values of this order can be shown to be the minimum necessary to obtain spectra in reasonable amounts of total measurement time, as discussed in Section 7.

Obtaining a working InSb detector with such sensitivity proved to be difficult during the contract period. Georgia Tech owned InSb elements at the start of the work of unknown sensitivity. These proved to be significantly less sensitive than Golay cells, which usually have NEP values of 10^{-9} to $10^{-10} \text{ W/Hz}^{1/2}$. We then were grateful to obtain an element through MICOM and learned to contact it to the post which holds it in our detector cavity. The resulting sensitivity was better but not adequate to see the source signal over the 400 m path. After recontacting the element several times, the best that we achieved was $2.4 \times 10^{-11} \text{ W/Hz}^{1/2}$ (see Section 8), not

sufficient to conduct the experiment. We attempted to improve our technique by contacting the element in a reducing atmosphere but this was unsuccessful. Nevertheless, it is still believed possible to obtain a detector with the necessary sensitivity, particularly, since new sources for detector elements have appeared in the U.S. since the work began.

4.2 Dewar and Internal Optics

The detector element used has been mounted in a standard Infrared Laboratories dewar with a downward looking window, as shown in Fig. 8. The detector element is contacted to a post within a gold-plated beryllium-copper cavity which is fed by a small horn. A fine wire to the other side of the element completes the circuit to the preamp.

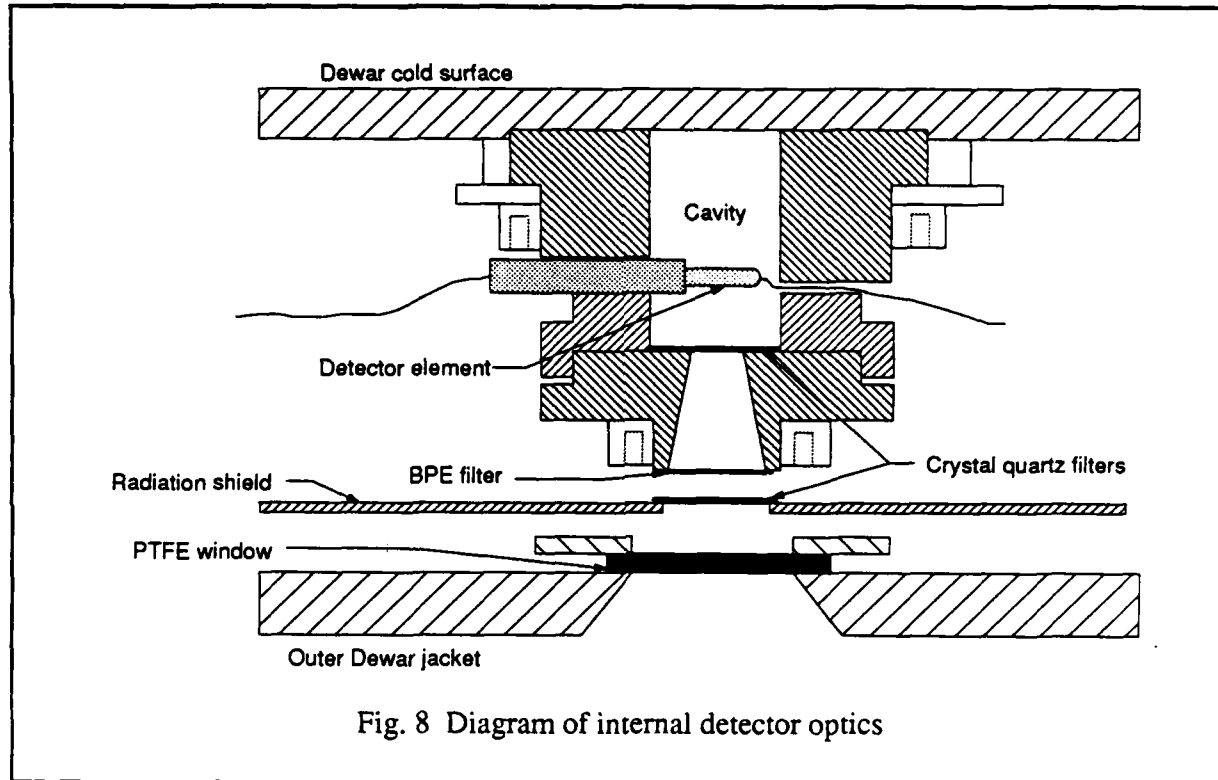


Fig. 8 Diagram of internal detector optics

It is necessary in Fourier spectroscopy to have a low-pass optical filter to prevent aliasing of high frequency signals in the region of interest. InSb elements have a natural roll off at around 1000 GHz. However, it is necessary to remove higher frequencies in the infrared where the element can be sensitive. Accordingly, black polyethylene and crystal quartz have been mounted on the radiation shield of the detector dewar and on the detector cavity. The external detector window is made of PTFE.

4.3 Preamp

A standard low-noise FET preamplifier with three stages and a gain of 300 has been used with the detector. The noise figure of the amplifier was tested to be 1.8 $\text{nv/Hz}^{1/2}$. This compares favorably with 3 $\text{nv/Hz}^{1/2}$ typical of such preamps.

5 ELECTRONIC CONTROL

The electronics subassemblies prepared for the FTS are diagrammed in Fig. 9. Many of the electronic systems involved were developed concurrently for this program and for research for AFGL. The interested reader may consult [23,24] for detailed information on the circuits and on common optical elements. Control of the interferometer is separated into two sections, a primarily analog section, called "Head Electronics", near the interferometer, and a primarily digital section, called "Control Electronics", which can be several feet away.

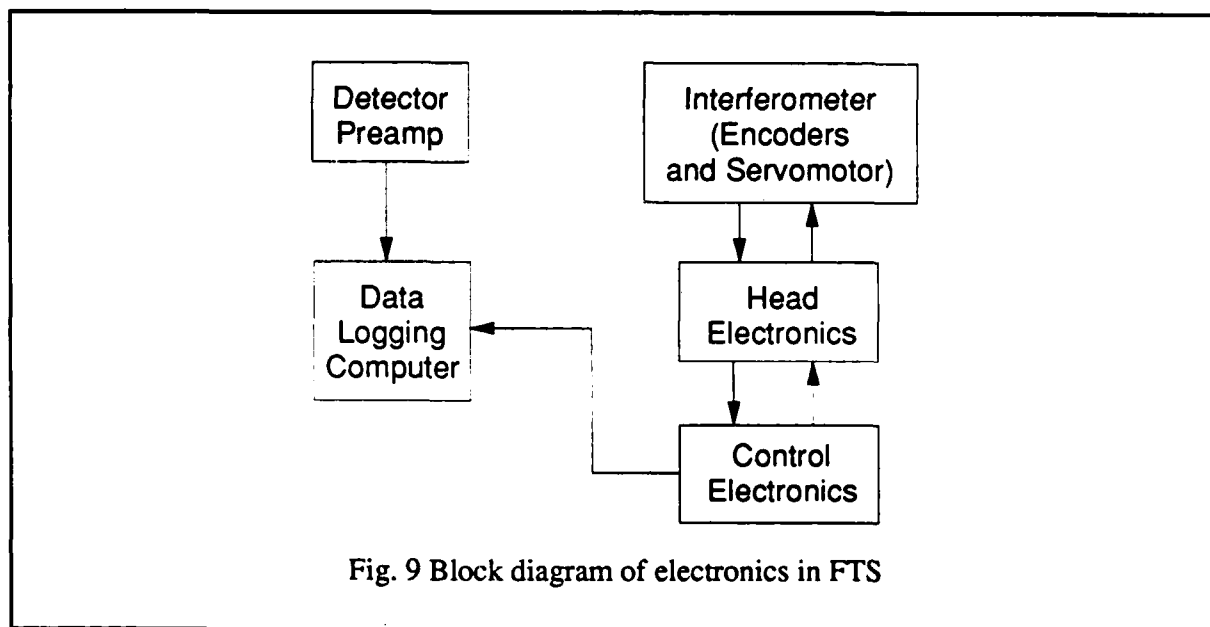


Fig. 9 Block diagram of electronics in FTS

Two Motorola 6809 microprocessors are contained in the Control Electronics chassis, one responsible for servo-control and one for monitoring keyboard inputs which set various control parameters. The circuits in the Head Electronics, in conjunction with the Control Electronics, implement a hybrid analog/digital servo-system for accurate control of the moving mirrors. The primary mode of operation drives the mirrors at a constant speed until a predetermined path difference is reached and then the motion is reversed. The servo-control circuitry supplies a control voltage to a power servo-amplifier used as a voltage controlled current source (VCC) which supplies current to the torque motor. The mirror position is determined by the pair of incremental position encoders, whose conditioning electronics closes the feedback loop by supplying information to the position counter. The position counter supplies position information to the servo-loop control circuitry and to the control processor.

Fig. 10 gives a functional block diagram of the servo-system that has been implemented. In the initial design, the servo-loop controller was directly connected to the servo-amplifier. Late in the research effort it was discovered that the digital feedback of position and velocity implemented by this system caused a grainy signal to be transmitted to the torque motor. As a new byte of position or velocity information was received, the torque motor was asked to make a small step response. This let the motor to radiate a great deal of interference which was picked up by some part of the sensitive detector system. As a result, interferograms had an interference component superimposed, as shown in Fig. 11.

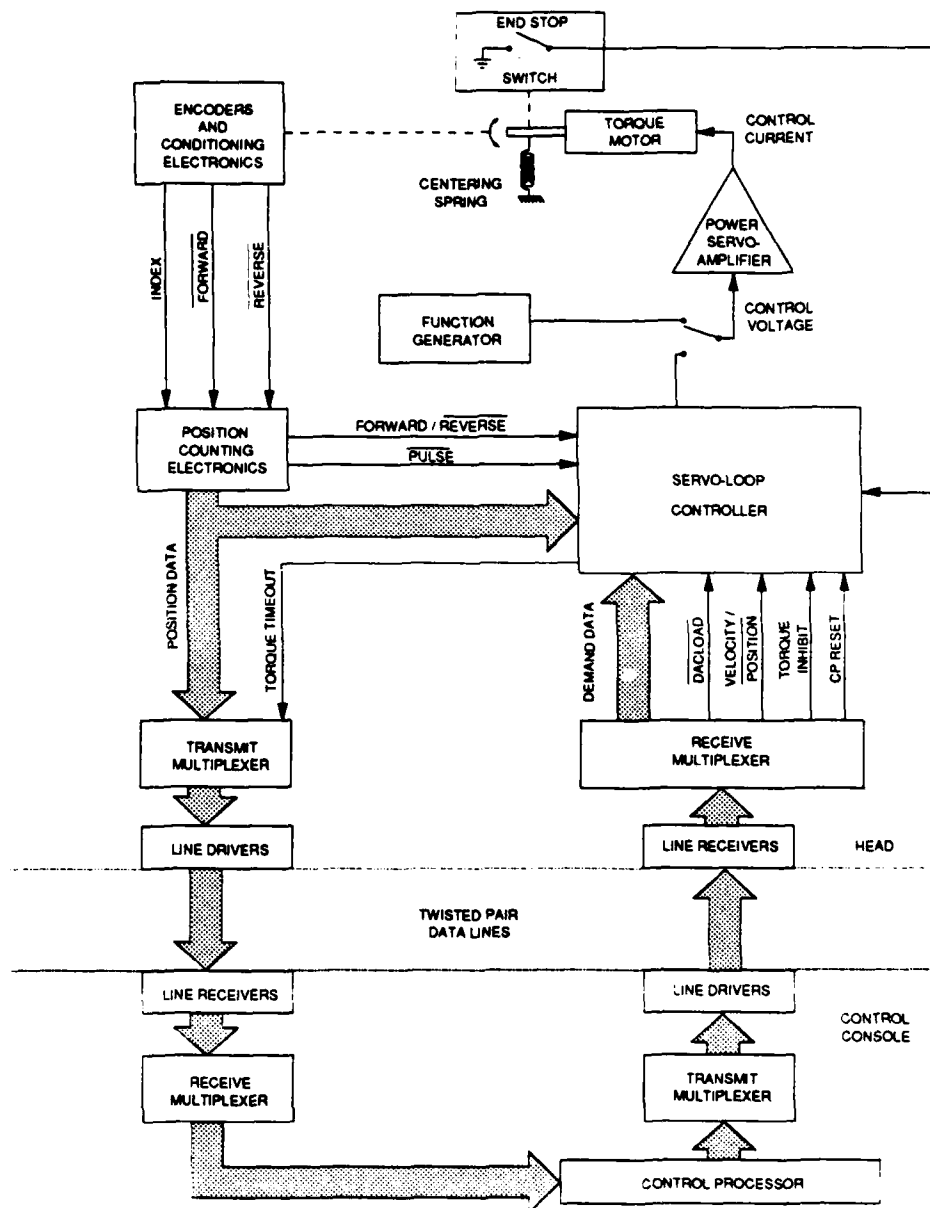


Fig. 10 Servo-system functional diagram. In the upper right corner, there is a switch to connect either the servo-loop controller or a function generator to the power servo-amplifier. In the initial design the servo-loop controller was connected and later designs connected the function generator, as explained in the text.

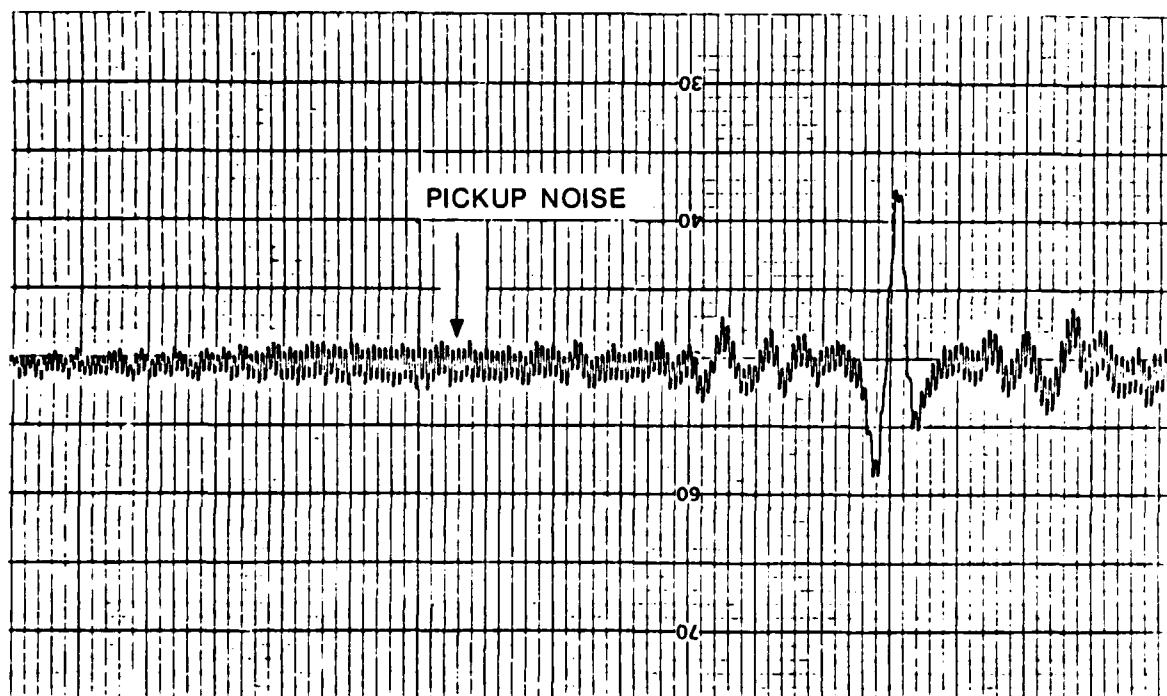


Fig. 11 Rapid scanning interferogram recorded with the initial servo-system, high frequency ripple is due to interference from the servo-system.

Manual rapid scanning showed (see Fig. 12) that this spurious signal did indeed arise from the servo-system, so it was necessary to remove the continuous digital feedback. A centering spring was added to the mirror drive and a function generator was used to scan the interferometer in an open loop. This mode is selected in Fig. 10 when the function generator is switched in.

In the revised system, the encoder pulses are not used for feedback to the servo-system, but they are used by the control processor to send to the data logging system to trigger analog-to-digital conversion. This is the primary purpose of the encoders in any case. With the Control Electronics, one can define the size of the sampling interval in terms of the number of encoder pulses between samples. In the course of this work, various data logging computers have been used and need not be commented on in detail. The same computers have been used to implement the Fourier transforms [25].

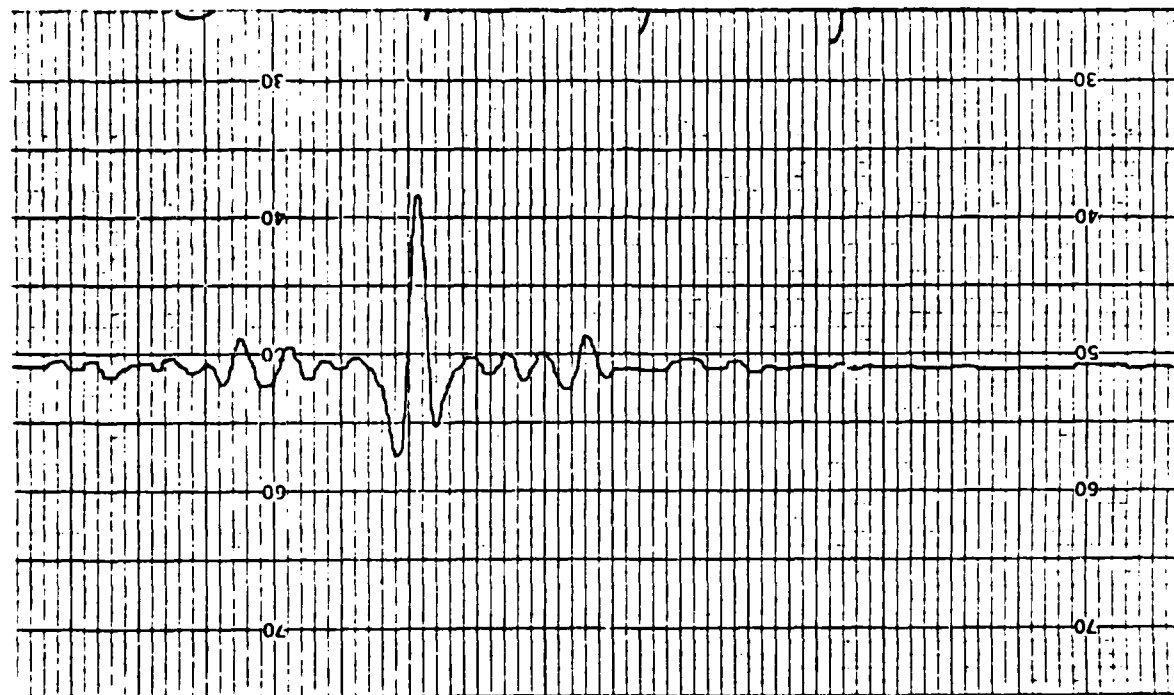


Fig. 12 Rapid scanning interferogram recorded with manual scanning

6 CALIBRATION

To determine atmospheric transmission from spectroscopic measurements of transmitted signals, it is necessary to know the signal that would have been obtained if the atmosphere were not present and absorbing. The source, the instrumentation, the geometry of the propagation path, and atmospheric attenuation all contribute to the shape and magnitude of the spectrum of radiation received over the propagation path. In a laboratory experiment involving an absorption chamber, it is often possible to pump out the atmosphere and record a spectrum characteristic of the instrumental-type effects. The atmospheric transmission is then the ratio of spectra with and without the atmosphere. Clearly, we cannot do this in the open atmosphere.

In monochromatic experiments, methods have been devised to remove most instrumental effects [26]. Multiple corner cube reflectors are set up at different ranges from the transceiver. Ratios of signal received from the various corner reflectors depend on the differential atmospheric attenuation between the ranges and on differential diffraction losses. Since the monochromatic sources can be approximated by point sources, the differential diffraction losses are calculable and the signal ratios can be corrected to find the contribution of atmospheric transmission.

In the use of extended, wide-band sources, diffraction effects are not practically calculable. The best that one can do is record the spectrum of signals received from the full path (400 m) and another over a short path, and then take the ratio. The resulting spectral ratio is an approximation to the transmission spectrum with two things which are unknown: the actual transmission scale at a given frequency, and any remaining instrumental trends in the spectrum. The root source of these uncertainties are questions about how the propagated beam diverges, as a function of frequency, resulting in incomplete capture of the signal by the retroreflector and the receiving antenna. On the other hand, such ratios of long and short path spectra should remove any narrow instrumental effects, such as features due to internal interference in the lamp envelope. All that should remain of frequency dependent instrumental effects are slow trends in propagation efficiency. Since an extended source is used that over-fills both retroreflector and the receiver, even these should be minor over much of the NMMW band. Thus, it should be possible to obtain spectra which will show whether or not isolated anomalous atmospheric absorption features (the third characteristic mentioned in the introduction) appear between the known water vapor lines.

By making measurements during different atmospheric conditions, ratios of atmospheric transmission can also be obtained with an absolute scale. Since warm, dry weather has been said to be less likely to produce anomalous absorption, such conditions can be used as a reference to test hypotheses about the existence of anomalous phenomena.

For the facility described here, a small retroreflector, like that at the remote site, has been constructed as shown in Fig. 13. It can be rolled into place and then keyed to the antenna for reproducible location. This has been useful also for testing the interferometer and detector.



Fig. 13 Photograph of calibration retroreflector

7 ENERGY BUDGET

In this section, we will calculate what is expected in signal levels through the instrumentation and over the propagation path. We can make two useful estimates: the total signal in the pass band of the system, and the signal in one resolution width (7.5 GHz). Most of the signal of interest is between 60 and 450 GHz, since the instrumentation will probably have poor response and throughput below this range, and the atmosphere will absorb most of the signal above this range. To facilitate calculation of the total signal, we divide the whole range into three intervals, between 60-180, 180-310, and 310-450 GHz. The boundaries of these intervals are natural ones determined by noticeable water lines. The signal received in each interval is then the product of

- integrated power from the source
- instrumental transmission
- fraction of signal received by the retroreflector
- fraction of signal received by the receiving antenna, and
- mean transmission of the atmosphere over 400 m.

We begin with the signal radiated by the source. The Rayleigh-Jeans approximation for black body radiation holds in this range. Thus, the power ΔP available in a resolution width $\Delta \nu$ can be approximated by

$$\Delta P_s = 2kTA\Omega\nu^2 \frac{\Delta \nu}{c^2}$$

and the integrated power P_s between two frequencies ν_1 and ν_2 , in Hz, is given by

$$P_s = 2kTA\Omega \frac{(\nu_2^3 - \nu_1^3)}{3c^2}$$

where k is Boltzmann's constant, T is the source temperature, A is the area of the source, Ω is the solid angle in which radiation is collected from the source, and c is the speed of light. We have used the following values:

$$T = 2000K$$

$$A = 1.075 \times 10^{-3} m^2$$

$$\Omega = 0.0641 \text{ str}$$

Values of ΔP_s and P_s calculated for the three intervals are given in Table 1.

Table 1. Factors in the Expected Signals over the 400 m Propagation Path			
	Frequency Interval, GHz		
Factor	60-180	180-310	310-450
Source power in a resolution interval, W	4.6×10^{-9}	1.9×10^{-8}	4.6×10^{-8}
Integrated source power in each interval, W	7.9×10^{-8}	3.4×10^{-7}	8.7×10^{-7}
Instrumental transmission	0.047	0.047	0.047
Chopper factor when total power is measured	0.5	0.5	0.5
Fraction received by retroreflector	0.08	0.08	0.08
Fraction received by receiver	0.045	0.045	0.045
Mean atmospheric transmission	0.90	0.77	0.25
SIGNAL NEAR THE CENTER OF EACH INTERVAL (IN A RESOLUTION WIDTH, 7.5 GHz), W	5.9×10^{-13} @ 110 GHz	2.5×10^{-12} @ 245 GHz	1.7×10^{-12} @ 340 GHz
TOTAL SIGNAL RECEIVED IN EACH INTERVAL, W	6.0×10^{-12}	2.2×10^{-11}	1.8×10^{-11}
TOTAL ALL INTERVALS, W	4.6×10^{-11}		

The instrumental transmission represents all transmission factors within the transmitter/receiver. There are a great many such factors, some of which are well known and some which are uncertain. Among those which are known are

- a factor of 1/2 for the selection of one plane of polarization
- a factor of 1/2 for interferometric modulation. This is applied even when total power is measured since this type of interferometer must be set at some large path difference: in this case only about half the frequencies transmit through the interferometer. When the interferometer is scanning, a given wavelength is transmitted about half the time.
- a factor of 1/2, if a chopper is turned on
- a factor of approximately 0.75 for reflective losses at the eight lens surfaces encountered by the radiation.

Among those which are not well-known are

- the cumulative effect of imperfections throughout the system including radiation lost at the edges of apertures
- the coupling efficiency to the detector element
- the interferometric efficiency, generally found to be in the range 0.8-0.9.

Thus we cannot estimate the total instrumental transmission with any degree of certainty. Since the unknown factors could be significant, we select a value of 0.25 to represent all unknown factors here, leaving a total instrumental transmission of 0.047 (except for a chopper factor).

The fraction of the power received by the retroreflector can be estimated as the ratio of the area of the retroreflector to that of the ideal projected image, or $1 \text{ m}^2 / (3.52 \text{ m})^2 \approx 0.08$. From ray traces, we estimate that the beam leaving the retroreflector will expand to twice the size of the retroreflector plus the size of the transmitting antenna by the time it returns to the receiver. Thus, the fraction received by the receiving antenna is $\pi(0.315/2.63)^2 \approx 0.045$. The atmospheric transmission values are rough approximations calculated from an empirical model [27] for a relative humidity of 50%, and temperature, 288K.

From the results in Table 1, we conclude that a detector sensitivity (NEP) of about $10^{-12} \text{ W/Hz}^{1/2}$ is necessary to have a signal to noise ratio in the spectrum of about 100 in an integration time of about 1/2 hr, or a signal to noise ratio of 50 in an integration time of a little over 1 sec. The best detector sensitivity achieved was 24 times worse than these figures. With such a sensitivity, the time to reach 100:1 SNR in a spectrum would have been unacceptably long, nearly 300 hrs.

8 RESULTS

The main results of this work to date have been tests of the equipment developed. A few tests have already been mentioned in foregoing sections; e.g., tests of the rapid scanning servo-system and of the preamplifier. In this section, tests of the antenna system, of the spectral response of the FTS, and of the sensitivity of the detector will be described.

After the antenna was assembled, but before the interferometer was fully mounted, we placed a projection lamp at the Cassegrain focus of the antenna. In nighttime experiments, we adjusted the antenna and focused it on the tarpaulin of the remote retroreflector to determine the quality of the focus. While all the optical elements are polished so that they look optically shiny, they are not figured to optical wavelength tolerances. The projection lamp had a filament that was about 3 mm across, so if the antenna were optically perfect, the spot on the retroreflector would have been about 0.32 m across. The observed spot was about 0.75 m across, suggesting that the size of the blur circle of the antenna is about 0.45 m. Such excellent performance should add little to the losses in the system.

Once the interferometer and other optics were mounted on the table attached behind the antenna, it was no longer possible to use this method to aim the antenna since the Cassegrain focus is near the beam splitter BD1. Instead, rough initial alignment can be obtained by several steps: First we look for the crude image of the retroreflector during daylight. If this proves difficult, we can place a bright lamp in the middle of the retroreflector at night and look for the image of this source. We then reverse the process and place a photo-flood in front of the Cassegrain aimed at the retroreflector with plate-glass mirrors covering the Hexcell™ plates. The retroreflector is then aimed so that the reflected light is centered on the hut on the roof housing the transmitter/receiver. Finally, the mercury lamp source is temporarily replaced with a 90 GHz Gunn source which sends a clear signal through the whole system and permits final adjustment to maximize this signal.

During the course of the work, interferograms were produced to verify that good spectra could be obtained. An interferogram, which was presented earlier in Fig. 12, was obtained from the short path to the calibration reflector. The corresponding spectrum is shown in Fig. 14. The locations of expected water vapor lines are shown and account for most of the features in the spectrum. One at about 660 GHz is probably an example of features due to interference in the detector window. Such features are commonly found and should disappear when ratios of long and short path spectra are taken.

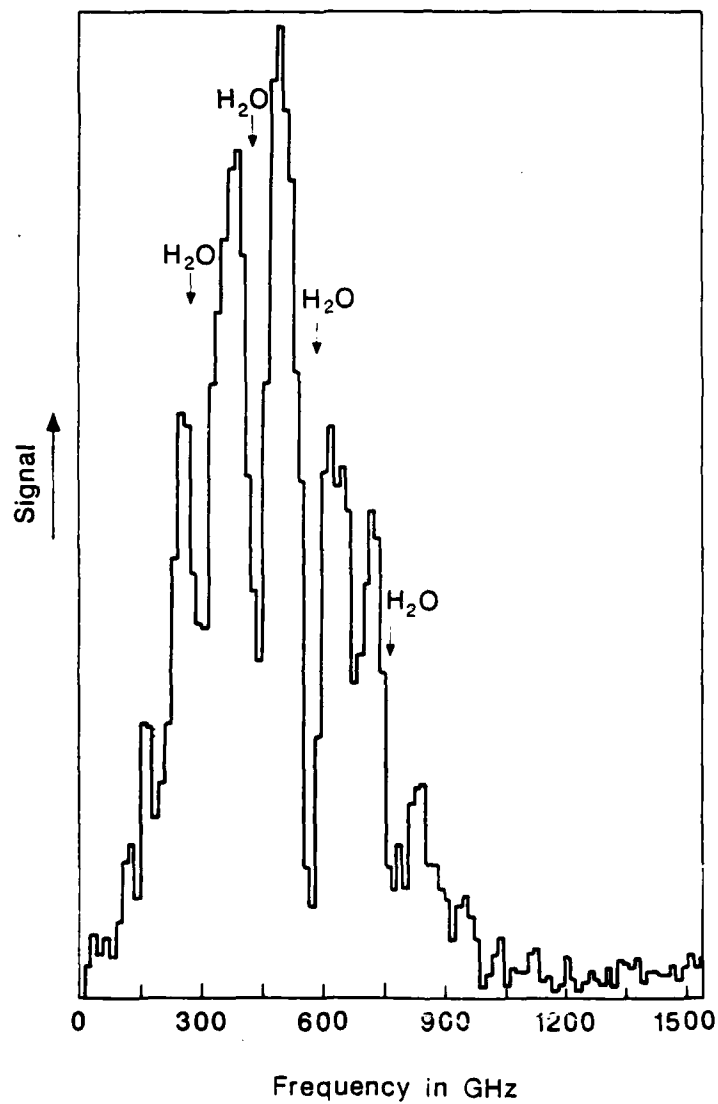


Fig. 14 Spectrum obtained by Fourier transformation of the interferogram in Fig. 12. The atmospheric path length was about 2.5 m. Resolution, about 50 GHz.

Throughout the work, we battled problems with detector sensitivity. Improvements gradually came through better contacting and making a better thermal contact between the detector post and the liquid-helium temperature detector cavity. During the latter stages, we devised a laboratory test for detector NEP. This involved a large aperture, temperature-controlled black body source about 80K higher in temperature than the room. We measured the signal from this source using a chopper and a lock-in amplifier. We estimated the limiting area-solid angle product in the system and calculated the optical NEP to be $2.4 \times 10^{-11} \text{ W/Hz}^{1/2}$. The voltage noise of the cold detector element was measured to be $2.1 \text{ nV/Hz}^{1/2}$. Thus the responsivity of the detector is 117 V/W .

The IV characteristics of the detector were also measured. The dynamic impedance of the detector at the operating current of 70 microamps was found to be 272 ohms. The electrical NEP derived from the shape of the IV curve was found to be $5 \times 10^{-13} \text{ W/Hz}^{1/2}$. This value is in line with typical InSb detector performance.

The size of the discrepancy between the optical and electrical NEP values is indicative of three possible problems:

- pathological low sensitivity to radiation due to poor absorption by the InSb element,
- a bad electrical contact
- the element being starved for radiation in its particular cavity environment

The last in this list was considered the least likely, and it is difficult to test for the first, so we attempted to improve the contacting. It is known that the best InSb contacts are made in an atmosphere free of oxygen and water vapor. Thus, we attempted to set up the entire contacting process in a glove box. However, repeated processing degraded the element to the point where it was no longer useable. Time and financial resources ran out in this contract effort before this problem could be resolved. At this point, the best course of action will be to purchase a new commercial element with a matching cavity and feed.

9 CONCLUSIONS

In the course of this work, a number of improvements have been made in instrumentation for NMMW research. In particular, an interferometer has been made with the following combination of features:

- High interferometric efficiency, due to the Martin-Puplett type design
- Ruggedness in photolithographically produced beam splitters
- Compactness and light-weight, of importance in attaching it to an antenna
- Capability for rapid scanning, enabling the recording of spectra in a fraction of a second.

Admittedly, severe problems have occurred in this work, of which the pivotal one in the end was detector sensitivity, as detailed above. Also, much more time had to be spent on developing the microprocessor-based controls for the system than had been anticipated. As a result, the intended atmospheric transmission research could not be carried out inside the resources of the contract. The research questions that were raised in the proposed research have been partially answered since the inception of this work. Subsequent, atmospheric transmission or emission

measurements have largely refuted the existence of anomalous absorption [e.g., 6,7,27,28]. It would still be desirable to see wide-band spectra for the perspective this would give, and it is our belief that the any remaining problems with the FTS equipment described here can be overcome.

10 REFERENCES

1. R. J. Emery, "Measurements of atmospheric absorption in the range 5-17 cm^{-1} and its temperature dependence, *J. Atmos. Terrest. Phys.*, vol. 42, pp. 801-807, 1980.
2. H. A. Gebbie, "Observations of anomalous absorption in the atmosphere," in *Atmospheric Water Vapor*, A. Deepak, T. D. Wilkerson, and L. H. Ruhnke, Eds. New York: Academic Press, pp. 133-141, 1980.
3. G. G. Gimmestad and H. A. Gebbie, "Measurements of near-millimeter wave atmospheric attenuation in the temperature range 259K to 282K," *Int. J. Infrared Millimeter Waves*, vol. 3, pp. 77-82, Jan. 1982.
4. R. A. Bohlander, *Spectroscopy of Water Vapor*, Ph.D. Dissertation, Imperial College of Science and Technology, 1979.
5. R. A. Bohlander, R. J. Emory, D. T. Llewellyn-Jones, G. G. Gimmestad, H. A. Gebbie, O. A. Simpson, J. J. Gallagher, and S. Perkowitz, "Excess absorption by water vapor and comparison with theoretical dimer absorption," in *Atmospheric Water Vapor*, A. Deepak, T. D. Wilkerson, and L. H. Ruhnke, Eds. New York: Academic Press, pp. 241-254, 1980.
6. L. I. Fedoseev and L. M. Koukin, "Comparison of the results of summer and winter measurements of atmospheric water vapor absorption of wavelengths 1.15 to 1.55 mm," *Int. J. Infrared Millimeter Waves*, vol. 5, pp. 953-963, July 1984.
7. N. I. Furashov, V. Yu Katlov, and V. Ya Ryadov, "On the anomalies in submillimeter absorption spectrum of atmospheric water vapor," *Int. J. Infrared Millimeter Waves*, vol. 5, pp. 971-984, July 1984.
8. R. A. Bohlander, R. W. McMillan, and J. J. Gallagher, "Atmospheric effects on near-millimeter-wave propagation," *Proc. IEEE*, vol. 73, pp. 49-60, Jan. 1985.
9. R. P. Walker and J. D. Rex, "Interferometer design and data handling in a high vibration environment. Part I: Interferometer design," *Trans. SPIE*, vol. 191, pp. 88-91, 1979.
10. J. H. Schummers, "Interferometer design and data handling in a high vibration environment. Part II: data handling," *Trans. SPIE*, vol. 191, pp. 92-95, 1979.
11. H. A. Gebbie, *Interferometry*, HM Stationery Office, 1960.
12. D. A. Naylor, R. T. Boreiko, T. A. Clark, "Mylar beam-splitter efficiency in far infrared interferometers: angle of incidence and absorption effects", *Appl. Opt.*, vol. 17, pp. 1055-1058, 1978.
13. D. H. Martin and E. Puplett, "Polarised interferometric spectroscopy for the millimetre and submillimetre spectrum", *Infrared Physics*, vol. 10, pp. 105-109, 1969.
14. O. A. Simpson, A. McSweeney, R. A. Bohlander, "Optical tests of quasi-optical components," *Proc. 6th Int. Conf. Infrared and Millimeter Waves*, IEEE Cat. 81 CH 1645-1, Miami Beach, FL, Dec. 7-12, 1981.

15. I. H. Hutchison, S. E. Kissel, "Calibration of a rapid-scan polarizing Michelson interferometer", *Proc. 4th Int. Conf. Infrared and Millimeter Waves*, IEEE Cat. No. 79 CH 1384-7 MTT, Miami Beach, FL, pp. 76-77, Dec. 10-15, 1979.
16. D. T. Llewellyn-Jones (unpublished work at Rutherford-Appleton Laboratory, England).
17. Donald E. Williamson, "Cone Channel Condenser Optics", *J. Opt. Soc. Am.*, vol. 42, pp. 712-715, 1952.
18. R. Kingslake, *Lens Design Fundamentals*, Orlando, FL: Academic press, pp. 36-37, 112-113, 1978.
19. E. B. Brown, *Modern Optics*, New York: Reinhold, p. 276, 1965.
20. G. R. Loefer, (unpublished work at Georgia Tech).
21. S. El-Atawy, P. A. R. Ade, J. V. Radostitz and I. G. Nolt, "Evaluation of composite bolometers at 0.4 Kelvin", *Int. J. Infrared Millimeter Waves*, vol. 1, pp. 459-468, 1980.
22. F. Nakajima, M. Kobayashi, and S. Narita, "New millimeter and submillimeter wave detecting system utilizing n-InSb electronic bolometer", *Jap. J. Appl. Phys.*, vol. 17, pp. 149-153, Jan. 1978.
23. R. A. Bohlander, J. W. Larsen, D. R. Lamm, M. J. Sinclair, G. D. Holah, A. McSweeney, O. A. Simpson, P. B. Reinhart and D. O. Gallentine, "Far infrared radiometric spectrometer (FIRRS)," R&D Design Evaluation Report, AFGL Contract F19628-80-C-0031, GT Project A-2519, May 30, 1983.
24. R. A. Bohlander, D. R. Lamm, J. W. Larsen, and M. J. Sinclair, "Far infrared radiometric spectrometer (FIRRS)", Final Report, AFGL-TR-83-0137, 29 July 1983.
25. N. Brenner, *IEEE Audio Transactions*, June, 1968.
26. A. B. Crawford and D. C. Hogg, "Measurement of atmospheric attenuation at millimeter wavelengths", *Bell Syst. Tech. J.*, vol. 35, pp. 907-916, July 1956.
27. H. J. Liebe, "Millimeter-wave properties of the atmosphere: laboratory studies and propagation modeling", NTIA Report 87-224, U. S. Department of Commerce, Oct. 1987.
28. D. P. Rice and P. A. R. Ade, "Absolute measurements of the atmospheric transparency at short millimeter wavelengths", *Infrared Physics*, vol. 19, pp. 575-584, 1979.

Appendix A

Fabrication of Polarizing Beam Splitters

by

A. McSweeney

The polarizing beam splitters consist of a pattern of parallel strips and spaces etched in an aluminum film on a Mylar* substrate. The widths of the opaque strips and of the spaces are about $5\text{ }\mu\text{m}$ each. Therefore there are 1000 line-pairs per cm. The thickness of the aluminum film is nominally $0.4\text{ }\mu\text{m}$. The thickness of the Type S Mylar* is $6\text{ }\mu\text{m}$.

The general procedure for fabricating the beam splitters is as follows:

1. A piece of Mylar is stretched over an aluminum beam splitter ring.
2. An aluminum film is deposited on the Mylar by evaporating aluminum wire in a vacuum chamber.
3. A thin layer of photoresist is applied over the aluminum layer.
4. The photoresist is exposed to UV radiation through a mask.
5. Developing the resist leaves the line pattern of the mask in the resist. The pattern consists of parallel strips of resist separated by uncoated strips of aluminum.
6. The strips of uncoated aluminum are etched away from the Mylar leaving the pattern of opaque aluminum strips separated by transparent spaces.

*Mylar is a registered trademark of DuPont.

The detailed procedure for fabricating the beam splitters is as follows:

1. A piece of Mylar is stretched over an aluminum beam splitter ring. Installation of a clamping ring further stretches the Mylar.

2. A measured quantity of high purity aluminum wire is placed on a tungsten filament in a vacuum chamber. The stretched Mylar film is cleaned with methanol and baked dry. It is then placed in the vacuum chamber about 15 cm above the filament loaded with aluminum wire.

After the chamber is evacuated, current is applied to the filament to first melt the aluminum wire and then to evaporate it. Some of the aluminum vapor coats the Mylar. The filament is kept at a high temperature until most of the aluminum has evaporated from the filament.

3. A resist promoter, hexamethyldisilazane (HMDS) is then applied and spun off in a temperature and humidity controlled chamber.

4. Thinned Shipley AZ1350J Positive Resist is then deposited on the aluminum film. The resist mixture consists of two parts resist to one part AZ Thinner. When the aluminum surface is covered with the resist solution the beam splitter ring is spun at about 3000 rpm for 25 seconds. This is done in a dust-free environment. The resist is then "soft-baked" at 85°C for 25 minutes.

5. The mask and resist surface are then pressed together in an evacuable container shown in Figure A1. The container has a large aperture in the metal bottom to allow exposure of the photoresist to UV radiation. A 12 mm inch thick transparent fused quartz plate is placed over an O-ring to serve as a window. The cleaned mask is then placed on top of the fused quartz plate with the chromium mask pattern facing up.

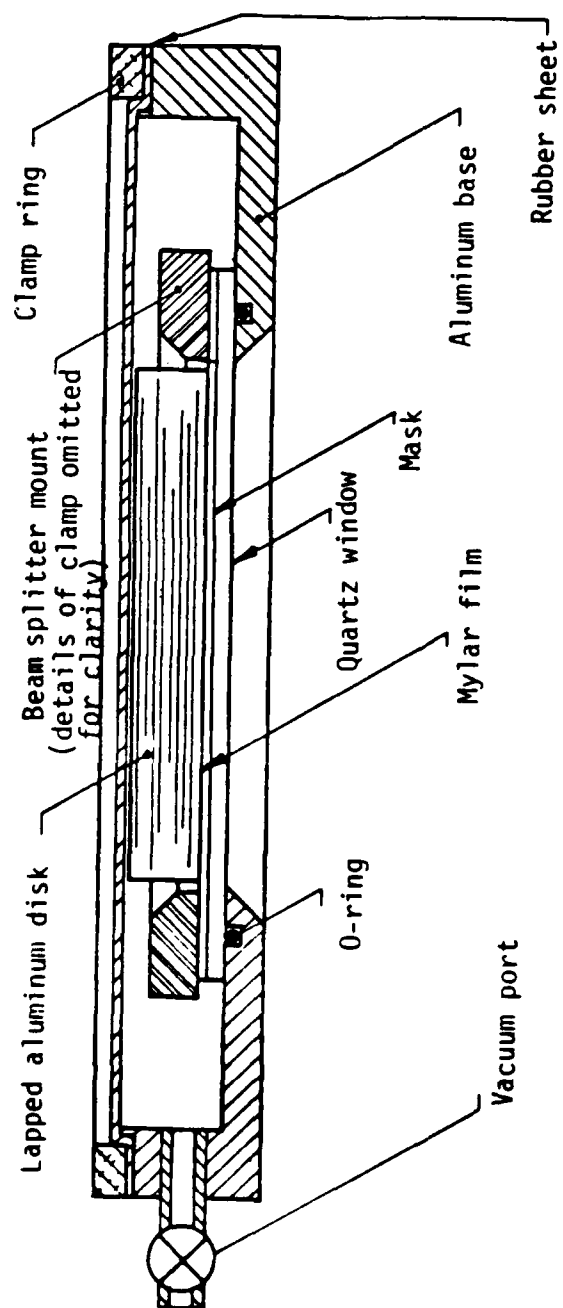


Figure A1. Assembly for exposing photoresist on aluminum coated Mylar film, not to scale.

Then the beam splitter ring, with the resist surface facing down, is placed on top of the mask. A lapped aluminum disk is then placed inside the beam splitter ring, with the lapped surface pressing down on the Mylar. The thickness of the aluminum disk is greater than the thickness of the beam splitter ring, so the top of the disk is the tallest part of the stack. The outer diameter of the disk is just slightly smaller than the inner diameter of the beam splitter ring. Therefore, the entire usable area of the photoresist surface is pressed into contact with the mask. Finally, a sheet of rubber is clamped by the edge to the top of the evacuable container. When the air is pumped out of the container, the rubber sheet is pressed in by atmospheric pressure. It presses against the aluminum disk which in turn presses the flexible Mylar with its aluminum and photoresist coatings into contact with the mask. A UV lamp is then used to expose the photoresist through the window in the bottom of the container and through the mask pattern. The exposure lasts about 1 minute.

6. The beam splitter ring is then removed from the evacuable container and the photoresist is developed in a mixture of 20 parts AZ-351 Developer and 70 parts water for 15-20 seconds. After a deionized water rinse, it is dried and examined under a microscope.

7. The photoresist surface is then "hard-baked" at 110°C for 20-30 minutes.

8. The aluminum etch solution is a mixture of one part Acetic Acid, 16 parts Phosphoric Acid, one part Nitric Acid, and two parts water. A drop of Kodak Foto Flo is added as a wetting agent and the temperature is raised to 42.5°C . It takes about 2 minutes for the aluminum to be etched away sufficiently to see light through the beam splitter.

9. The remaining photoresist is removed from the aluminum. This is accomplished by the use of acetone. The beamsplitter is then rinsed in deionized water and blown dry with nitrogen.

10. The final step is to remove the Mylar film from the aluminum ring, clean the aluminum and the O-ring, and then re-stretch the Mylar in the aluminum ring.

Appendix B.

THEORETICAL OPTICAL PROPERTIES OF A GRID ON A DIELECTRIC FILM

R. A. Bohlander

1.0 Introduction

A grid of metal strips, or wires, preferentially reflects the plane of polarization parallel to the strips and preferentially transmits the orthogonal polarization when the wavelength is long compared with the grid period. Polarizers and polarization sensitive beam splitters have been constructed on this principle mainly for use at infrared and longer wavelengths. When the application is in the microwave region, strips or wires can be stretched on a frame to make a "free standing" grid. This technique has been extended well into the submillimetre or far infrared region (Ade et al. 1979; Simonis 1979) by the fabrication of grids with periods as small as 5 μm and wire diameters as small as 12.5 μm . Transmissions and reflections of the respective polarizations in excess of 95 percent have been measured (Ade et al. 1979) for wavenumbers as high as 100 cm^{-1} . However, there are potential advantages in forming the grid on a dielectric substrate. This can be done, for example, by photoetching a grid pattern in a thin metal layer deposited on the dielectric. The substrate then helps to preserve the accuracy of the grid, particularly the fine ones used at high wavenumbers.

The performance of such grids has been studied by Auton (1967) in the wavelength range 20 to 100 μm and for grid periods of 4 to 10 μm . Each disc, made of polyethylene, was thick relative to the wavelength, and its surfaces were not sufficiently parallel to cause resonances between multiply reflected waves. In this case, the dielectric has a deleterious effect on transmission as summarized by Auton (1967): "supporting a grid on a substrate of refractive index n not only reduces the wanted polarization, as compared with the unsupported grid, but also

increases the transmission of the unwanted polarization". However, if the faces of the substrate are parallel, interference between multiply reflected beams can occur. If the thickness of the substrate is chosen so that constructive interference gives a maximum transmission, the effect of the substrate on the optical properties of the polarizer can be negligible. Auton (1967) commented on this but did not give a theoretical treatment.

The benefit of constructive interference can also be realized over a wide spectral region in which the wavelength is much longer than the thickness of the substrate. One region of interest is the near-millimetre to submillimetre wavelength range where new component development is being actively pursued. There is the need for polarizing beam splitters, for example in polarization diplexers (Chu et al. 1975) in Fabry-Perot etalons (Ulrich et al. 1963), and in the Martin-Puplett variation (Martin and Puplett 1969, Challener et al. 1980) of the Michelson interferometer. Films which are sufficiently thin, and have sufficient mechanical strength and transparency are available commercially; for example: Mylar (Smith and Lowenstein 1975), thickness $\geq 2 \mu\text{m}$; Kapton (Smith and Lowenstein 1975), $\geq 8 \mu\text{m}$; and polypropylene (Chantry and Chamberlain 1972), $\geq 12 \mu\text{m}$. It may be mentioned that these films have also been important as substrates for metal meshes used in the fabrication of multilayer interference filters for the far infrared (Holah et al. 1979).

There has been considerable interest in the theory of the optical properties of grids. Larsen (1962) reviews work up to about 1962 mainly on grids of wires. Some of the more recent work is referenced by Kalhor (1978). When one is undertaking the design or the evaluation of a polarizing beam splitter, a complete picture of both its transmission and reflection properties is needed, and in many cases arbitrary input polarization and incidence must be considered. We have found that a more complete theoretical model is needed for a grid of metal strips on a dielectric film than is readily available in the literature.

The preliminary account which is given here is an extension of a theoretical treatment given by Adonina and Shestopalov (1963), hereafter referred to as AS. The present results are part of a larger effort, including measurements, which will be reported elsewhere in due course.

2.0 Theory

2.1 No Dielectric Substrate

We will consider a grid which has a period g and metal strips of width a , as shown in Figure 1, and initially we assume that the metal strips are very thin, ideal conductors. Agronovitch et al. (1962) were able to express the diffraction from a free standing grid of metal strips as a boundary-value problem of the Riemann-Gilbert type for which solutions were known. Their approach can in principle give a full description of all diffracted orders. The validity of their method has been checked by Kalhor (1978) and compared with an exact solution for a special case by Baldwin and Heins (1954). The work of Agronovitch et al. was a seminal paper in the Soviet literature on diffraction by optical systems involving metal strips, and the paper by AS was an extension of their theory to the case of a dielectric substrate.

However, polarizing beamsplitters are used at wavelengths which are long enough that only zero order diffraction need be considered. We will assume that the wavelength λ of the radiation is much greater than g and will discuss later the theoretical limit to the validity of this assumption. It is helpful to subdivide the problem into cases where

- a) the plane of incidence is either perpendicular
or parallel to the strips

- b) the plane of polarization is either perpendicular
or parallel to the strips.

An arbitrary wave can be subdivided into waves of the two polarizations mentioned in (b), but a subdivision for an arbitrary direction of incidence

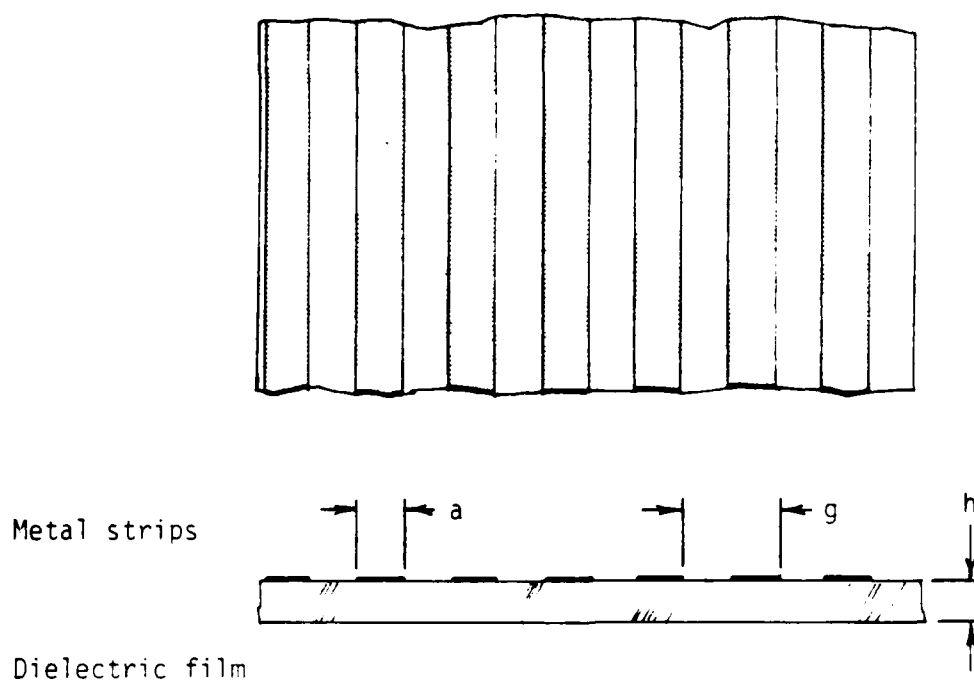


Figure B.1 Polarizer made from a grid of metal strips on a dielectric film.

along the lines in (a) is of course not possible. Nevertheless, it is helpful to focus on the two limiting cases mentioned in (a) for the present. For the amplitude reflection and transmission coefficients r and t to be discussed, we will use a first subscript to specify the orientation of the plane of incidence, and the second, the orientation of the polarization; a 1 is used for perpendicular and 2 for parallel.

When there is no dielectric substrate, the amplitude reflection and transmission coefficients in the long wavelength limit are well-known. Lamb (1898), Auton (1967) and others give expressions for normal incidence and Marcuvitz (1951), Smirnov (1958) and others give relevant expressions for oblique incidence. This can be summarized by the following

$$r_{12} = \frac{-1}{1 + i \frac{g}{\lambda} \ln \left(\frac{u+1}{2} \right) \cos \theta} \quad (1a)$$

$$t_{12} = \frac{-i \frac{g}{\lambda} \cos \theta}{1 + i \frac{g}{\lambda} \ln \left(\frac{u+1}{2} \right) \cos \theta} \quad (1b)$$

where $u \equiv \cos \left[\pi (g - a)/g \right]$ and θ is the angle of incidence. Since $g \ll \lambda$, reflection dominates for this polarization, as expected. The coefficients for the other plane of incidence r_{22} and t_{22} are obtained from r_{12} and t_{12} by setting the factors $\cos \theta$ to unity. The case of opposite polarization, ie. r_{11} , t_{11} , etc. may be obtained from the first by Babinet's principle (Born and Wolf 1970, pp. 559-60; AS). For example, r_{11} is obtained from t_{12} but with u replaced by $v \equiv \cos (\pi a/g)$. Intensity reflection and transmission coefficients are given by rr^* and tt^* , where $*$ denotes the complex conjugate, and these are the quantities usually tested by experiment. Excellent agreement between experiment and theory has been found (AS; Pursley 1956).

2.2 Dielectric Substrate. Only

Again, the theory is well-known (Born and Wolf 1970, pp. 60-62). The reflection and transmission coefficients for a dielectric slab which has parallel faces, and a thickness h are

$$r_s = \frac{r_\sigma + r_\sigma \exp(2i\gamma_2 h)}{1 + r_\sigma^2 \exp(2i\gamma_2 h)} \quad (2a)$$

$$t_s = \frac{t_\sigma t'_\sigma \exp(i\gamma_2 h)}{1 + r_\sigma^2 \exp(2i\gamma_2 h)} \quad (2b)$$

where r_σ is the amplitude reflection coefficient of each surface and t_σ and t'_σ are the amplitude transmission coefficients of the first and second surfaces. When the plane of polarization is perpendicular to the plane of incidence,

$$r_\sigma = \frac{\gamma_1 - \gamma_2}{\gamma_1 + \gamma_2}, \quad (3a)$$

$$t_\sigma = \frac{2\gamma_1}{\gamma_1 + \gamma_2}, \quad (3b)$$

and
$$t'_\sigma = \frac{2\gamma_2}{\gamma_1 + \gamma_2}, \quad (3c)$$

where $\gamma_1 = k \cos \theta$, $\gamma_2 = kn \cos \theta'$, $k = 2\pi/\lambda$, n is the index of refraction of the slab (assumed to be in air), and θ' is the angle of refraction. For the opposite polarization, $n \cos \theta'$ is replaced by $\frac{1}{n} \cos \theta'$ in equations (3). If the medium is absorbing, n is replaced by the complex refractive index $n + iK \lambda/(4\pi)$, where K is the absorption coefficient. $\cos \theta'$ is also complex and $n \cos \theta'$ may be expressed as (Born and Wolf 1970, pp. 627-30)

$$n \cos \theta' = v + wi \quad (4)$$

where

$$2v^2 = n^2 - \kappa^2 - \sin^2\theta + \sqrt{(n^2 - \kappa^2 - \sin^2\theta)^2 + 4\kappa^2 n^2}$$

$$2w^2 = -(n^2 - \kappa^2 - \sin^2\theta) + \sqrt{(n^2 - \kappa^2 - \sin^2\theta)^2 + 4\kappa^2 n^2}$$

and

$$\kappa = K\lambda/(4\pi).$$

The following familiar optical properties of a dielectric slab carry over to some extent when a grid is deposited on it:

- a) as the thickness increases, the reflection and transmission coefficients cycle between maxima and minima due to the interference of multiply reflected waves,
- b) reflection and transmission always depend on the angle of incidence (which was not always the case for a free standing grid)

and

- c) at Brewster's angle of incidence, $\theta = \tan^{-1}(n)$, the dielectric reflection coefficient is small when the plane of polarization is parallel to the plane of incidence.

The last property can be used to enhance the degree of polarization obtained from a grid formed on a substrate.

2.3 Metal-strip Grid on a Dielectric Slab

It is desirable to have expressions for the optical properties of such a grid for arbitrary planes of incidence. Wait (1957a, b, 1959; see also Wait 1954, and Larsen 1962b) has done this for grids made from wires. For metal strips on a dielectric slab, AS have considered only the plane of polarization perpendicular to the strips. This orientation gives the best polarization properties at oblique incidence for two

reasons: (1) as θ increases, the grid period appears to get smaller relative to λ [(notice the $\cos \theta$ factors in eq. (1)] and the leakage of the "wrong polarization" decreases; (2) the transmission of the "right polarization", namely that perpendicular to the strips, can be improved if θ is selected to be Brewster's angle for which the dielectric reflection is negligible. The latter was also pointed out recently by Challener et al. (1980). We will give a more complete formulation than did AS, but for the present we, too, will restrict our attention to the case where the plane of incidence is perpendicular to the strips. The formulation is also restricted in another way; namely, the incident beam is assumed to strike first the side with the metal strips. Of course, the intensity transmission coefficients in both directions must be the same, on thermodynamic grounds, but the reflection and absorption properties need not be. Other directions of incidence will be covered in a subsequent paper.

2.3.1 Polarization Parallel to the Strips

Formulas derived by AS for the polarization parallel to the strips are the following:

$$r_{12} = \frac{\frac{i}{2} \frac{g}{\lambda} \frac{\ln(u+1)}{2} (\gamma_1 - \chi_0 \gamma_2) - k}{\frac{i}{2} \frac{g}{\lambda} \frac{\ln(u+1)}{2} (\gamma_1 + \chi_0 \gamma_2) + k}, \quad (5a)^*$$

$$\text{where } \chi_0 = \frac{\gamma_2 + \gamma_1 - (\gamma_2 - \gamma_1) \exp(2i\gamma_2 h)}{\gamma_2 + \gamma_1 + (\gamma_2 - \gamma_1) \exp(2i\gamma_2 h)}; \quad (5b)$$

$$t_{12} = \frac{r_{12} + 1}{G} \quad (5c)$$

where G depends only on the dielectric properties and is given by

$$G = \frac{1}{2} \frac{\gamma_2 + \gamma_1}{\gamma_2} e^{i(\gamma_2 - \gamma_1)h} + \frac{\gamma_2 - \gamma_1}{\gamma_2} e^{i(\gamma_2 + \gamma_1)h} \quad (5d)$$

*Note: the reader should be warned that there are many errors in the formulas of AS which appear to have occurred in type-setting. Corrected formulas are indicated with an asterisk.

When there is no dielectric (ie., in the limit when $n \rightarrow 1$), equation (5) can be reduced to equation (1). Alternatively when there is no grid (ie., in the limit $a \rightarrow 0$), equation (5) can be reduced to equation (2). Also, the intensity coefficients $r_{12}r_{12}^*$ and $t_{12}t_{12}^*$ can be shown to be complementary; ie.,

$$r_{12}r_{12}^* = 1 - t_{12}t_{12}^*.$$

An assessment of the limit to the validity of the long wavelength approximation can be made by comparison of equation (5) with a more complete calculation involving higher orders of diffraction made by AS for the case where there is no dielectric slab. The comparison is shown in Figure 2 for two angles of incidence. When the incidence is near normal, the minimum wavelength λ_{\min} where there is good agreement is $\lambda_{\min} \approx 2.5g$. As θ increases, λ_{\min} increases so that, for $\theta=65^\circ$, $\lambda_{\min} \approx 5g$. Unfortunately, AS have not provided calculated transmission values in the case where the grid is on a dielectric slab. However, it is reasonable to suppose that λ_{\min} specified in air should increase with increasing n since the wavelength in the dielectric medium is reduced.

2.3.2 Polarization Perpendicular to the Strips

The formula given by AS for reflection is as follows

$$r_{11} = \frac{i \frac{g}{\lambda} \frac{n^2+1}{2} \ln \frac{(1+v)\gamma_1 - kn}{2}}{i \frac{g}{\lambda} \frac{n^2+1}{2} \ln \frac{(1+v)\gamma_1 - kn + k}{2}} \quad (6a)^*$$

$$\eta \equiv \frac{\frac{1}{2} + \frac{1}{2} n^2 \frac{\gamma_1}{\gamma_2} \frac{R_o + 1}{R_o - 1}}{\gamma_2} \quad (6b)$$

$$R_o \equiv \frac{\gamma_2 - n^2 \gamma_1}{\gamma_2 + n^2 \gamma_1} \exp(2i\gamma_2 h) \quad (6c)^*$$

AS do not give a formula for t_{11} , but by analogy with equation (5c) it should be of the form

$$t_{11} = \frac{r_{11} - 1}{G'} \quad (6d)$$

In the limit $n \rightarrow 1$, $G' \rightarrow 1$ and equation (6d) conforms to Babinet's principle; in the limit that the grid is absent ($a \rightarrow 0$), equation (6d) must go over to equation (2b). This fact provides a means of deriving a formula for G' which is

$$G' = \frac{1}{n-1} \frac{(n^2 \gamma_1 + \gamma_2)^2 - (n^2 \gamma_1 - \gamma_2)^2 \exp(2i\gamma_2 h)}{4 \gamma_1 \gamma_2 n^2 \exp(i\gamma_2 h)} \quad (6e)$$

As an example, we show in Figure 3 calculations of the reflection, transmission and absorption of a grid with the following parameters

$$\begin{aligned} g &= 20 \text{ } \mu\text{m} \\ a &= 10 \text{ } \mu\text{m} \\ h &= 13 \text{ } \mu\text{m} \\ n &= 1.5 \text{ (polypropylene)} \\ K &= \text{given by Chantry and Chamberlain (1972)} \\ \theta &= 30^\circ. \end{aligned}$$

2.4 Absorption

Absorption in the dielectric substrate may be included in equations (5) and (6) by following the procedure for replacing n and $n \cos \theta'$ by their complex values as described in section 2.2. However, absorption by the metal strips has not as yet been included in the theory.

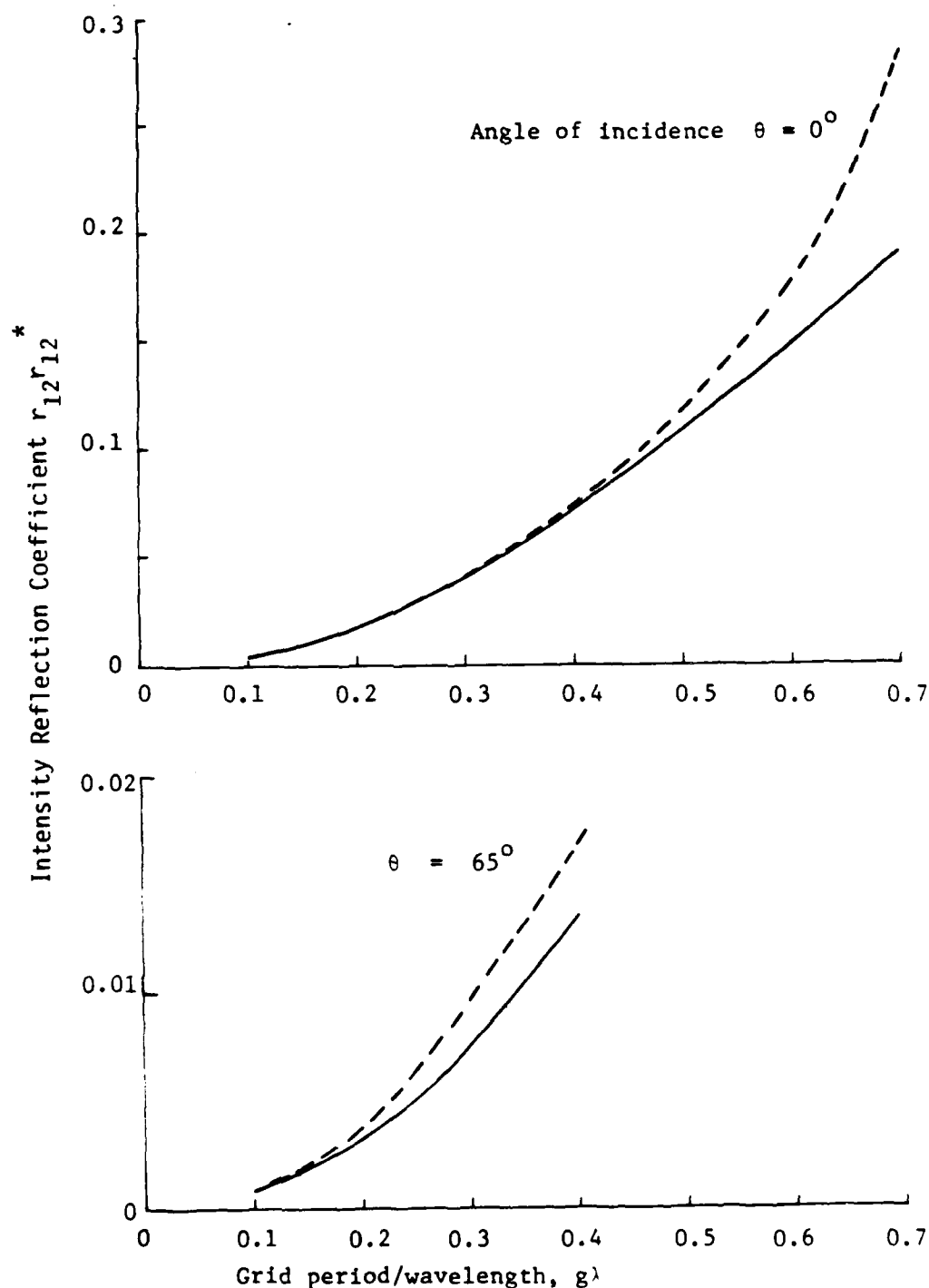


Figure B.2 Theoretical reflectivity of a grid for the plane of polarization parallel to the metal strips. — present calculations in the long wavelength approximation, ---- full calculation (Adonina and Shestopalov 1963). $a = g/2$. $n = 1$.

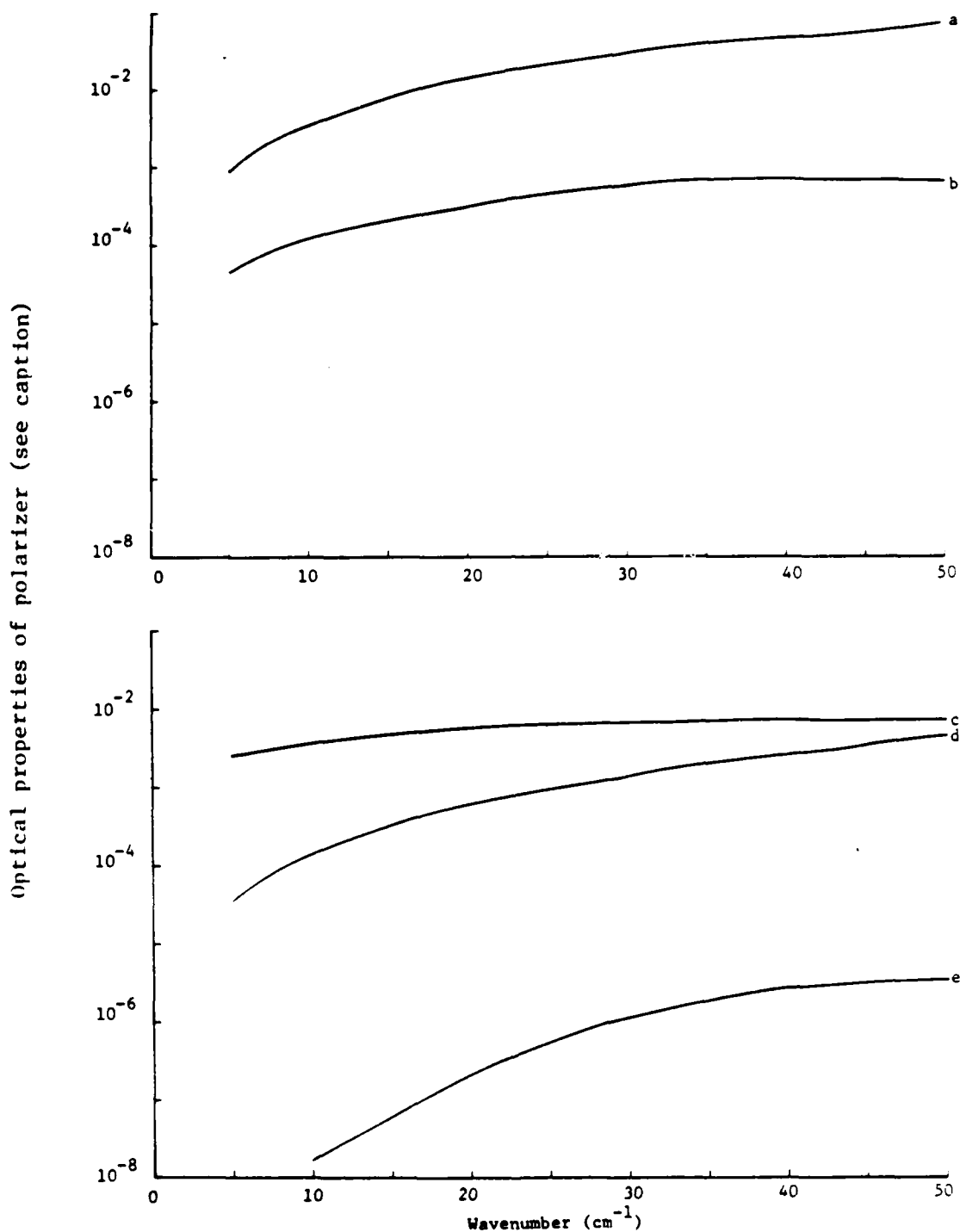


Figure B.3 Theoretical optical properties of a metal grid polarizer on a polypropylene film. [Parameters assumed: $g = 20 \mu\text{m}$, $a = 10 \mu\text{m}$, $h = 13 \mu\text{m}$, $\theta = 30^\circ$, $n = 1.5$, K in the range 0 to 0.36cm^{-1} (Chantry and Chamberlain 1972), and $\sigma = 1 \times 10^{17} \text{ statmho/cm}$. Curve a.) $r_{11}r_{11}^*$ and $1-t_{11}t_{11}^*$; curve b.) $1-r_{11}r_{11}^* - t_{11}t_{11}^*$; curve c.) ohmic losses A_{12} ; curve d.) $t_{12}t_{12}^*$ and $1-r_{12}r_{12}^*$; curve e.) $1-r_{12}r_{12}^* - t_{12}t_{12}^*$]

Generally, this is a small effect unless the beam splitter is part of a strongly resonant cavity such as a Fabry-Perot etalon. According to Ulrich et al. (1963), the fraction of the intensity absorbed by the strips is of the order of

$$A_{12} = \frac{g}{a} r_{12} r_{12}^* \left(\frac{c}{\sigma \lambda} \right)^{\frac{1}{2}} \quad (7)$$

for the polarization indicated, where σ is the conductivity of the strips and c the speed of light. For the opposite polarization, ohmic losses are considered negligible (Ulrich et al. 1963). Calculations of A_{12} are shown in Figure 3 for the grid described above.

3.0 Conclusions

Following Adonina and Shestopalov (1963), we have extended the set of equations for the reflection and transmission coefficients of a grid made of metal strips on a dielectric slab. Orthogonal planes of polarization have been considered. However, the equations are restricted to the case where the plane of incidence is normal to the strips, and the radiation is incident on the side with the metal strips. Whereas absorption in the dielectric substrate has been treated rigorously here, absorption by the metal strips has only been estimated to order of magnitude following Ulrich et al. (1963). Throughout this work, the approximation has been made that the wavelength λ is much longer than the grid period g . The limit to the validity of this assumption appears to be $\lambda > 5g$ for free standing strips, but it is not as well-known when the grid is on a dielectric substrate. The remaining problems will be addressed in further work, and an experimental evaluation of grid performance will be made.

4.0 References

P.A.R. Ade, A.E. Costley, C.T. Cunningham, C.L. Mok, G.F. Neill and T.J. Parker 1978, "Free-Standing Grids Wound from 5 μ m Diameter Wire for Spectroscopy at Far-Infrared Wavelengths," *Infrared Physics* 19, 599-601.

A.D. Adonina and V.P. Shestopalov 1963, "Diffraction of Electromagnetic Waves Obliquely Incident on a Plane Metallic Grating with a Dielectric Layer," *Sov. Phys. - Tech. Phys.* 8, 479-486.

Z.S. Agronovich, V.A. Marchenko, and V.P. Shestopalov 1962, "The Diffraction of Electromagnetic Waves from Plane Metallic Lattices," *Sov. Phys. - Tech. Phys.* 7, 277-286.

J.P. Auton 1967, "Infrared Transmission Polarizers by Photolithography," *Appl. Opt.* 6, 1023-1027.

G.L. Baldwin and A.E. Heins 1954, "On the Diffraction of a Plane Wave by an Infinite Plane Grating," *Math. Scand.* 2, 103-118.

M. Born and E. Wolf 1970, *Principles of Optics*, Pergamon Press, Oxford.

W.A. Challener, P.L. Richards, S.C. Zilio and H.L. Garvin, "Grid Polarizers for Infrared Fourier Spectrometers," submitted to *Infrared Physics*.

G.W. Chantry and J. Chamberlain 1972, "Far Infrared Spectra of Polymers," *Polymer Science*, 1330-1381.

T.S. Chu, M.J. Gans and W.E. Legg 1975, "Quasi-Optical Polarization Diplexing of Microwaves," *Bell Syst. Tech. J.* 54, 1665-1680.

G.D. Holah, B. Davis and N.D. Morrison 1979, "Narrow-Bandpass Filters for the Far-Infrared Using Double-Half-Wave Designs," *Infrared Physics* 19, 639-47.

H.A. Kalhor 1978, "Diffraction of Electromagnetic Waves by Plane Metallic Gratings," *J. Opt. Soc. Am.* 68, 1202-1205.

H. Lamb 1898, "On the Reflection and Transmission of Electric Waves by a Metallic Grating," *Proc. London Math. Soc.* 29, 523-544.

T. Larsen 1962, "A Survey of the Theory of Wire Grids," *IRE Trans. on Microwave Theory and Techniques*, 191-201.

T. Larsen 1962b, "Numerical Investigation of the Equivalent Impedance of a Wire Grid Parallel to the Interface Between Two Media," *J. Res. Nat. Bur. Std.* 66D, 7-14.

N. Marcuvitz 1951, Waveguide Handbook, M.I.T. Rad. Lab. Ser., McGraw-Hill Book Co., New York, N.Y.

D.H. Martin and E. Puplett 1969, "Polarized Interferometer Spectrometry for the Millimetre and Submillimetre Spectrum," Infrared Physics 10, 105-109.

W.K. Pursley 1956, "The Transmission of Electromagnetic Waves through Wire Diffraction Gratings," PhD. Thesis, University of Michigan.

G.J. Simonis, F. Weiser and G.L. Wood 1979, "Near-Millimeter-Wave Polarizing Wire Grid Fabrication and Evaluation," Fourth International Conference on Infrared and Millimeter Waves and Their Applications, Miami Beach, Fla., 10-15 December, 267-268.

N.N. Smirnov 1958, "Propagation of Electromagnetic Waves in Circular Waveguides with Periodic Slits," Sov. Phys. - Tech. Phys. 3, 1383-1391.

D.R. Smith and E.V. Loewenstein 1975, "Optical Constants of Far Infrared Materials. 3: Plastics," Appl. Opt. 14, 1335-41.

R. Ulrich, K.F. Renk and L. Genzel 1963, "Tunable Submillimeter Interferometers of the Fabry-Perot Type," IEEE Trans. on Microwave Theory and Techniques MTT-11, 363-371.

J.R. Wait 1954, "Reflection at Arbitrary Incidence from a Parallel Wire Grid," Appl. sci. Res. B4, 393-400.

J.R. Wait 1957, "The Impedance of a Wire Grid Parallel to a Dielectric Interface," IRE Trans. on Microwave Theory and Techniques MTT 5, 99-102.

J.R. Wait 1957b, "On the Theory of Reflection from a Wire Grid Parallel to an Interface between Homogeneous Media," Appl. sci. Res. B6, 259-275.

J.R. Wait 1959, "On the Theory of Reflection from a Wire Grid Parallel to an Interface between Homogeneous Media (II)," Appl. sci. Res. B-7, 355-360.

APPENDIX C

Measured Transmission and Reflection of Grid Polarizers on a Dielectric Film

by

O.A. Simpson
R.A. Bohlander
R.E. Forsythe

In this section of the report we present preliminary results of transmission measurements on 2 grid polarizers and a clear Kapton substrate with both a Fourier Spectrometer in the spectral region 10 to 100 cm^{-1} and a far-infrared (FIR) optically pumped laser at four frequencies between 8.2 and 61.3 cm^{-1} . The two separate sets of data are in excellent agreement.

The basic experimental apparatus for the Fourier measurements, a Grubb Parsons cube interferometer is shown in Figure C.1. An evacuated chamber with a grid polarizer and mirror arrangement (not shown) directed the linearly polarized broad band FIR radiation to normal incidence with the second polarizer (or clear substrate). The grid orientation was normal to the plane of polarization of the radiation for maximum signal transmission. The transmitted radiation then entered a Golay cell detector. Transmission spectra were determined from the ratio of spectra obtained for the second polarizer (or Kapton substrate) and spectra with no sample. The measured values are shown graphically in Figures C.2-C.4.

The grids tested were fabricated by Dr. G. Lamb at NASA Goddard Space Flight Center. He vacuum deposited 5000 Å of aluminum on Kapton $13\text{ }\mu\text{m}$ thick and then photo-etched the grid pattern of metal strips. The sample of Kapton film was processed in the same way, but all of the aluminum was etched off.

A block diagram of the optically pumped laser is shown in Figure C.5. A 20 watt CO_2 laser pumps a FIR laser of the metal waveguide type. The FIR beam was divided by the beam splitter BS2. The reference signal I_b , after detection and amplification by a Golay cell and lock-in amplifier, entered the denominator channel of the ratiometer RA. The beam

then entered a Fabry-Perot interferometer (FP) which was used both to measure the wavelength and as a filter to eliminate unwanted wavelengths that may have lased simultaneously with the desired signal. Since the radiation from this type laser is generally unpolarized, the signal I_a was passed through a polarizer to produce the desired plane of polarization. The signal was then transmitted through (or reflected from) the sample polarizer and detected by another Golay cell. This signal, after lock-in amplification, became the numerator signal in the ratiometer. The ratioing process was important in eliminating source fluctuations in the FIR power level. We will call values of I_a/I_b normalized signals.

The transmission of a sample polarizer was determined from the ratio of the normalized signal with and without the sample in the laser beam. The reflection coefficient was determined by the ratio of the normalized signal when the radiation was reflected from the polarizer and that for reflection from a mirror.

Results of the laser measurements, together with block diagrams of each experimental arrangement are shown in sections I,II,III.

CONCLUSION

In evaluating the performance of the grids we have used the theoretical framework in Appendix B. The polarizers we have tested were originally intended for millimeter wavelengths. However; theory suggested that they should be of use to much shorter wavelengths and so we have tested them to wavelengths as small as $100\ \mu\text{m}$. It is apparent from Figures C.3 and C.4. Table 2 that the polarizers perform well at millimeter wavelengths, but a close comparison with theory cannot be made in the absence of good absorption coefficient and refractive index data for the Kapton substrate. At short wavelengths the polarizer transmission and reflection are very different from expectation. When the plane of polarization incident on polarizer #2 is perpendicular to the grids, it is expected that the transmission would be close to that for the Kapton film alone. Instead the transmission is about a factor of 0.5 lower. From a comparison of tables I and II one can see that the transmission and reflection are almost

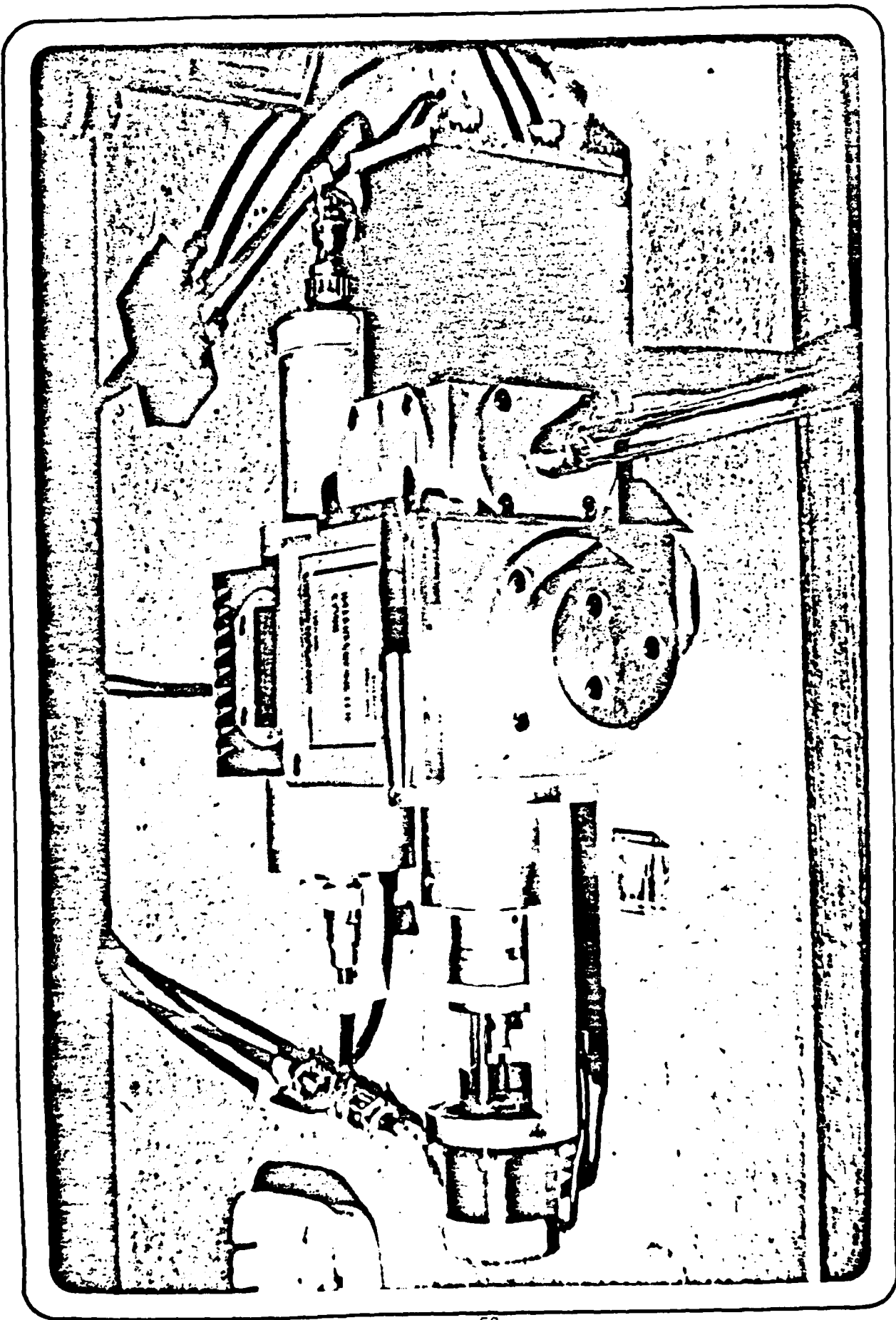


Fig. C.1 Grubb Parson Cube Interferometer

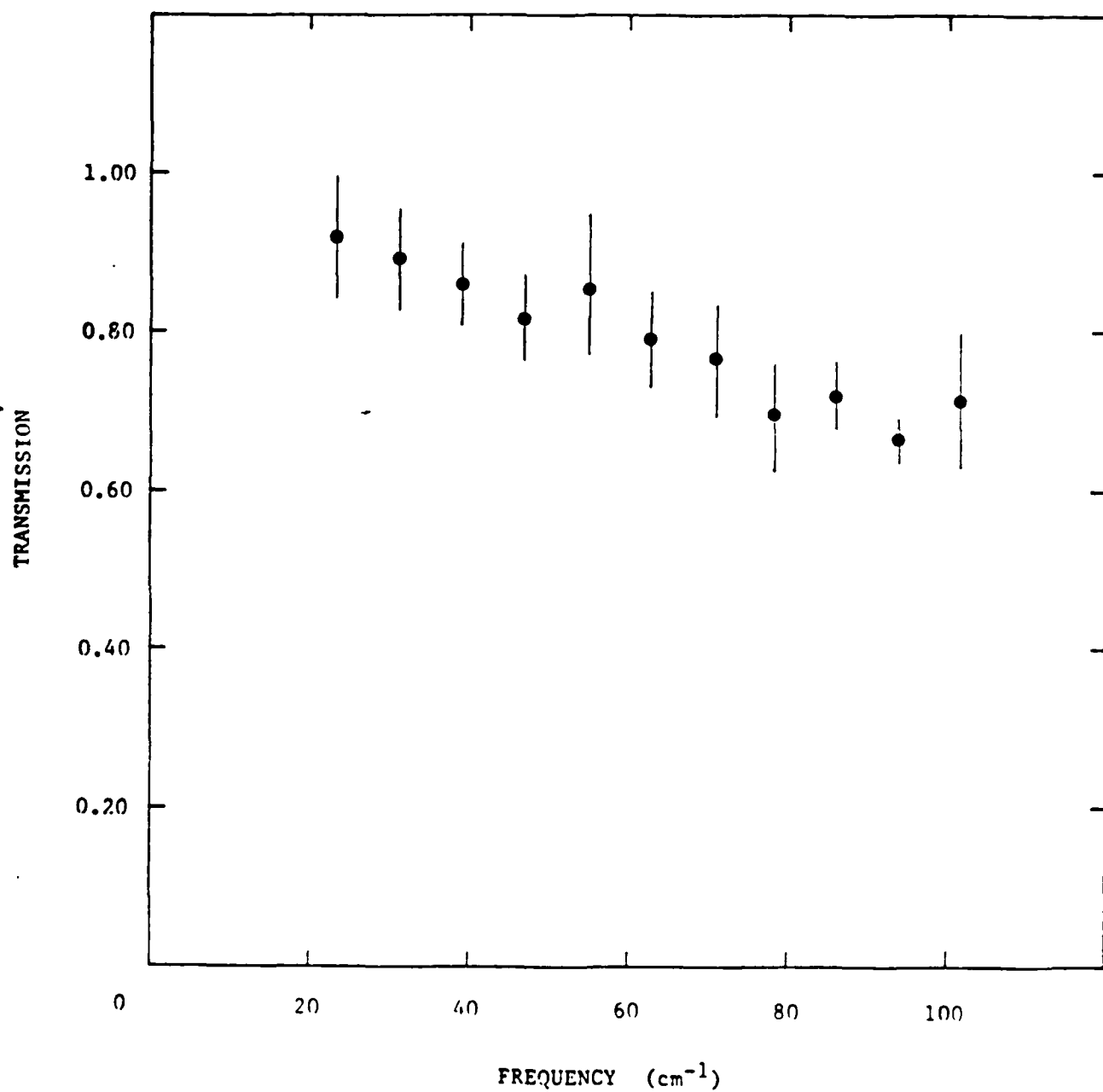


Fig. C.2 Fourier transmission spectra of the Kapton substrate. Substrate thickness is 12.7 μm .

complementary, so that the discrepancy does not arise in the main from absorption. Further experimental and theoretical work is needed to uncover the reason for the discrepancies. The one case where the discrepancies are not serious is when the grid period is very small, as is the case for the data shown in Figure C.4. The predicted spectrum for this case is very close to that of the substrate and agrees well with the data. The conclusion drawn from this is that polarizers for use with interferometers should have very small grid periods, and the period of 10 μm chosen for subsequent fabrication was about as small as could be fabricated accurately with the equipment available.

The primary parameters of the gridded beamsplitter were aperture, 95mm; Mylar substrate thickness, 6 μm ; strip width, approximately 4 μm ; and strip period, 10 μm . Four types of techniques were used to measure the transmission properties of these grids, and one to measure the reflection properties. Figure C.6 shows the layout of instrumentation used to make transmission measurements with the optically pumped laser at frequencies of .525, 1.84 and 2.54 THz. As shown in Figure C.7, the transmission of the polarizer is high as expected when the plane of the polarization is perpendicular to the strips. Comparison is made with theoretical calculations done according to the theory of Adonina and Shestopalov and good agreement is found. On the basis of the work described above, this is to be expected only when the wavelength is much greater than the grid spacing, as is true here. In this case, the polarizer's transmission is mainly limited by that of the substrate as also shown in Figure C.7. The transmission of the opposite polarization is small as expected (see Figure C-7), although not quite as small as predicted by the theory used. Table C.4 gives values of the polarization ratio; i.e., the ratio of the signal for polarization perpendicular to the strip and that parallel.

Table 2 (continued)

λ (μm)	Line Orientation			Measured Transmission
	Pol. 1	Pol. 2	θ	
1217	H	H	0	0.941
1217	H	H	10	0.948
1217	H	H	20	0.944
1217	H	H	30	0.949
1217	H	H	40	0.932

Table 3. Kapton substrate transmission data for normal incidence.

λ (μm)	Kapton Substrate Thick. (mills)	Transmission
185.4	0.3	0.91
185.4	0.5	0.83
570.5	0.3	0.98
570.5	0.5	0.95
1217	0.5	0.96

II. Transmission coefficient measurements.

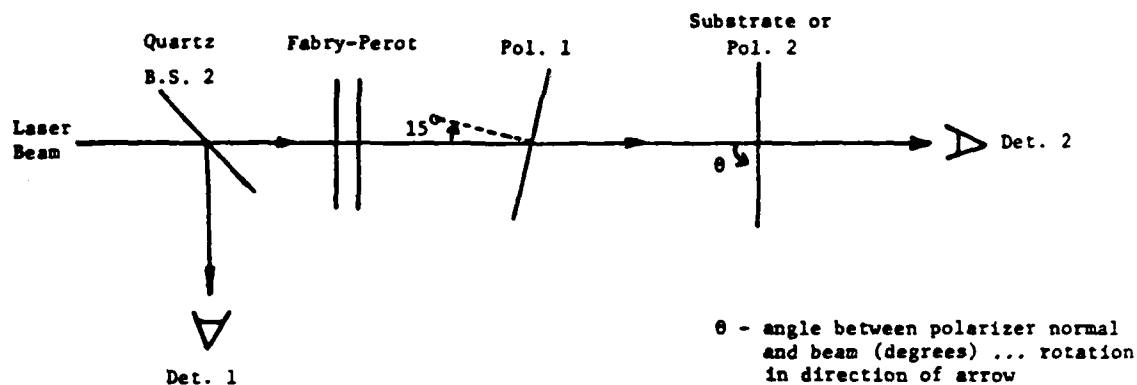


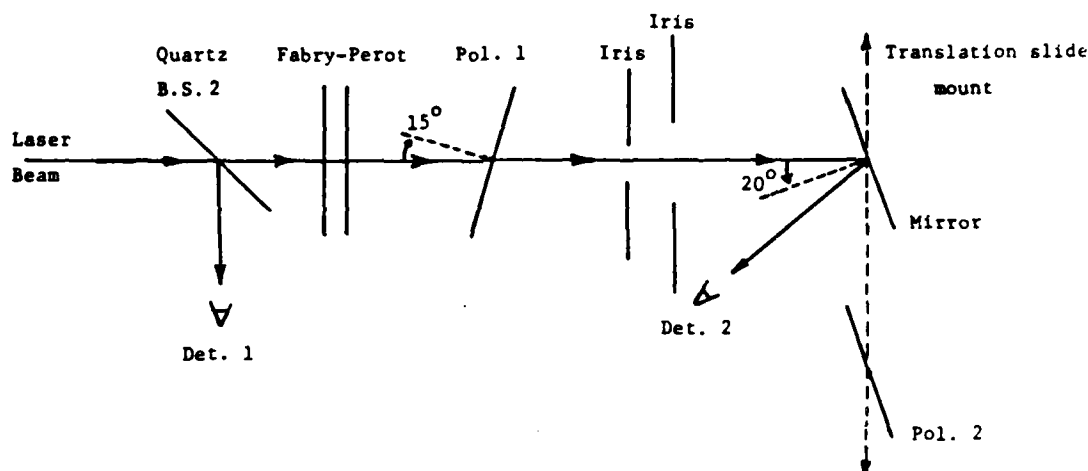
Table 2. Polarizer transmission data.

λ (μm)	Line Orientation			Measured Transmission
	Pol. 1	Pol. 2	θ	
163	H	H	0	0.405
163	H	H	10	0.406
163	H	H	20	0.401
163	H	H	30	0.363
163	H	H	40	0.356
185.4	V	V	0	0.434
185.4	V	V	10	0.421
185.4	V	V	20	0.443
185.4	V	V	30	0.482
185.4	V	H	0	0.034
185.4	V	H	10	0.047
185.4	V	H	20	0.048
185.4	V	H	30	0.049
570.5	H	H	0	0.805
570.5	H	H	10	0.782
570.5	H	H	20	0.787
570.5	H	H	30	0.783
570.5	V	V	0	0.761
570.5	V	V	10	0.785
570.5	V	V	20	0.809
570.5	V	V	30	0.832
570.5	V	H	0	0.016
570.5	V	H	10	0.013
570.5	V	H	20	0.012
570.5	V	H	30	0.013

V - vertical (\perp to page)
H - horizontal (\parallel to page)

(table continued - next page)

I. Reflection coefficient measurements.



Note: the translation slide mount allowed the mirror and polarizer to be interchanged ... coincidence of the two surfaces was constantly checked by the reflection of a HeNe laser. The second iris has a larger aperture than the first and absorbing sheets (Eccosorb) on both sides to stop stray radiation.

Polarizer #1 has a strip spacing of $50.8 \mu\text{m}$ and a strip width of $12.7 \mu\text{m}$ on a Kapton substrate $12.7 \mu\text{m}$ thick.

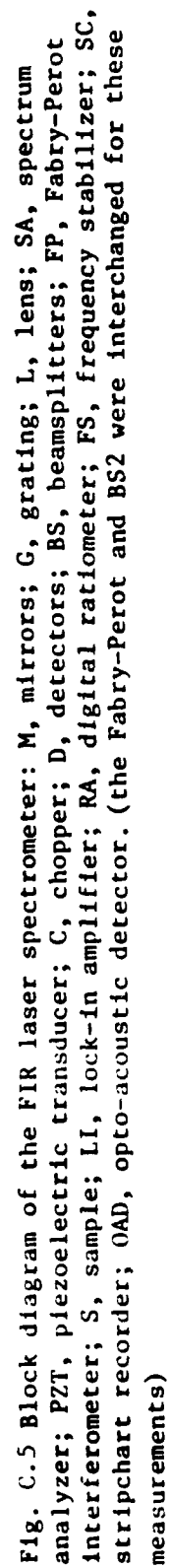
Polarizer #2 has a strip spacing of $50.8 \mu\text{m}$ and a strip width of $19.1 \mu\text{m}$ on a Kapton substrate $12.7 \mu\text{m}$ thick.

Table 1. Polarizer reflectivity data.

λ (μm)	Line Orientation		Measured Reflection
	Pol. 1	Pol. 2	
570.5	V	V	0.137
570.5	V	H	0.930
185.4	V	V	0.458
185.4	V	H	0.970
1217	V	V	0.045
1217	V	H	0.979

V - vertical (\perp to page)

H - horizontal (\parallel to page)



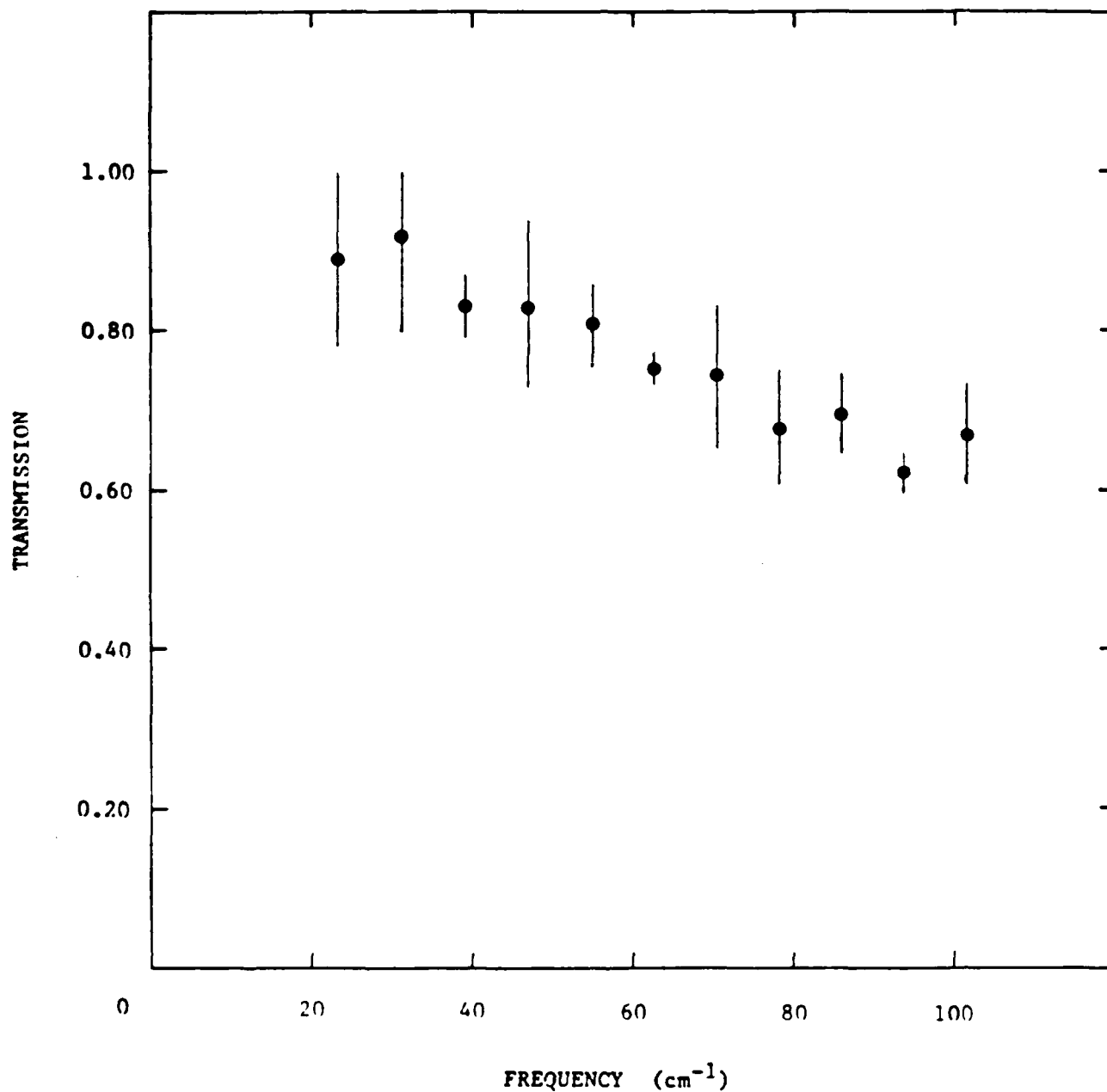


Fig. C.4 Fourier transmission spectra of a fine Kapton - aluminum grid polarizer. Polarizer has a strip spacing of 3 μm and a strip width of 1.5 μm on a Kapton substrate 12.7 μm thick.

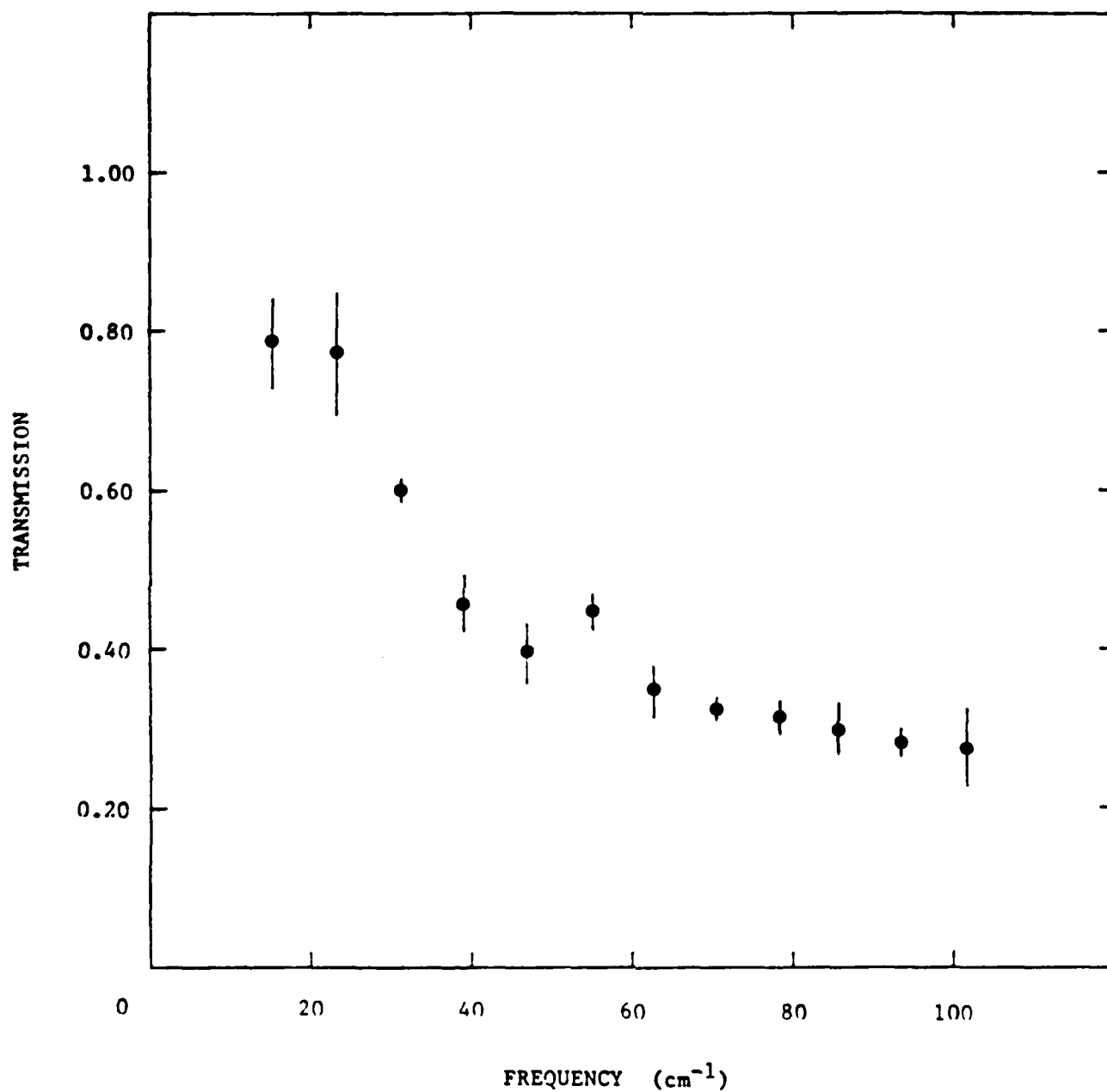


Fig. C.3 Fourier transmission spectra of the Kapton - aluminum grid polarizer. Polarizer has a strip spacing of 50.8 μm and a strip width of 19.1 μm on a Kapton substrate 12.7 μm thick.

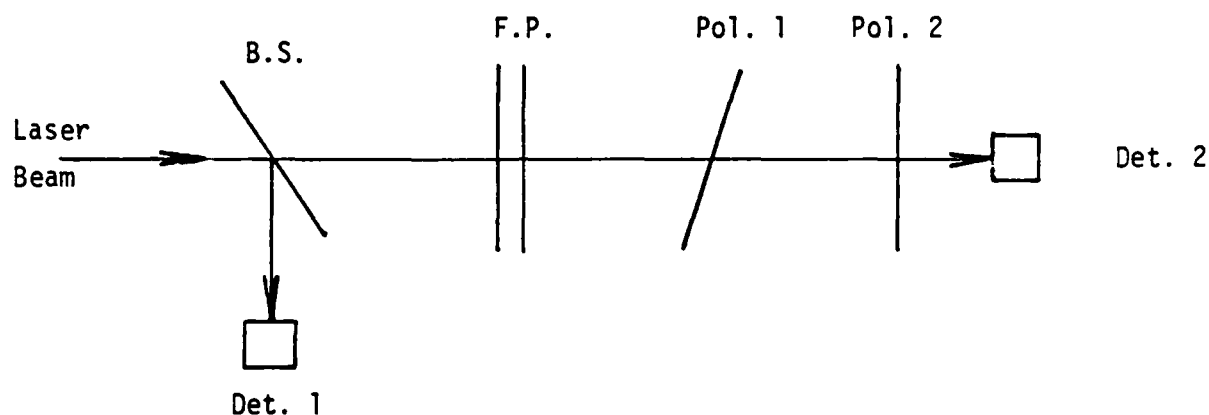
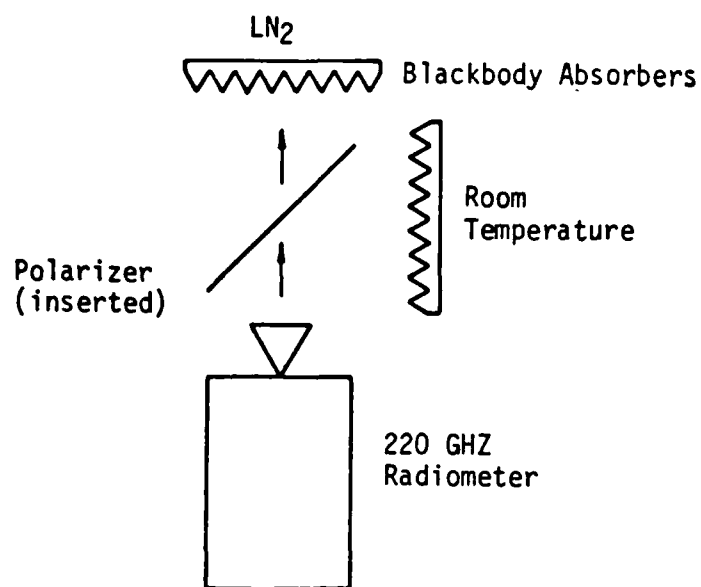


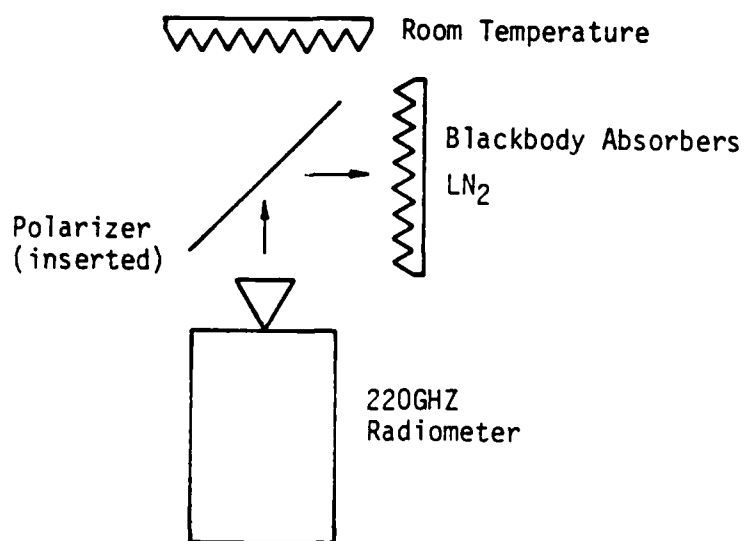
Figure C.6 Experimental arrangement for measuring the transmission of a mylar-aluminum polarizer, Pol. 2 with an optically pumped laser. Components are: B.S., beam splitter; F.P., Fabry-Perot interferometer; Det., golay cell detectors. Polarizer #1 has a strip spacing of 50.8 microns and a strip width of 12.7 microns on a Kapton substrate 12.7 microns thick.

Acknowledgement

The authors would like to acknowledge with thanks the use of laser and Fourier spectrometer facilities at Emory University's Physics Department and the cooperation of Dr. Sid Perkowitz.



a) Transmission Test



b) Reflection Test

Figure C.9 Transmission and reflection test setup using 220 GHz Radiometer.

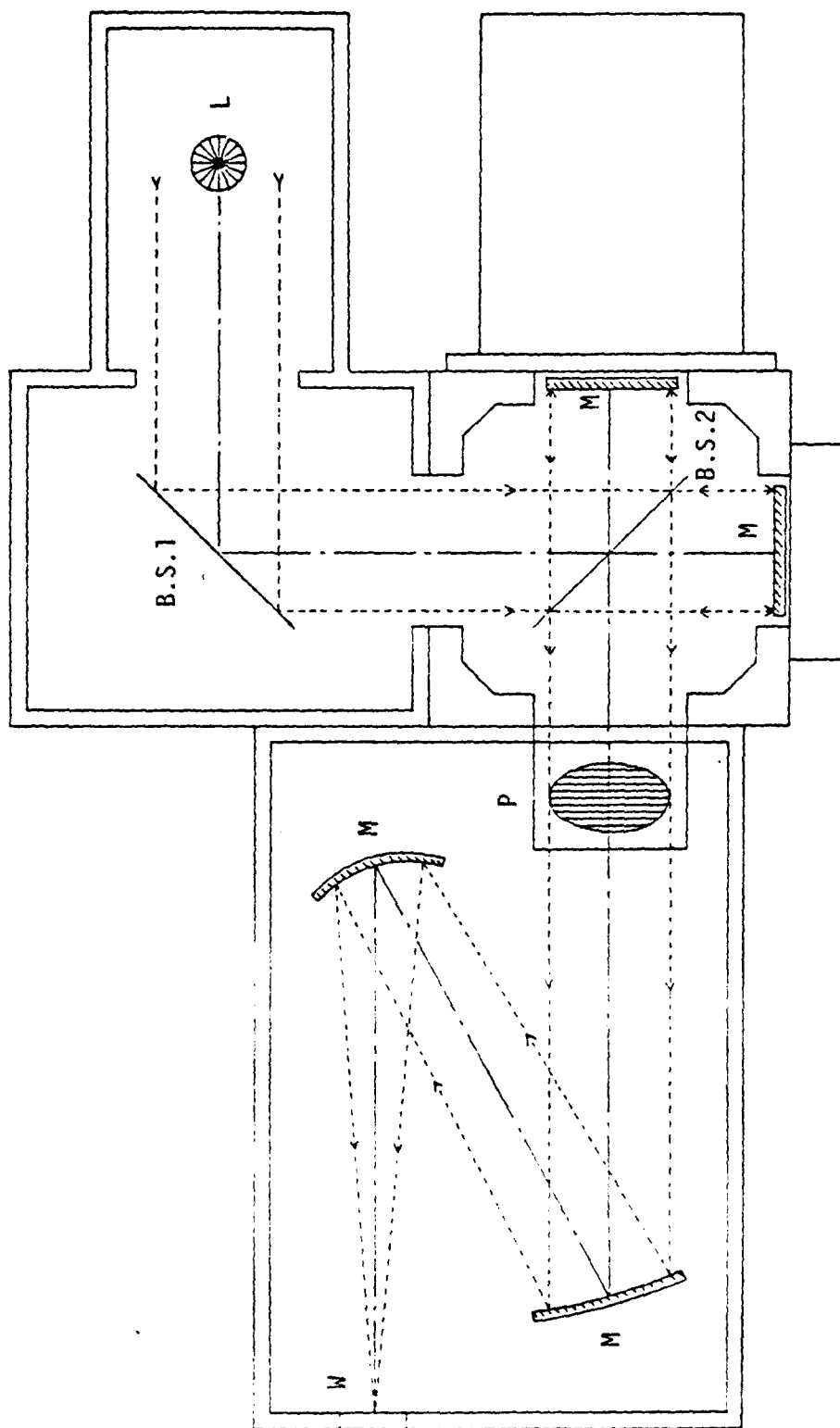


Figure C.8 The Fourier transform spectrometer. B.S.1 is a wire grid which produces a plane polarized output from the spectrometer. Components are: M, mirrors; B.S., beam splitters; L, Hg vapor lamp sources; P, polarizer; D, detector; W, polyethylene window.

A Fourier transform spectrometer in an arrangement shown in Figure C.8 was also used to make measurements of the transmission for the case of the polarization perpendicular to the strips in the same frequency range as Figure C.7. These results were in good agreement with the laser measurements, though of somewhat less accuracy.

A radiometer at 220 GHz having a sensitivity ΔT_{\min} of $< 0.1^\circ\text{C}$ was used to measure the loss introduced by the polarizing beamsplitter when inserted in front of the radiometer's horn antenna, as shown in Figure C.9a. The polarization of the horn was perpendicular to the grid strips. A loss value of 1% was found and is consistent with expectations based on the laser measurements. Similarly, reflection loss was measured, for the opposite relationship between the polarization and the strip orientation as shown in Figure C-9b, and found to be 1%. This is consistent with expected losses due to the transmission of this polarization (as may be estimated by extrapolation from the laser measurements) and due to absorption in the substrate and in the grid.

Finally, measurements have been reported elsewhere of the polarization ratio at 96 GHz. A value of 630 was found, which as expected is a little higher than that found at 220 GHz.

Acknowledgement

The authors are very grateful to Dr. G. Lamb of Goddard Space Flight Center for providing some sample grid polarizers for preliminary tests.

TABLE C.4 Polarization Ratios of the Grid Polarizer Measured
with a Laser Source

Frequency GHz	Polarization Ratio	
	Measured	Theoretical
525	500	5000
1841	150	260
2542	50	110

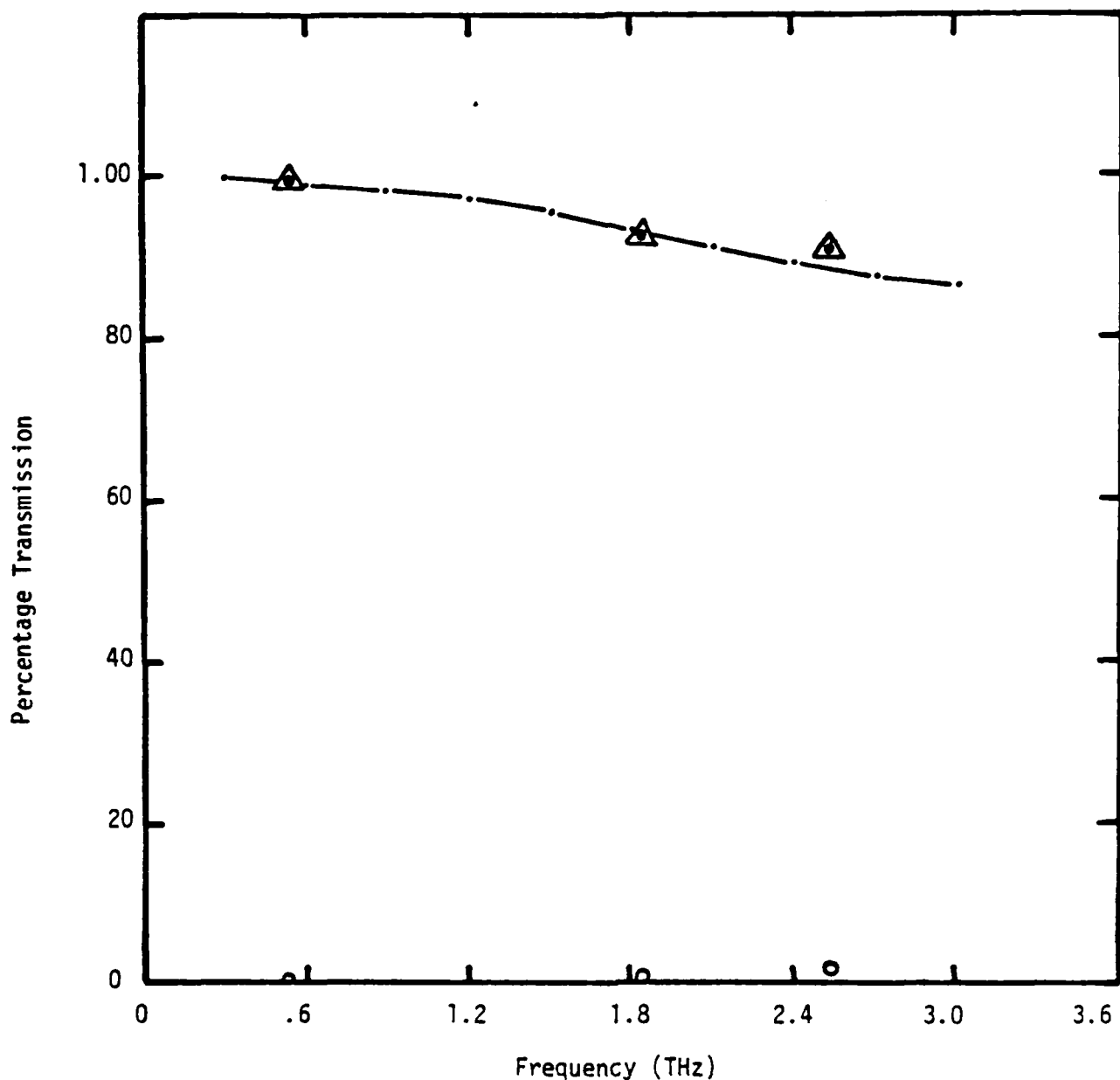


Figure C.7 Transmission Spectrum of a Mylar-Aluminum Strip Polarizer. Strip period 10 microns, strip width 4 microns, substrate thickness 6.35 microns. Measurements with a pumped laser: polarizer strips perpendicular to input polarization • ; polarizer strips parallel to input polarization ○ ; Mylar substrate only Δ. The theoretical curve — · — · — is for the case where the polarizer strips are perpendicular to the input polarization.

Atmospheric Effects on Near-Millimeter-Wave Propagation

RONALD A. BOHLANDER, ROBERT W. MCMILLAN, SENIOR MEMBER, IEEE, AND JAMES I. GALLAGHER, FELLOW, IEEE

Invited Paper

Utilization of the near-millimeter-wave band is limited by atmospheric effects on propagation. Although this paper is restricted to clear-air effects, it is pointed out that these phenomena, which are meteorological in origin, are also present to a significant degree in adverse weather. The paper surveys theoretical and observational knowledge concerning absorption, emission, refraction, and turbulence effects in clear air and in the spectral range 90 to 1000 GHz. Modeling practices are also reviewed.

I. INTRODUCTION

The effects of the atmosphere have been paradoxically both a hindrance and a boon to the development of near-millimeter-wave technology. For many years, this spectral range was handicapped, not only by formidable development problems, but also by concerns about atmospheric attenuation which is significantly higher than at longer wavelengths. A resurgence of interest in near-millimeter waves came about in response to problems at shorter wavelengths. Infrared systems, while able to operate in both day and night, are frequently unable to perform through clouds, fog, or smoke. Near-millimeter waves are able to penetrate these obscurants with reasonable compromises in range and angular resolution. Activity in near-millimeter-wave propagation research has increased in recent years in response to needs for better definitions of the limitations. In addition, it is recognized that certain processes in molecular physics or atmospheric optics can be studied with special advantage in this part of the electromagnetic spectrum.

A number of commendable reviews have appeared (e.g., [1]–[7]) which examine in some detail the available literature. The present review will not attempt to repeat their critical efforts but rather provide a relatively terse account summarizing what is known and what are the frontier issues. The review will cover effects of importance in the frequency range 90 to 1000 GHz and will be divided in two parts to be published separately. In this first part, the effects

of molecular absorption, emission, and refraction and those due to turbulence will be covered. These are normally thought of as clear-air phenomena, but they are also an important component of adverse weather effects, which will be reviewed in a later paper.

II. MOLECULAR ABSORPTION

A. Theory

The major molecular absorbers in the near-millimeter wavelength region are H_2O and O_2 . A few minor constituents can be seen weakly, such as O_3 , and have been the subject both of ground-based and high-altitude investigations (e.g., [8], [9]). However, these have a negligible impact on utilizations of the band for communications, radar, and the like. Molecular absorption at these frequencies occurs principally through the excitation of rotational transitions, and its strength is usually determined by the size of the molecule's electric dipole moment. For O_2 , oxygen is the weaker of the two principal absorbers because it is a homonuclear diatomic with no electric dipole moment. It is able to make relatively weak transitions since it exists in a triplet-sigma ground state with two uncoupled (electron) spins, which give the molecule a magnetic moment. Absorption due to O_2 shows up clearly not from its intrinsic strength but from the large concentration of it in the atmosphere. The water molecule, on the other hand, has a strong electric dipole, and in spite of the light atoms in the molecule, the spacing of the absorption resonances is relatively close due to the molecule's bent shape and the consequent asymmetry of its rotational inertia. Absorption resonances of both oxygen and water molecules are shown in the calculated spectrum in Fig. 1. The level of absorption between these resonances has a considerable contribution from the wings of strong resonances of water at higher frequencies.

An important tool in modeling atmospheric absorption is the compilation of atmospheric absorption resonance parameters which is maintained by the Air Force Geophysics Laboratory [10]; parallel efforts should also be recog-

Manuscript received September 11, 1984; revised September 1984. This on-going investigation by the authors in the areas reviewed in this paper is supported by the U.S. Army Research Office in two contracts (DAAG-29-80-K-0077 and DAAG-29-80-K-0078).

The authors are with Georgia Tech Research Institute, Georgia Institute of Technology, Atlanta, GA 30332, USA.

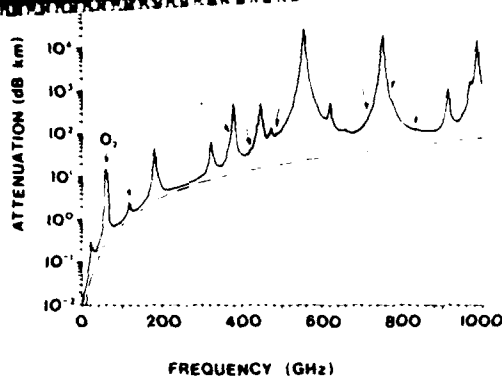


Fig. 1. Atmospheric absorption coefficient for a horizontal path near sea level calculated with the model in [37]. Solid line is the total predicted for absorption by water and oxygen molecules in the atmosphere. The positions of oxygen lines are indicated with arrows. The dashed line shows the continuum component of the model calculated with (2). Conditions assumed: $T = 288$ K, dry air pressure $P_d = 101.3$ kPa (1013 mbar), partial pressure of water vapor $p = 1.7$ kPa (17 mbar, i.e., saturated). After [37].

nized [11], [12]. A word about nomenclature is appropriate here. The term resonance, to denote regions of peak molecular absorption, is physically more satisfying; however, the convention in spectroscopy is to call these peaks "lines," and this paper will comply to avoid confusion with the literature. The AFGL tables comprise extensive lists of line positions, intensities, widths, and energy levels from which the absorption coefficient at a given frequency ν may be calculated according to

$$\alpha(\nu) = q \sum_i S_i f(\nu, \nu_i, \gamma_i) \quad (1)$$

where ν_i is the line position, S_i is the intensity, $f(\nu, \nu_i, \gamma_i)$ is a function which describes the shape of the lines, γ_i is the linewidth, and q is the concentration of the absorber. As shown, a simple summation is made over all lines in a band, since line-coupling effects may be neglected for atmospheric molecules in the near-millimeter spectrum [13]. Allowance is made for the temperature dependence of the line intensities with the help of tabulated energy levels, and for the temperature dependence of linewidths, with the help of detailed calculations for at least two temperatures [14], [15]. Since the width of lines in the troposphere arises from collisional broadening, this parameter depends on the barometric pressure and the partial pressure of the absorbing gas [14], [15]. As a result, in the gaps between lines, absorption by water vapor has two terms, one that increases linearly with water molecule concentration (line broadening by air), and one that increases quadratically with water molecule concentration (self-broadening). The accuracy of tabulated data on line parameters is reviewed in [10] and is generally adequate for modeling. Widths are difficult to measure, but by far the most uncertain item in any model is the shape of the lines a few linewidths away from line center, particularly when an entirely theoretical description is used.

Interest in the physics of line shape has been spurred in the near-millimeter spectrum since much of this region's utility lies in the intervals of frequency between lines, and there significant limitations are imposed by molecular absorption, even more so than in those regions commonly

used in the infrared. For many years, collisional line shape formulas have been used which were derived [16], [18] with a simplification known as the "impact approximation" in which it is assumed that collisions occur in infinitesimal intervals of time. This can give a fairly accurate picture of the line shape within intervals of frequency equal to a few times the linewidth since this regime corresponds to time intervals of the order of the time between collisions, or longer. (One can think of collisional line broadening as a kind of modulation process.) The details of the events within collisions begin to have an effect on the line shape as the frequency difference from a given line center approaches the reciprocal of the collision durations. Recent work has made progress in methods to include the finite duration of collisions in the theory [19], [20], and some general constraints on the shape of lines far from line center have been clarified. For frequencies distant from a given line by more than the reciprocal of typical collision durations, some type of exponential decrease is required in the line shape formula [21]. This represents less absorption in the far wings of lines than has been heretofore predicted by impact approximation formulas and is understandable as a smoothing of the modulation process. However, the inclusion of a mean collision duration is not the last hurdle to the development of an adequate theory, as may be seen from an appreciation of the physics of the collision process as well as from comparisons of observation with prediction.

The problem faced in understanding atmospheric spectra is that the water molecule, the prime absorber, undergoes molecular interactions complicated by relatively strong attractive forces which are to some degree not spherically symmetric due to the shape of the molecule. Attractive interactions are believed to be responsible for the observation of increased absorption between lines when temperature decreases. There has been a controversy about whether this absorption signals the formation of dimers or should be understood as monomer line wings sensitive to the attractive part of the potential energy of interaction. For simpler molecules (which have spherically symmetric shapes) absorption caused by unbound, metastable, and bound pairs can be predicted in the correct proportions at a given temperature [22], [23]. In general when the temperature is low by comparison with the binding energy of molecular pairs, dimers are numerous and play an important role in the absorption of such simple molecules. Although this condition is met for pairs of water molecules (the heat of formation is believed to be at least as large as 0.12 eV, as compared with $k_B T = 0.025$ eV [24]), the theory of the relative importance of different kinds of pair interactions has not been extended as yet to asymmetric molecules.

Microwave transitions of water dimers have been observed in molecular beams [25] and are consistent with the lowest energy structure calculated from molecular orbital theory (e.g., [26]). However, molecular beams provide what is an essentially very cold molecular environment, and an analysis of observed room-temperature laboratory spectra shows no band structures simply related to the known low-temperature form of the dimer [24]. If dimers do contribute a significant part of the absorption at room temperature, it would appear that they must exist in many structures different from the lowest energy form. While theory does not yet predict how the spectrum of the dimer evolves with increasing temperature, one would expect considerable changes since current calculations [26] indicate that the nonspherical part of the potential energy function,

which defines the particular configuration of lowest energy, is relatively weak.

In the complementary arena of line broadening theory, some progress is being made toward the inclusion of more aspects of the intermolecular potential energy, but a complete inclusion of what is known [26] will be a formidable undertaking. Thus a satisfactory, completely theoretical description of water vapor absorption is not presently available, and current models of atmospheric transmission are empirical.

B. Observations

There are several fairly recent reviews of data on the transmission of clear air or of atmospheric constituents measured in the laboratory [2], [6], [24], [27]. Such data are not easily obtained as may be elaborated briefly by the following generalizations concerning the various methods used.

1) Spectra can be obtained with Fourier spectroscopy, but available black-body, wide-band sources are weak, and require liquid-helium-cooled detectors and relatively long integration times for satisfactory results. Spectroscopy performed instead with multiple or tunable narrow-band sources sometimes requires tedious tuning operations, but generally offers greater accuracy at a given frequency.

2) Laboratory studies have the advantage of better control of the subject constituents, their pressures and temperatures, but the disadvantage of limited path lengths relative to the kilometer size links important in applications of the band. These frontiers have been pushed back through extreme care in fabrication of open-resonator cells [28] and through the development of large, untuned resonator cells [29].

3) In direct atmospheric research there is relatively greater difficulty in specifying the atmospheric conditions and, of course, a lack of control of these conditions, but in several on-going researches, a greater effort on characterization is being made. There are also difficulties in obtaining an absolute scale of transmission or absorption, since the atmosphere cannot be "pumped out" in order to obtain signals from the same experimental apparatus with no atmospheric absorption and thereby to make allowance for instrumental losses and losses due to beam divergence. Narrow-band measurements have something of an advantage in that the beam divergence in the far field can be calculated and experiments involving multiple paths can be analyzed in such a way that instrumental losses are eliminated [30]. Those who employ Fourier spectroscopy, and many who use narrow-band sources, must settle for relative transmission measurements from which the change of attenuation for a given change in humidity or temperature can be obtained. When the database is large enough, extrapolation to zero water vapor is possible [31], and an absolute scale for the important water vapor component can be established.

4) Slant-path radiometry has also been used to measure emission and absorption, but the difficulty of knowing the atmospheric constituent concentrations and temperatures over the path complicates the interpretation of the results.

Despite the diversity of methods, a consensus is forming on data of sufficient quality and consistency [2], [6], [24], [27] that an adequate basis exists to construct empirical models useful over a fair range of clear air conditions in the atmosphere. The spectrum in Fig. 1 illustrates such a calculation.

C. Anomalous Attenuation and Recent Work

Several significant researches have been reported since the reviews mentioned above which have been motivated by another controversy involving claims for the existence of anomalous attenuation ascribed to complexes of water of various sizes [32]–[34]. The conditions under which this is said to be observable are ones of high humidity with clear air or fog present, and ones of low temperatures in which relatively weakly bound complexes might plausibly be favored. Consequently, such conditions have been given more attention in recent work. Examples of anomalous absorption indications are given by a narrow-band laboratory study in a special untuned cavity at frequencies of 115–126 and 213 GHz [29], [35] and a Fourier spectroscopic investigation of atmospheric transmission in the range 150–870 GHz [36]. Both showed increases in specific attenuation with decreasing temperature (below 290 K) which were much larger than expected both by comparison with previously observed temperature dependences in higher temperature ranges and by consideration of the temperature dependences likely to be associated with energy levels in the water molecule and expected intermolecular interaction energies. Moreover, the absolute attenuations derived from these experiments were considerable in engineering terms; namely, in the range 5–20 dB/km at various frequencies between about 210 and 300 GHz, values which if correct would have a noticeable impact on applications of near-millimeter waves. A number of results have appeared since which do not show these effects and raise doubts concerning their validity.

A careful laboratory study has recently appeared of attenuation at 138 GHz [28]. An open resonator was used in which care was taken to avoid adsorbed layers of water on the reflecting surfaces which might add spurious attenuation. Results were obtained for temperatures of 282 and 300 K and for various mixtures of nitrogen and water vapor. This has been used to determine empirical corrections to model spectra (see below) which have been used to make comparisons with other data. No support for low-temperature or high-humidity anomalies was found and agreement with data in previously mentioned reviews [2], [6], [24], [27] is good. Reasonable agreement has also been found [37] with new results at 110 GHz [38], [39] in which techniques were used that were closely similar to those [29], [35] which previously showed anomalous attenuation, although an alternate analysis [39] still finds an anomalous low-temperature effect at several frequencies between 290 and 300 GHz, its contribution to total absorption is not large.

New Soviet studies have recently been described [40], [41] of measured attenuation in the frequency range 120–400 GHz over a 1.5-km-long atmospheric path. The zero of the attenuation scale was found by extrapolation from relative measurements at various humidities, a method that was mentioned earlier. Excellent signal-to-noise ratios were obtained, and no indication of anomalous temperature dependences or unexpected spectral features were found in the temperature range 263 to 282 K. Previous work by these investigators [42] is consistent with an absence of such effects, and recent Soviet laboratory results also support these conclusions [41].

Although proponents of the existence of anomalous absorption caution that their observations may apply to occasional nonequilibrium events [32], the tide appears to be running toward a belief that such conditions are either

quite rare or nonexistent. Nevertheless, recent activity spurred by this controversy has fostered significant improvements in millimeter-wave propagation models [28], [37], and further benefits can be anticipated.

D. Empirical Models of Clear-Air Transmission

There have been major efforts to develop computer models of near-millimeter-wave propagation at several national laboratories, the U.S. Air Force Geophysics Laboratory [43], [44], e.g., the U.S. Army Atmospheric Sciences Laboratory [45], and the National Telecommunications and Information Administration [28], [37], [46]–[48]. All have been extended to include effects of adverse weather, which will be considered in a later paper.

In the interest of computing speed, the general practice in these models is to compute the summation in (1) only for lines near the region of interest and to add to this a term that slowly increases with frequency. This represents all the contributions due to the wings of lines at other frequencies and due to other possible absorption mechanisms in water vapor which have been mentioned. It has been customary in this field to refer to this term as "continuum absorption" although this is not entirely consistent with previous usage in spectroscopy. Its magnitude has been determined by fitting to observations and thus compensates for the limitations which exist in current theory. In early empirical modeling efforts [49], data for limited conditions of barometric pressure, absolute humidity, and temperature were utilized in the fit, and thus there was inadequate underpinning to the assumptions made concerning the dependence of the magnitude of this term on those variables. In particular, inadequate attention was paid to the effect of self-broadening on the humidity dependence and to the steepness of the temperature dependence in the gaps between lines. A recent formulation of the continuum term α_c [28], [37] given by

$$\alpha_c = (0.397eP_vT^{-1} + 4605e^{-T^{-1}}) \nu \quad (2)$$

is much improved in this regard and is illustrated in Fig. 1 by the dashed curve. Here, the water vapor partial pressure ν is in kPa ($= 10$ mbar), the dry air pressure P_v is in kPa, frequency ν is in GHz, and the continuum absorption coefficient α is in dB/km. In another approach, a continuum has been derived from the wings of an empirically modified line shape that has been successfully fitted to data in parts of the millimeter- and near-millimeter-wave regions as well as to the infrared, with only four fitting parameters being necessary [43].

Comparisons between formulations of α_c , such as in [28], are difficult to make and assess since the lines included in the one-by-line part of a given model and the line shape formula used are seldom the same from one model to the next. These choices can have a dramatic effect not only on the magnitude of the complementary continuum term, but also, for example, on its apparent frequency dependence. Some workers show a continuum with a simple frequency dependence like that in (2) and others a continuum with two or more inflection points [2], [24], [27], [43]. The apparent temperature dependence of the continuum is similarly affected by the lines selected for explicit inclusion in a model calculation and may vary with frequency [24]. In the use of continuum formulas, it is useful to remember that this so-called continuum is not yet a separable physical

phenomenon but rather an artifice which is added in to simplify calculations and improve agreement with observations. Unnecessary discrepancies with observations can result when parts of a model are obtained from different sources and happen to be incompatible. There is a considerable need for future standardization of practice to avoid this source of confusion. Further work is underway on comparisons of the effectiveness of competing current models as regards agreement with observations. In the course of the present review, it was noted that the near-Soviet results [40], [41] mentioned above differ from predictions based on the model in [28], [37] by plus and minus 1–2 dB/km, depending on the frequency or conditions studied (see Note Added in Proof on p. 58).

Besides the advantages of computational speed from restricting the number of lines that are calculated explicitly, improvements have also been made in the speed with which regions near line centers can be calculated [43]. This has facilitated modeling of vertical or slant paths in which many layers are included in the calculation, some of which are at low pressures and consequently have very narrow lines. Fig. 2 is an example of such a calculation for a

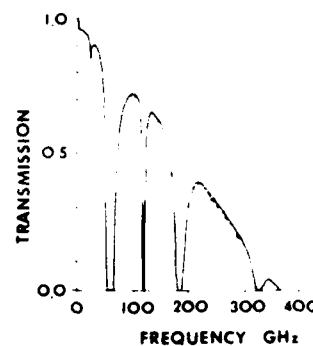


Fig. 2. Transmission of a vertical path through the U.S. Standard Atmosphere calculated with the AFGL EXST model [43]. The small line absorption lines (especially noticeable between 200 and 300 GHz) are due to minor atmospheric constituents such as ozone. After [43].

standard atmosphere from which the temperature profile in the gaps between lines is $\nu = 100$ GHz. The resulting paths with zenith attenuations which are less than 1 dB are one-way zenith transmission.

III. EMISSION AND REFRACTION

Emission and refraction by the atmosphere are treated only briefly since predictions of these phenomena can be derived in large measure from a knowledge of the absorption spectrum, provided that there is a good characterization of the meteorology of the region of interest. Emission is related to absorption by Kirchhoff's law [7], and refraction, by the Kramers-Kronig relationship [7].

A. Emission

In the near-millimeter and in the millimeter-wave regions, thermal energy emitted is proportional to the temperature of the emitting substance, in accordance with the Rayleigh-Jeans approximation. As a result, emission in these regions is frequently expressed in terms of "brightness temperature" T_B , or "antenna temperature" related to the power

P received from the atmosphere by a radiometer at frequency ν by [51]

$$P(\nu) = k_B T_B(\nu) \nu d\nu A \Omega / c \quad (3)$$

where $d\nu$ is the receiver bandwidth and A and Ω are the effective receiver areas and beam solid angles, respectively. If the atmosphere could be represented by one homogeneous slab of air, T_B would be given by

$$T_B = T_a(1 - t) + T_c(\nu)t \quad (4)$$

where t is the transmission through the slab, T_a is the air temperature, and the last term is due to the cosmic background and is small.

In (4) it is assumed that the atmosphere is in thermodynamic equilibrium, and thus its thermal emissivity, by Kirchhoff's law, is equal to its fractional absorption $(1 - t)$. Gradients with height of both temperature and molecular concentration are modeled by approximating the integral relationship

$$T_B(\nu) = \int_0^\infty T_a(z) K(\nu, z) dz + T_c(\nu)t \quad (5)$$

by a summation over thin spherical shells in the atmosphere which are taken to have uniform conditions. Here $K(\nu, z)$ is a weighting function which determines the contribution of the air temperature at altitude z to the sky brightness temperature and is given by

$$K(\nu, z) = \frac{d}{dz} t(0, z) \quad (6)$$

where

$$t(0, z) = 10^{-0.1 \int_0^z \alpha(z') dz'} \quad (7)$$

if α is expressed in dB/km.

When one wishes to determine the transmission of the atmosphere over vertical or slant paths, one can in principle point a radiometer at a source of radiation outside the atmosphere, such as the sun, and correct the received signal for what is known of the source radiance and the antenna coupling efficiency (both functions of frequency). In practice, these corrections are difficult and some simplifications may be realized if, instead, emission from the atmosphere is measured and the corresponding transmission is inferred [52]. If the distribution of atmospheric temperature with height is known, from radiosonde observations for example, measured spectra of T_B can be inverted through (5)–(7) to find the transmission of the path. If the water vapor distribution is also known or can be estimated, a mean radiating temperature can be assigned by a Curtis–Godson-type approximation [50], [53]. Then (4) can be used to obtain a simple approximate inversion to transmission. An example of data inverted by this means [52] is shown in Fig. 3 and compared with a calculation based on a recent empirical model [43].

This and other recent comparisons [37], [54], [55] between models and slant-path observations have shown reasonable agreement. The significance of these comparisons is tempered, however, by the scant amount of data available concerning the humidity and temperature profiles over the paths studied. Some workers have attempted to derive continuum expressions for use in empirical models on the basis of slant-path emission observations [52]. Although these do not greatly differ in predicted absorption from the

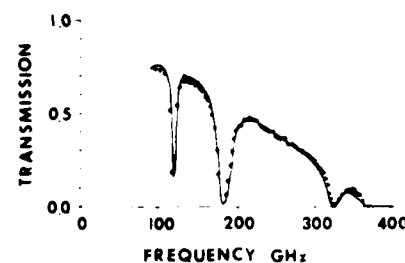


Fig. 3. Slant-path transmission inferred from emission measurements [52] (dots) and compared with a model calculation of transmission [43]. Slant secant = 1.72 . Integrated water vapor column density, derived from radiosonde data = 2.1 mm precipitable. After [43].

models referenced in the previous section, they should probably be given less weight of confidence than models based on laboratory or horizontal-path measurements where the atmospheric conditions can be better specified.

There is interest, of course, in levels of atmospheric emission for their own sake as they impact astronomical observations [52], [54], [55], communications [6], [56] and radiometric surveillance.

B. Refraction

In the near-millimeter-wave range, atmospheric refractivity can be described as a sum of a constant term N_0 derived from a sum of contributions by lines at all frequencies, and a dispersion term N_d , due to the water and oxygen lines in the region

$$N = N_0 + N_d \quad (8)$$

(Note: refractivity is equal to the refractive index minus one and is usually expressed in parts per million of unity, ppm, equivalent to the term N -units which is frequently seen.) In common with the radio-frequency and microwave regions of the spectrum, the nondispersive term used in near-millimeter-wave models [57]

$$N = K_1(P_d/T)Z_d^{-1} + K_2(e/T)Z_w^{-1} + K_3(e/T)Z_w^{-1} \quad (9)$$

depends strongly on the amount of water vapor present in the atmosphere (expressed here as the partial pressure e). This differs from the case in the visible or near-infrared parts of the spectrum, where the nondispersive refractivity depends almost entirely on barometric pressure (equal to e plus the partial pressure of dry air P_d) and temperature T . Equation (9) is not an exact theoretical form but, with $K_1 = 7.760$ K/kPa, $K_2 = 7.15$ K/kPa, and $K_3 = 3.750 \times 10^{-4}$ K/kPa, one which fits [57], [58] observations well. The factors Z_d and Z_w are nearly equal to unity [58], [59] and correct for the nonideal gas relation between density and pressure. It is interesting that a small but statistically significant discrepancy has been found [57] between the above values of K_2 and K_3 and those which best fit theoretical refractivity calculated from tables of line parameters. It has been suggested [57] that this indicates either an error in values of the strength of certain key lines in the water vapor pure rotation band or an effect of association by water molecules.

The dispersive term is calculated [37], [46], [47], [60], [61] as a summation over lines, similar to (1), but with a line shape derived from χ' by application of the Kramers–Kronig relation. A typical value of N_d is 350 ppm, and by compari-

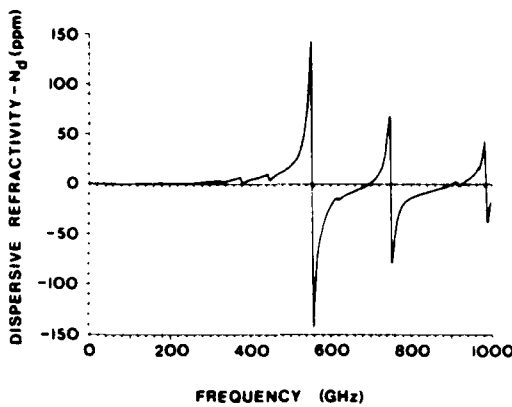


Fig. 4. The dispersive part of the atmosphere's refractivity calculated with the same model and conditions as in Fig. 1. For these conditions the total refractivity at 0 Hz is 350 ppm.

son, the dispersive term illustrated in Fig. 4 is important only in the vicinity of the strong lines, such as those at 557, 752, and 988 GHz. Observations of dispersion in the near-millimeter range are thus far available only at low resolution from dispersive Fourier transform spectroscopy [62], but no significant discrepancies with models have been identified.

The practical effects of clear-air refractivity are to produce phenomena which may be grouped into ones resulting from large-scale structures in the atmosphere, such as diurnal and weather changes, overall temperature and water vapor gradients or inversions, tidal effects, and the like, and those involving small-scale structures such as those produced by turbulence. The former will produce varying propagation delays, beam bending, beam ducting, multipath interference, etc. Except in the immediate vicinity of strong water vapor lines, as mentioned above, these effects should be closely similar to those found in the microwave region, since the refractivities in the two regions are very nearly equal and the sizes of the atmospheric structures are large compared with the wavelength in both cases. One distinction may, however, be found for multipath-type effects near the ground where reflected signals off the ground may contribute to a propagated wave. In this case, the ground effects will differ at near-millimeter-wave frequencies from those at lower frequencies due to significantly different scattering properties. Little experimental attention has thus far been given to these large-scale phenomena in near-millimeter-wave propagation. Studies are being made of the effects of small-scale phenomena, however, as described in the following sections.

IV. TURBULENCE

When the wind carries inhomogeneities in the atmosphere through a propagation path, fluctuations in several properties of the propagation result. In clear air, turbulence is the cause of inhomogeneities in both the refractive index and the absorption coefficient of the air. The refractive variations explain the familiar visible phenomena of star twinkling and the shimmering of distant images on a horizon on a hot day. Many aspects of the effects at visible and near-infrared wavelengths have been explored, after seminal theoretical work by Rytov [63], Chernov [64], and Tatarski [65], and detailed reviews are available [5], [66], [67].

Significant work has also been done in the microwave region (e.g., [68]), but millimeter-wave or near-millimeter-wave studies have only recently been given prominent attention. The possible propagation effects which may be catalogued are fluctuations in received intensity, angle of arrival, propagation delay, frequency, and polarization, of which the first three may be expected to be significant at near-millimeter wavelengths. In image formation, the phenomena can be manifested as scintillation, image dancing, and image blooming, of which the first two are important at such wavelengths.

As pointed out in [3], turbulence effects have sometimes been discounted for near-millimeter waves, since scattering by turbulent eddies is a diffractive effect, which naturally is stronger at shorter wavelengths. This is demonstrated by the following expression for the expected log-intensity variance of a received signal [60]:

$$\sigma_{\ln I}^2 = 0.496 k^{-1/6} L^{11/6} \left[1 - 2.73 \left(\frac{L_0}{\sqrt{L/k}} \right)^{1/3} \right] \quad (10)$$

in which k is the wavenumber $2\pi/\lambda$, L is the propagation path length, L_0 is the size of the largest turbulence eddies, and C_n^2 is the refractive index structure parameter, a measure of the spatial variance of refractive index. The reason that turbulence effects cannot be neglected in the near-millimeter-wave picture is the significant contribution by water vapor to the refractive index that distinguishes this regime from shorter wavelength regions, as mentioned earlier, and the fact that water vapor inhomogeneities in the atmosphere can be large. Fluctuating signal strength is not the only propagation issue of interest. Since at these wavelengths, high-precision tracking and adequate image formation systems may be constructed with antennas of moderate size, it is particularly of interest to know whether fluctuations in angle of arrival may show up as significant [69].

The near-millimeter-wavelength regime is of considerable interest for a number of other reasons. Some controversy has arisen over the interpretation of observations near the center of water vapor lines of moderate strength where the refractive index must be treated as complex, as will be discussed further in later sections. Such frequencies are of practical interest as possible choices for controlled-range communication links. Another distinction from shorter wavelengths is that near-millimeter wavelengths are no longer much smaller than turbulent eddies, but rather are comparable with the smallest ones. This so-called inner scale of turbulence L_0 is of the order of a few millimeters. On the other hand, it is possible to construct antennas or antenna arrays which are as large as the largest eddies, or the outer scale of turbulence L_{∞} , which ranges from a meter to a few meters in size for propagation near the ground, and possible to have propagation ranges for which the Fresnel zone of size $\sqrt{\lambda L}$ is also comparable with L_0 . This has given investigators an opportunity for interesting tests and extensions of theoretical models.

A. Theory

If one may assume that turbulent eddies are distributed in the neighborhood of a propagation path in a homogeneous and isotropic fashion, the Kolmogorov model [66] of the eddy spectrum says that the refractive index spatial

variance is proportional to the two-thirds power of the separation of two measurement points Δr when Δr is between ℓ_0 and L_0 , i.e.,

$$\langle \Delta n^2 \rangle = C_n \Delta r^{-1/3} \quad (11)$$

The brackets denote ensemble averages which can usually be replaced by time averages (according to an ergodic hypothesis). The constant of proportionality C_n , which also appeared in (10), is the key refractive index structure parameter relating the turbulence structure to the resulting optical effects. In general, the index of refraction must be considered to be complex, and strictly, terms should be added to (10) for the contributions of the variance of the real and imaginary parts and for the covariance of these components. The terms involving the imaginary part are due to spatial variations in absorption, and it has been estimated that, except in special circumstances, the contribution of absorption to fluctuations will be difficult to observe in the near-millimeter-wavelength range [60], [61]. The discussion will return later to this topic, but for the time being can be simplified by ignoring the terms involving the imaginary part of the refractive index.

Since both air density and water vapor concentration affect the refractive index, the structure parameter C_n can be expressed in terms of analogous structure parameters for temperature, humidity, and barometric pressure. Pressure variations can generally be neglected [60], and C_n is given by

$$C_n = A_T \frac{C_T}{\langle T \rangle^2} + A_Q \frac{C_Q}{\langle Q \rangle^2} + 2A_T A_Q \frac{C_{TQ}}{\langle T \rangle \langle Q \rangle} \quad (12)$$

where the A coefficients have been calculated from the refractive index spectrum [60], [61] and Q denotes water vapor concentration. Frequently, the earth's surface evaporates or transpires a considerable amount of water vapor. In these instances, the humidity fluctuations in the boundary layer are considerably larger in relative terms than the temperature fluctuations [60], [70], say

$$\frac{C_Q}{\langle Q \rangle^2} \approx 10^4 \frac{C_T}{\langle T \rangle^2}$$

and humidity variance dominates the refractive index structure. This can result in values of the near-millimeter wave C_n which are larger by an order of magnitude or more than ones in the infrared, which are mainly sensitive to temperature structure.

That this is not always the case may be seen from the following considerations. The last term in (12) is proportional to the covariance of temperature and humidity, $C_{TQ} = \langle \Delta T \Delta Q \rangle / \Delta r^{-1/3}$ which can generally be approximated for the boundary layer by [60]

$$\frac{C_{TQ}}{\langle T \rangle \langle Q \rangle} = \pm \left[\frac{C_Q}{\langle Q \rangle^2} \frac{C_T}{\langle T \rangle^2} \right]^{1/2} \quad (13)$$

The positive sign is usually found during the day and the negative sign during the night, due to a change in the direction of the temperature gradient near the ground. Since A_T is negative (i.e., refractive index decreases with increasing temperature), the last term in (12) acts to reduce the near-millimeter-wave refractive index structure. Under some dry conditions, it can substantially cancel the contribution of the other two terms [71] and result in a situation

for which the value of C_n is smaller in the near-millimeter region than in the near infrared.

A formulation was given earlier in (10) for the expected level of intensity fluctuations that applies [60] when 1) the wavefronts are spherical, 2) the transmitting and receiving antennas are small relative to a Fresnel zone $\sqrt{\lambda L}$, and in turn, 3) the Fresnel zone is small compared with the outer scale L_0 . The corresponding expression for angle of arrival variance is [64]

$$\sigma_A^2 = 0.54 L C_n^2 \rho^{-1/3} \quad (14)$$

where ρ may be interpreted as the spacing of small antennas (or the width of a large antenna) used in measuring the angle. Since with two or more antennas in an array, one actually measures the phase difference variance, known as the phase structure function D_ϕ , an alternate description is

$$D_\phi = \langle \Delta \phi^2 \rangle = 1.09 k^2 L C_n^2 \rho^{5/3} \quad (15)$$

where, in both (14) and (15), the dependence on ρ holds when $\sqrt{\lambda L} < \rho < L_0$ [72]. At larger antenna spacings, one can sense the outer scale by a drop-off in the slope of D_ϕ with ρ . A transverse coherence length ρ_0 is sometimes used which is the value of ρ for which $D_\phi = 2 \text{ rad}^2$. Since in the near-millimeter-wave range antennas are usually smaller than or comparable with ρ_0 , the main source of image degradation expected from turbulence is from image dancing rather than image blooming.

In early derivations of expressions such as (10), (14), and (15), it was assumed that scattering by eddies was weak (i.e., that scattering angles were small) and to reinforce this assumption, it was additionally assumed that $\lambda^3 L \ll \ell_0^4$, or more simply, that $\lambda \ll \ell_0$. Whereas these inequalities are readily satisfied at visual wavelengths, they are not so in the near-millimeter range, where $\lambda \sim \ell_0$. It is reasonable to ask whether small eddies are able to sustain significant resonant scattering in this regime, similar to that familiar in Mie scattering from rain drops. However, recent work [73]–[75] has shown that the formulas derived under the assumption of weak scattering are still a good approximation when $\lambda > \ell_0$ provided that $\lambda < \rho_0$ or L_0 .

An important dimension underlying the phenomena discussed thus far is the spatial spectrum of turbulent eddies and the resulting time spectra of modulations in propagation. Between the inner and outer scales of turbulence, the Kolmogorov model gives [67]

$$\Phi_n(\kappa) = 0.033 C_n^2 \kappa^{-11/3} \quad (16)$$

for the spectrum of refractive index as a function of spatial wavenumber κ . For smaller scales (larger wavenumbers than $2\pi/\ell_0$), refractive index variations are small and a Gaussian tail can be added to (16) [65], [67]; for larger scales (smaller wavenumbers than $2\pi/L_0$), turbulent phenomena merge with the large-scale variations in the atmosphere that were enumerated in Section III-B and are ill-defined in form. In general, the variations in refractive index continue to increase in size as the wavenumber decreases below $\kappa = 2\pi/L_0$ but with some decrease in slope until some considerably smaller wavenumber is reached.

When a transverse wind carries the turbulence structure through a propagation path, the spatial spectrum helps to determine the resulting modulation spectrum for propagating electromagnetic waves. An approximation that is frequently invoked is that turbulent eddies are "frozen in";

i.e., last for times which are long by comparison with the time taken to cross the path. Not all eddies are equally effective in creating modulation, and so fluctuation spectra measured in a propagation experiment do not closely parallel (16). For instance, eddies approximately equal in size to the Fresnel zone are particularly effective in producing intensity fluctuations, and the resulting spectrum of such fluctuations does not fall off rapidly with increasing frequency f until $f > f_0 = v(2\pi\lambda L)^{-1/2}$ [76], as illustrated in Fig. 5(a), where v is the cross wind speed. For fluctuations in the phase difference between two receivers separated by ρ , eddies of a scale similar to ρ are particularly effective, and the fluctuation spectrum has the form illustrated in Fig. 5(b). In contrast, the total phase in a link fluctuates slowly with a spectrum dominated by the largest scales in turbulence and by the other large-scale phenomena which have been mentioned. For this reason, it is not meaningful to give an expression analogous to (15) for the overall phase

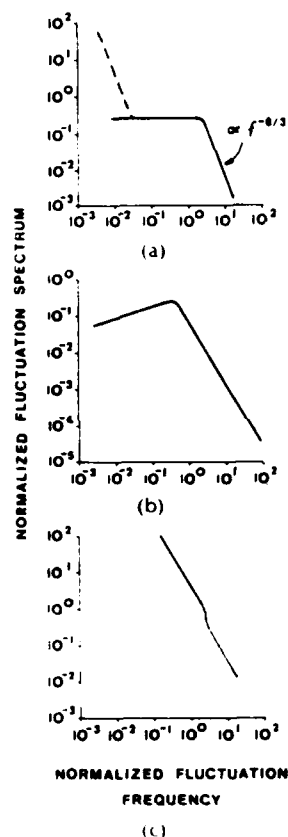


Fig. 5. Theoretical form of fluctuation spectra for the propagation of spherical electromagnetic waves [76]. (a) Log-intensity spectral density normalized by multiplying by the factor f_0/σ_{η}^2 . Frequency scale normalized by dividing the fluctuation frequency f by $f_0 = v(2\pi\lambda L)^{-1/2}$ where v = cross wind speed. The dashed line shows expected low-frequency behavior when absorption adds significant fluctuations. The exact frequency where it joins the solid line will depend on relative importance of absorption and refraction [81]. (b) Phase difference spectral density normalized by dividing by the phase structure function D_ϕ . Frequency scale normalized by dividing the fluctuation frequency f by v/ρ , where ρ is the spacing of the points with different phase. (c) Total phase fluctuation spectral density normalized by multiplying by the factor $1/\sigma_{\eta}^2$. The fluctuation frequency scale is normalized as in (a).

variance [67]. In summary, for Fresnel zones which are typically one to a few meters in size and for receiver antennas or arrays of the order of one to a few meters in size, the important fluctuation frequencies are expected to be in the low part of the audio spectrum in clear air turbulence.

B Observations

The preponderance of experimental efforts have thus far been directed at intensity fluctuation effects as these require less apparatus. The frequency dependence [70]–[77] and path length dependence [70] in (10) have been verified by simultaneous observations at multiple frequencies in ranges covering 36 to 230 GHz and over paths of different lengths. Expected changes when the outer scale L_η happens to become smaller than a Fresnel zone have also been observed [77]. Less attention heretofore has been given to verification of the refractive index factor in (10) due to the requirement for a considerable investment in micrometeorological instrumentation to enable predictions of C_n^2 to be made. This need was perceived in recent years [68] and several significant efforts are now underway. A comparison of observed microwave values of C_n^2 with ones calculated from measured values of C_0^2 , C_T , and $C_{\text{H}_2\text{O}}$ has shown reasonable agreement [71]. Observations have recently been obtained for near-millimeter-wave intensity fluctuations (in the range 116 to 173 GHz) as well as the detailed micrometeorological parameters [72]–[74], and a direct test of (10) will thus be possible.

Observations of the spectrum of intensity scintillation have also netted interesting results. The general form of Fig. 5(a) has been confirmed [79], including the expected falloff with fluctuation frequency to the $-8/3$ power at high frequencies [76]. Studies in the neighborhood [80], [81] of the oxygen absorption band near 55 GHz, somewhat below the near-millimeter range, have demonstrated that inhomogeneities in absorption in the atmosphere produce an expected increase [81]–[83] in fluctuations at low fluctuation frequencies, above those due only to the real part of the refractive index, as sketched by the dashed line in Fig. 5(a). One would expect similar effects to be observed near significant water vapor absorption lines in the near-millimeter-wave region.

Observations have been reported, however, of effects which have the opposite sense; namely, striking decreases (by a factor of five) in the relative intensity fluctuation levels in the center of a moderately strong water vapor line near 325 GHz [84], [85], as compared with nearby regions between lines. Attempts at theoretical treatments [65]–[66] have taken account of the fact that propagation paths have to be much shorter in such instances due to the high level of absorption (30 dB or more) and thus refractive scattering can become relatively more important than diffractive scattering. Although it has been shown that in particular circumstances, a decrease in fluctuations can occur, present theories predict much smaller decreases than those observed [85], [86]. A small departure has also been reported [87] from the usually expected log-normal distribution of intensity for a region of high absorption in the millimeter-wave spectrum. There is an opportunity here for further work to consolidate the picture of phenomena that accompany high absorption, which are of more than academic

interest due to potential applications in the communications field, for example. In further investigations, it would be advisable to eliminate some of the existing uncertainty through observations supported by detailed micrometeorology of the temperature and humidity structure.

Relatively little attention has been given until recently to the important topic of angle of arrival or phase difference fluctuations. Apart from measurements conducted at microwave frequencies [68], there were some observations near 150 GHz based on the use of a receiver which switches between two apertures, which showed angle of arrival fluctuations with a standard deviation of about $100 \mu\text{rad}$ [88]. The present authors, with collaborators from the National Oceanic and Atmospheric Administration and the U. S. Army Atmospheric Sciences Laboratory, have been engaged in a new study in the frequency range 116 to 173 GHz that covers both intensity and angle of arrival effects [78]. It is being conducted over extremely flat and uniform ground cover to eliminate as many complications as possible to the turbulent structure. Simultaneous measurements of the micrometeorological parameters that characterize humidity and temperature structure are being made along with observations of standard meteorological parameters. Near- and mid-infrared scintillations are also recorded. Measurements have been conducted in a wide range of weather conditions throughout one year, but are at the time of writing in only a very preliminary state of reduction. The angle of arrival measurements are derived from a 10-m-wide by 1.5-m-high interferometric receiver array, and an example of results typical of summer daytime conditions dominated by humidity fluctuations is given in Fig. 6 as a function of horizontal receiver spacing. The Kolmogorov $5/3$ power law (15) is shown for comparison, and one can

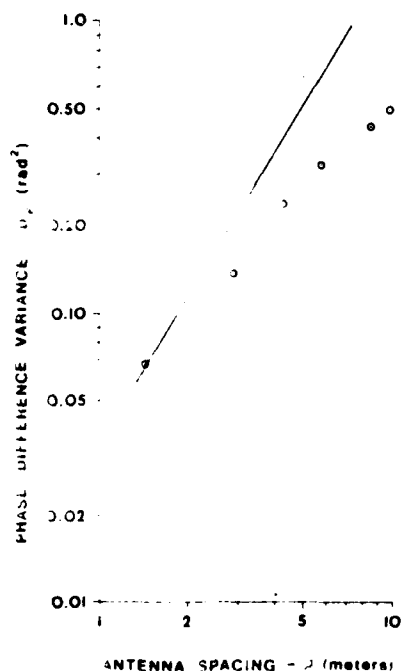


Fig. 6 Observed phase structure function (dots) at 173 GHz during a clear, sun-shining near-midday in the summer [78]. The straight line shows the Kolmogorov $5/3$ power-law comparison. The departure at the larger spacings is due to a departure from a similarity between the size of the separations and the outer scale of turbulence.

see clearly the expected departure at larger spacings due to the effects of the finite size of the outer scale of turbulence [72].

In the longer term, such studies will be useful in affording the opportunity for detailed comparisons with theory, but for the present they have also provided useful orientations concerning the qualitative importance of various types of weather in producing degradation in propagation due to turbulence (or turbidity from suspended or falling hydrometeorites). Summertime conditions when transpiration or evaporation of humidity are strong have provided the largest fluctuations yet seen. Over a path of about 1.4 km, intensity fluctuations up to 40 percent peak-to-peak and angle of arrival fluctuations of a few hundred microradians have been observed. At the other end of the spectrum have been fog conditions in stationary air, for which fluctuation levels have been about thirty times lower [78]. Generally, precipitation events have provided intermediate levels of fluctuations. This may at first seem surprising since during a rain storm, for example, there is plenty of available humidity and, in addition, fluctuations from scattering by rain. Offsetting those influences which increase the effect of turbulence, is a typical decrease due to cloud cover and the removal of strong heating at the ground. Even so, of the factors which increase the fluctuations during a storm, preliminary indications appear to rank the humidity effects as being the most important [78], pretty much in line with expectation [89]. This stresses the importance of the study of turbulence not only in clear air but also as it is superimposed on adverse weather.

The discussion of turbulence effects in this review has been confined essentially to horizontal paths fairly near the ground where the atmospheric conditions can be reasonably uniform and readily characterized by *in situ* measurements. Little attention has been given to turbulence effects on near-millimeter-wave propagation over slant paths. One might argue that slant-path effects will be smaller in most regards due to shorter interactions with the layers nearest the ground where the refractive index structure constant is expected to be highest. The foregoing discussion has also been restricted to spherical wavefronts as these are often encountered in practice. However, models for planar and beam-wave cases also are available (e.g., [27], [28]).

V. CONCLUDING REMARKS

An understanding of the effects of the clear atmosphere on near-millimeter-wave propagation is fundamental to a wider understanding of effects in all types of weather. A few of the salient needs for further work, which were discussed in the preceding sections, will be outlined here.

1) Present models of nonresonant absorption by water vapor, the so-called continuum between the lines, are empirical. A breakthrough to an *a priori* description of the role of the molecular attractive forces of water in collision broadening of absorption lines and in dimer formation would be of major consequence. It would provide a better understanding of hydrogen bonding for a key molecule as well as better predictions of atmospheric absorption as a function of temperature.

2) Even within empirical approaches to predictions of atmospheric absorption, there is room for improvement. Much needless confusion arises by a lack of standardization

over the definition of what nearby lines to include in explicit line-by-line calculations. There is little on which to base a choice, but the procedure used by the investigators at the U.S. Air Force Geophysic Laboratory [43] has the advantage that it is useable over a wide spectral range. An effort to bring about standardization and a consolidation of present observations and predictions into a format where more thorough comparisons can be drawn would be welcomed.

3) The discrepancy between theory and the observed temperature dependence of the radio-frequency refractivity is tantalizing [57]. The phenomenology of large-scale refractive effects at near-millimeter wavelengths, such as beam bending and multipath propagation, have so far been given little attention.

4) Greater prominence is now being given to studies of turbulence effects. Several interesting confirmations of theory have been completed and many more comparisons are in the offing. One puzzle which has appeared is the report of a strong diminution of intensity fluctuations near the center of a line at 325 GHz (e.g., [85]).

Important effects in adverse weather will be covered in a future publication.

Note Added in Proof

The author recently received a preprint of an article by H. J. Liebe in which revisions of the model in [28], [37] are presented. The improvements are based on revised line data and a more refined analysis of data obtained in his laboratory. They appear to bring the model into substantially better agreement with the Soviet data [40], [41].

ACKNOWLEDGMENT

The authors would like to acknowledge helpful discussions with S. F. Clifford, R. J. Hill, H. J. Liebe, and J. T. Priestley.

REFERENCES

- [1] J. W. Waters, "Absorption and emission by atmospheric gases," in *Methods of Experimental Physics*, vol. 12B, M. L. Meeks, Ed., New York: Academic Press, 1976, ch. 23.
- [2] D. E. Burch and D. A. Gryvnak, "Continuum absorption by H₂O vapor in the infrared and millimeter regions," in *Atmospheric Water Vapor*, A. Deepak, T. D. Wilkerson, and L. H. Ruhnke, Eds., New York: Academic Press, 1980, pp. 47-76.
- [3] S. M. Kulpa and E. A. Brown, "Near-millimeter wave technology base study, vol. 1: Propagation and target/background characteristics," U.S. Army Harry Diamond Laboratory Rep. HDL SR-79-8, chs. 1-2, Nov. 1979.
- [4] T. Oguchi, "Electromagnetic wave propagation and scattering in rain and other hydrometeors," *Proc. IEEE*, vol. 71, pp. 1072-1078, Sept. 1983.
- [5] R. L. Fante, "Electromagnetic beam propagation in turbulent media: an update," *Proc. IEEE*, vol. 68, pp. 1424-1443, Nov. 1980.
- [6] R. K. Crane, "Fundamental limitations caused by RF propagation," *Proc. IEEE*, vol. 69, pp. 196-209, Feb. 1981.
- [7] R. J. Emery and A. M. Zavody, "Atmospheric propagation in the frequency range 100-1000 GHz," *Radio Electron. Eng.*, vol. 19, pp. 770-790, July-Aug. 1979.
- [8] J. E. Barnes, "Infrared and submillimeter spectroscopy of the atmosphere," in *Infrared and Millimeter Waves*, vol. 6, K. J. Button, Ed., New York: Academic Press, 1982, ch. 1.
- [9] K. F. Kunzi and E. R. Carlson, "Atmospheric CO volume mixing ratio profiles determined from ground-based measurements of the J = 1 - 0 and J = 2 - 1 emission lines," *J. Geophys. Res.*, vol. 87, no. C9, pp. 7235-7241, Aug. 20, 1982.
- [10] L. S. Rothman, R. R. Gamache, A. Barbe, A. Goldman, J. R. Gillis, L. R. Brown, R. A. Toth, J.-M. Flaud, and C. Camy-Peyret, "AFGL atmospheric absorption line parameters compilation 1982 edition," *Appl. Opt.*, vol. 22, pp. 2247-2256, Aug. 1, 1983.
- [11] J.-M. Flaud, C. Camy-Peyret, and R. A. Toth, *Selected Constants, Water Vapour Line Parameters from Microwave to Medium Infrared*, Oxford, England: Pergamon, 1981.
- [12] J. K. Messer, F. C. De Lucia, and P. Helminger, "The pure rotational spectrum of water vapor—A millimeter, submillimeter, and far infrared analysis," *Int. J. Infrared Millimeter Waves*, vol. 4, pp. 505-539, 1983.
- [13] K. S. Lam, "Application of pressure broadening theory to the calculation of atmospheric oxygen and water vapor microwave absorption," *J. Quant. Spectrosc. Radiat. Transfer*, vol. 17, pp. 351-383, 1977.
- [14] W. S. Benedict and L. D. Kaplan, "Calculation of line widths in H₂O-N₂ collisions," *J. Chem. Phys.*, vol. 30, pp. 388-399, 1959.
- [15] ———, "Calculation of line widths in H₂O-H₂O and H₂O-CO collisions," *J. Quant. Spectrosc. Radiat. Transfer*, vol. 4, pp. 453-469, 1964.
- [16] J. H. Van Vleck and V. F. Weisskopf, "On the shape of collision-broadened lines," *Rev. Mod. Phys.*, vol. 17, pp. 227-236, Apr.-July, 1945.
- [17] E. P. Gross, "Shape of collision-broadened spectral lines," *Phys. Rev.*, vol. 97, pp. 395-403, 1955.
- [18] D. L. Huber and J. H. Van Vleck, "The role of Boltzmann factors in line shape," *Rev. Mod. Phys.*, vol. 32, pp. 147-148, 1966.
- [19] S. A. Clough, F. X. Kneizys, R. Davies, R. Gamache, and R. Tipping, "Theoretical line shape for H₂O vapor: Application to the continuum," in *Atmospheric Water Vapor*, A. Deepak, T. D. Wilkerson, and L. H. Ruhnke, Eds., New York: Academic Press, 1980, pp. 25-46.
- [20] G. Birnbaum, "The shape of collision broadened lines from resonance to the far wings," *J. Quant. Spectrosc. Radiat. Transfer*, vol. 21, pp. 597-607, 1979.
- [21] R. W. Davies, R. H. Tipping, and S. A. Clough, "Dipole autocorrelation function for molecular pressure broadening: A quantum theory which satisfies the fluctuation-dissipation theorem," *Phys. Rev. A*, vol. 26, pp. 3378-3394, 1982.
- [22] D. E. Stogryn and J. O. Hirschfelder, "Contribution of bound, metastable, and free molecules to the second virial coefficient and some properties of double molecules," *J. Chem. Phys.*, vol. 31, pp. 1531-1545, 1959; Errata, vol. 33, pp. 242-243, 1960.
- [23] A. T. Prengel and W. S. Cornall, "Raman scattering from colliding molecules and Van der Waals forces in 2-propanol methane," *Phys. Rev. A*, vol. 1, pp. 170-171, 1970.
- [24] R. A. Bohlander, R. J. Emery, D. T. Llewellyn-Jones, G. Gimmetstad, H. A. Gebbie, O. A. Simpson, L. E. Jaeger, and S. Perkowitz, "Excess absorption by water vapor and comparison with theoretical dimer absorption," in *Atmospheric Water Vapor*, A. Deepak, T. D. Wilkerson, and L. H. Ruhnke, Eds., New York: Academic Press, 1980, pp. 241-254.
- [25] T. R. Dyke, K. M. Mack, and J. S. Muenster, "The structure of water dimer from molecular beam electric resonance spectroscopy," *J. Chem. Phys.*, vol. 66, pp. 1384-1391, Jan. 1, 1977.
- [26] E. Clementi and P. Habitz, "A new two-body water-water potential," *J. Phys. Chem.*, vol. 87, pp. 1237-1241, 1983.
- [27] D. E. Burch, "Continuum absorption by atmospheric H₂O," *Proc. SPIE (Atmospheric Transmission)*, vol. 177, pp. 1-10, 1981.
- [28] H. J. Liebe, "The atmospheric water vapor continuum below 300 GHz," *Int. J. Infrared Millimeter Waves*, vol. 2, pp. 207-227, 1984.
- [29] D. T. Llewellyn-Jones, "Laboratory measurements of absorption by water vapour in the frequency range 100-1000 GHz," in *Atmospheric Water Vapor*, A. Deepak, T. D. Wilkerson, and L. H. Ruhnke, Eds., New York: Academic Press, 1980, pp. 255-264.
- [30] A. B. Crawford and D. C. Hogg, "Measurement of atmospheric attenuation at millimeter wavelengths," *Bull. Sect. Tech. J.*, vol. 35, pp. 907-916, July 1956.

- [31] Yu. A. Drvagin, A. G. Kislyakov, L. M. Kukin, A. I. Naumov, and L. I. Fedoseev, "Measurement of the atmospheric absorption in the range 1.36–3.0 mm," *Izv. VUZ. Radiofizika*, vol. 9, no. 6, pp. 1078–1084, 1966.
- [32] H. A. Gebbie, "Observations of anomalous absorption in the atmosphere," in *Atmospheric Water Vapor*, A. Deepak, T. D. Wilkerson, and L. H. Ruhnke, Eds. New York: Academic Press, 1980, pp. 133–141.
- [33] ———, "Resonant absorption by water polymers in the atmosphere," *Nature*, vol. 296, pp. 422–424, Apr. 1, 1982.
- [34] H. R. Carlson and C. S. Harden, "Mass spectroscopy of ion-induced water clusters. An explanation of the infrared continuum absorption," *Appl. Opt.*, vol. 19, pp. 1776–1786, June 1, 1980.
- [35] D. T. Llewellyn-Jones, R. J. Knight, and H. A. Gebbie, "Absorption by water vapour at 7.1 cm^{-1} and its temperature dependence," *Nature*, vol. 274, pp. 876–878, Aug. 31, 1978.
- [36] G. G. Gimmetstad and H. A. Gebbie, "Measurements of near-millimeter wave atmospheric attenuation in the temperature range 259K to 282K," *Int. J. Infrared Millimeter Waves*, vol. 3, pp. 77–82, Jan. 1982.
- [37] H. J. Liebe, "An atmospheric millimeter wave propagation model," NTIA Rep. 83-137, Dec. 1983.
- [38] D. T. Llewellyn-Jones and R. J. Knight, "Molecular absorption by atmospheric gases in the 100–1000 GHz region," in IEE Conf. Publ. No. 195, ICAP 81, pp. 81–83, 1981.
- [39] ———, "Measurements of water vapour absorption in the RAL untuned cavity," Rutherford Appleton Laboratory Rep. RL-82-051, July 1982.
- [40] L. I. Fedoseev and L. M. Koukin, "Comparison of the results of summer and winter measurements of atmospheric water vapor absorption of wavelengths 1.15 to 1.55 mm," *Int. J. Infrared Millimeter Wave*, vol. 5, pp. 953–963, July 1984.
- [41] N. I. Furashov, V. Yu. Katkov, and V. Ya. Ryadov, "On the anomalies in submillimeter absorption spectrum of atmospheric water vapor," *Int. J. Infrared Millimeter Waves*, vol. 5, pp. 971–984, July 1984.
- [42] L. M. Koukin, Yu. N. Nodrin, V. Ya. Ryadov, L. I. Fedoseev, and N. I. Furashov, "Determination of the contribution of water vapor monomers and dimers to atmospheric absorption from measurement data in the 1.15 to 1.55 mm band," *Radio Eng. Electron. Physics*, vol. 20, no. 10, pp. 7–13, Oct. 1975.
- [43] S. A. Clough, F. X. Kneizys, L. S. Rothman, and W. O. Gallery, "Atmospheric spectral transmittance and radiance: FAS-COD1B," *Proc. SPIE (Atmospheric Transmission)*, vol. 277, pp. 152–166, 1981.
- [44] V. J. Falcone, Jr. and L. W. Abreu, "Millimeter wave propagation modeling," *Proc. SPIE, (Millimeter Optics)*, vol. 259, pp. 58–66, 1980.
- [45] L. D. Duncan and R. C. Shirkev, "EOSAEL 82: library of battlefield obscuration models," *Opt. Eng.*, vol. 22, pp. 20–23, Jan./Feb. 1983.
- [46] H. J. Liebe and G. G. Gimmetstad, "Calculation of clear air EHF refractivity," *Radio Sci.*, vol. 13, pp. 245–251, Mar./Apr. 1978.
- [47] H. J. Liebe, "Modeling attenuation and phase of radio waves in air at frequencies below 1000 GHz," *Radio Sci.*, vol. 16, pp. 1183–1199, Nov./Dec. 1981.
- [48] ———, "Atmospheric EHF window transparencies near 35, 90, 140, and 220 GHz," *IEEE Trans. Antennas Propagat.*, vol. AP-31, pp. 127–135, Jan. 1983.
- [49] K. C. Allen and H. J. Liebe, "Tropospheric absorption and dispersion of millimeter waves," *IEEE Trans. Antennas Propagat.*, vol. AP-31, pp. 221–223, Jan. 1983; Errata: *IEEE Trans. Antennas Propagat.*, vol. AP-31, p. 1004, Nov. 1983.
- [49] N. E. Gaut and E. C. Reitenstein, III, "Interaction model of microwave energy and atmospheric variables," *Environmental Research and Technology, Inc.*, Tech. Rep. 13, Feb. 17, 1971.
- [50] J. T. Houghton and S. D. Smith, *Infrared Physics*. Oxford, England: Clarendon, 1966.
- [51] J. D. Kraus, *Radio Astronomy*. New York: McGraw-Hill, 1966, p. 98.
- [52] D. P. Rice and P. A. R. Ade, "Absolute measurements of the atmospheric transparency at short millimetre wavelengths," *Infrared Phys.*, vol. 19, pp. 575–584, 1979.
- [53] W. A. Traub and M. T. Sher, "Theoretical atmospheric transmission in the mid- and far-infrared at four altitudes," *Appl. Opt.*, vol. 15, pp. 364–377, Feb. 1976.
- [54] C. C. Zammit and P. A. R. Ade, "Zenith atmospheric attenuation measurements at millimetre and sub-millimetre wavelengths," *Nature*, vol. 293, pp. 550–552, Oct. 15, 1981.
- [55] C. C. Zammit, R. E. Hills, and R. W. Barker, "Atmospheric emission and attenuation in the range 100 to 600 GHz measured from a mountain site," *Int. J. Infrared Millimeter Waves*, vol. 3, pp. 189–203, 1982.
- [56] E. K. Smith, "Centimeter and millimeter wave attenuation and brightness temperature due to atmospheric oxygen and water vapor," *Radio Sci.*, vol. 17, pp. 1455–1464, Nov./Dec. 1982.
- [57] R. J. Hill, R. S. Lawrence, and J. T. Priestley, "Theoretical and computational aspects of the radio refractive index of water vapor," *Radio Sci.*, vol. 17, pp. 1251–1257, Sept./Oct. 1982.
- [58] G. D. Thayer, "An improved equation for the radio refractive index of air," *Radio Sci.*, vol. 9, pp. 803–807, Oct. 1974.
- [59] J. S. Owens, "Optical refractive index of air. Dependence on pressure, temperature, and composition," *Appl. Opt.*, vol. 6, pp. 51–58, 1967.
- [60] R. J. Hill, S. F. Clifford, and R. S. Lawrence, "Refractive-index and absorption fluctuations in the infrared caused by temperature, humidity, and pressure fluctuations," *J. Opt. Soc. Amer.*, vol. 70, pp. 1192–1205, 1980.
- [61] R. J. Hill and S. F. Clifford, "Contribution of water vapor monomer resonances to fluctuations of refraction and absorption for submillimeter through centimeter wavelengths," *Radio Sci.*, vol. 16, pp. 77–82, Jan./Feb. 1981.
- [62] A. J. Kemp, J. R. Birch, and M. N. Afsar, "The refractive index of water vapour: a comparison of measurement and theory," *Infrared Phys.*, vol. 18, pp. 827–833, 1978.
- [63] S. M. Rytov, *Introduction to Statistical Radiophysics*. Moscow, USSR: Nauka, 1966.
- [64] L. Chernov, *Wave Propagation in a Random Medium*. New York: Dover, 1967.
- [65] V. I. Tatarski, *Wave Propagation in a Turbulent Medium*. New York: McGraw-Hill, 1961.
- [66] R. L. Fante, "Electromagnetic beam propagation in turbulent media," *Proc. IEEE*, vol. 63, pp. 1669–1692, Dec. 1975.
- [67] R. S. Lawrence and J. W. Strohbehn, "A survey of clear-air propagation effects relevant to optical communications," *Proc. IEEE*, vol. 58, pp. 1523–1545, Oct. 1970.
- [68] H. B. Janes, M. C. Thompson, Jr., and D. Smith, "Tropospheric Noise in Microwave Range-Difference Measurements," *IEEE Trans. Antennas Propagat.*, vol. AP-21, pp. 256–260, Mar. 1973.
- [68] M. C. Thompson, Jr., L. E. Wood, H. B. Janes, and D. Smith, "Phase and Amplitude Scintillations in the 10–40 GHz band," *IEEE Trans. Antennas Propagat.*, vol. AP-23, pp. 792–797, Nov. 1975.
- [69] W. A. Flood, "Overview of near-millimeter wave propagation," *Proc. SPIE, (Millimeter Optics)*, vol. 259, pp. 52–57, 1980.
- [70] R. W. McMillan, R. A. Bohlander, G. R. Ors, R. J. Hill, and S. F. Clifford, "Millimeter wave atmospheric turbulence measurements: preliminary results and instrumentation for future measurements," *Opt. Eng.*, vol. 22, pp. 32–39, Jan./Feb. 1983.
- [71] J. T. Priestley and R. J. Hill, "Measuring high frequency humidity, temperature, and radio refractive index in the surface layer: Simultaneous observations with Lyman-alpha and near infrared hygrometers, a refractometer, and fine-wire thermometers," accepted for publication in *J. Atm. Ocean Technol.*, 1985.
- [72] S. F. Clifford, G. M. B. Bourcius, G. R. Ors, and M. A. Ackley, "Phase variations in atmospheric optical propagation," *J. Opt. Soc. Amer.*, vol. 61, pp. 1279–1284, 1971.
- [73] S. F. Clifford and J. W. Strohbehn, "The theory of microwave line-of-sight propagation through a turbulent atmosphere," *IEEE Trans. Antennas Propagat.*, vol. AP-18, pp. 264–274, Mar. 1970.
- [74] S. F. Clifford and R. J. Latatis, "Mutual coherence function for line-of-sight microwave propagation through atmospheric turbulence," *Radio Sci.*, accepted for publication, Jan. or Feb. 1985.
- [75] R. W. Lee and J. C. Harp, "Weak scattering in random media with applications to remote probing," *Proc. IEEE*, vol. 57, pp. 375–406, Apr. 1969.
- [76] S. F. Clifford, "Temporal-frequency spectra for a spherical wave propagating through atmospheric turbulence," *J. Opt. Soc. Amer.*, vol. 61, pp. 1285–1292, Oct. 1971.
- [77] R. S. Cole, K. L. Ho and N. D. Mavroukoulakis, "The effect

- of the outer scale of turbulence and wavelength on scintillation fading at millimeter wavelengths." *IEEE Trans. Antennas Propagat.*, vol. AP-26, pp. 712-715, Sept. 1978.
- [78] R. A. Bohlander, R. W. McMillan, D. M. Guillon, R. H. Platt, R. J. Hill, S. F. Clifford, J. T. Priestley, R. E. Cupp, R. Olsen, B. E. Rishel, and R. Okrasinski, "Millimeter wave transmission fluctuations due to snow," to be published in *Proc. Snow Symp. IV*, U.S. Army Cold Regions Research and Engineering Laboratory, Hanover, NH, Aug. 1984.
- [79] N. D. Mavroukoulakis, K. L. Ho, and R. S. Cole, "Temporal spectra of atmospheric amplitude scintillations at 110 GHz and 36 GHz," *IEEE Trans. Antennas Propagat.*, vol. AP-26, pp. 875-877, 1978.
- [80] F. C. Medeiros Filho, D. A. R. Javasuiva, and R. S. Cole, "Spectral density of amplitude scintillations on a 55 GHz line of sight link," *Electron. Lett.*, vol. 17, pp. 25-26, Jan. 3, 1981.
- [81] F. C. Medeiros Filho, D. A. R. Javasuiva, R. S. Cole, and C. G. Helms, "Spectral density of millimeter wave amplitude scintillations in an absorption region," *IEEE Trans. Antennas Propagat.*, vol. AP-31, pp. 672-676, July 1983.
- [82] R. T. Ott and M. C. Thompson, Jr., "Atmospheric amplitude spectra in an absorption region," *IEEE Trans. Antennas Propagat.*, vol. AP-26, pp. 329-332, 1978.
- [83] A. S. Gurvich, "Effect of absorption on the fluctuation in signal level during atmospheric propagation," *Radio Eng. Electron. Phys.*, vol. 13, no. 11, pp. 1687-1694, 1968.
- [84] A. O. Izvumov, "Amplitude and phase fluctuations of a plane monochromatic submillimeter wave in a near-ground layer of moisture-containing turbulent air," *Radio Eng. Electron. Phys.*, vol. 13, no. 7, pp. 1009-1014, 1968.
- [85] N. A. Armand, A. O. Izvumov, and A. V. Sokolov, "Fluctuations of submillimeter waves in a turbulent atmosphere," *Radio Eng. Electron. Phys.*, vol. 16, no. 1, pp. 15-19, 1971.
- [86] M. B. Kanevskii, "The problem of the influence of scintillation on amplitude fluctuations of submillimeter radio waves in the atmosphere," *Izv. VUZ. Radiofizika*, vol. 16, no. 1, pp. 147-149, 1973.
- [87] F. C. Medeiros Filho, D. A. R. Javasuiva, and R. S. Cole, "Probability distribution of amplitude scintillations on a line of sight link at 36 and 55 GHz," *Electron. Lett.*, vol. 17, pp. 393-394, June 11, 1981.
- [88] G. A. Andreyev, V. A. Golunov, A. T. Ismagulov, V. V. Parshikov, B. A. Rozanov, and A. A. Tarvigin, "Intensity and angle of arrival fluctuations of millimetric radio waves in a turbulent atmosphere," in *Proc. Anglo-Soviet Seminar on Atmospheric Propagation at Millimetre and Submillimetre Wavelengths* (Institute of Radioengineering and Electronics, Moscow, USSR, Nov. 28-Dec. 3, 1977).
- [89] H. T. Yura, K. G. Barthel, and W. Buchtemann, "Rainfall induced optical phase fluctuations in the atmosphere," *J. Opt. Soc. Amer.*, vol. 73, pp. 1574-1580, Nov. 1975.
- [90] R. M. Manning, F. L. Merat, and P. C. Gaspar, "Theoretical investigations of millimeter wave propagation through a turbulent atmosphere," *Proc. SPIE (Millimeter Wave Technology)*, vol. 337, pp. 67-80, 1982.

OPTICAL TESTS OF QUASI-OPTICAL
COMPONENTS FOR THE MM REGION

F-5-4

D. A. Simms, A. McSweeney, R. A. Bonlander
Engineering Experiment Station
Georgia Institute of Technology
Atlanta, Ga. 30332

Abstract

The need for various components in millimeter-submillimeter instrumentation has led us to an investigation of several quasi-optical techniques in this wavelength region. Results of studies of laminated TPX lens material, Eccosorb, an efficient quarter wave plate at 225 GHz, and metal grid polarizing beam splitters are presented.

Quarter Wave Plate for a 225 GHz Source

The efficiency of a sapphire quarter wave plate for a 225 GHz source depends primarily on the solution of two general problems:

- (1) a need for anti-reflection coating; the average refractive index of sapphire is 3.24 [1] and for the case of a thick parallel plane crystal this value corresponds to a high single surface reflectivity of 30 %.
- (2) The birefringent optical property $\Delta n = n_o - n_e$ of the crystal must be determined at 225 GHz to establish the plate thickness.

Initial far-infrared laser measurements at $\lambda = 1217 \mu\text{m}$ (244 GHz) were performed on a plane parallel plate of sapphire crystal cut with its optic axis parallel to the plate faces. The crystal thickness, $d = 5.00 \text{ mm}$ was such that the plate was close to a fifth order quarter wave plate at 225 GHz, based on values of n_o and n_e extrapolated from previously determined values for frequencies greater than 600 GHz [1-3]. The laser measurements indicated a significant reduction in reflection losses obtained with films of Mylar (TM, DuPont), $\bar{n} = 1.7$.

The difficulty in constructing such coatings is in eliminating the formation of air layers or pockets between the crystal substrate and film. The air layers were satisfactorily removed by first cleaning the surfaces carefully and then pressing the Mylar to the crystal. Both films were held in place with neoprene gaskets and clamps near the outer edge of the plate. The spacing between the Mylar and sapphire was then evacuated and sealed. With this method a maximum back reflectivity of about 1.3% was achieved at 225 GHz.

To determine the value of Δn , measurements were made of the effect of the sapphire plate on plane polarized radiation. The laser was used and its frequency, 244 GHz was sufficiently close to 225 GHz that the change in Δn between the two frequencies was negligible. Significant deviation from quarter wave plate conditions were expected at the laser frequency. The ellipticity of the polarized radiation resulting from two passes through the sapphire plate was determined and

compared with theoretically calculated changes in polarization for various Δn . The value $\Delta n = 0.345$ best fit the measurements and is in quite good agreement with extrapolations from previous results [1-3].

Based on this value of Δn , a sapphire quarter wave plate was constructed with a plate thickness of 4.08 mm. Reflectivity and ellipticity measurements similar to those performed with the FIR laser were made with an Extended Interaction Oscillator at the frequency 225 GHz. It was found that 99 % of the radiation after two transits through the quarter wave plate had a polarization orthogonal to the input polarization.

Lens Material for a 215 GHz Radiometer

In the course of designing and fabricating a horn-lens antenna for a 215 GHz radiometer, it was determined that absorption losses by the lens material Rexolite were substantially higher at 215 GHz than at lower frequencies [4,5]. Rexolite, a cross linked polystyrene, has been a popular choice for lenses used around 90 GHz [6]. However, comparison transmission/insertion loss measurements with a far-infrared optically pumped laser have shown that TPX or poly(4-methylpentene-1) gives much less absorption throughout the far-infrared region. Results of these laser measurements are given in Table I.

TPX is clear, slightly amber in color, and has a refractive index at millimeter wavelengths which is close to that in the visible spectrum [7,8]. Although TPX is not as rigid a material as Rexolite, there are no serious problems in machining. Some difficulty does arise with limitations in the sizes of available TPX bulk stock. Extruded plate stock is only available in thicknesses up to one inch (widths up to 18 inches) and extruded rods up to four inches in diameter. The present application required a lens thickness of 1.4 inches and initially it was felt that a strong adhesive with low optical absorption (or reflection) would be sufficient. Measurements were made of the transmission at 225 GHz of TPX samples laminated with various adhesives. The excellent optical properties of Horland Optical Adhesive 61 made it the best choice, but reinforcement of the bond was necessary for machining. This was accomplished with dowel rods of TPX. Two TPX sheets were machined flat, polished, and glued. Polishing the surfaces was an attempt to minimize interface reflections by making the adhesive layer very thin. The dowel rods were cooled to -55°C at which temperature their diameters were smaller by at least 0.003 inch. These were inserted into holes in the laminated TPX sheets and allowed to expand to a very tight fit. After this procedure machining of the lens was successfully completed.

Eccosorb Brewster Angle Measurements

Eccosorb (TM, Emerson and Cummings) is a material which has been used to make very compact black body radiators [9]. In these, the high absorption of the material is utilized by viewing the source at Brewster's angle and thereby reducing reflections. In the interest of extending the use of this material to frequencies above 183 GHz, new measurements of the reflection properties have been made.

Determination of the Brewster angle for Eccosorb at 163, 254, 570.5, and 1217 μm were performed with a far-infrared laser. With the equipment arrangement shown in Figure 2 the reflectance of plane polarized radiation from Eccosorb was measured for several values of θ in the vicinity of the Brewster angle θ_B .

The Eccosorb was specially molded into a flat sided disc of diameter 2 inches which could be easily interchanged with a standard 100% reflector. The polarizer was oriented to pass radiation linearly polarized in the plane of incidence to insure maximum penetration into the Eccosorb at θ_B . Results of the measurements are given in Table 2.

Metal Grid Polarizing Beam Splitter*

A polarizing beam splitter is often an important component in quasi-optical designs for duplexers, duplexers, Fabry-Perot type filters, or Fourier transform spectrometers. One type is made by wrapping thin wires tightly around a frame [10], but these are difficult to make accurately, are fragile and costly. An alternate kind is made by photo-etching the grid pattern on a thin dielectric grid substrate. The present work has been an attempt to extend the state of the art in this medium, so that larger apertures would be available and good performance obtained at high frequencies. Aluminum grids on Mylar (TM, Dupont) have been constructed with the following parameters: strip and gap widths 5 μm , film thickness 6 μm , and apertures up to 100 mm diameter. Preliminary tests with radiometers at frequencies near 200 GHz have indicated better than 99% polarization efficiency and less than 1% loss. Fourier spectrometric measurements will be made and compared with theory.

Acknowledgements *Thanks are due to R. E. Forsythe of UT/EES for measurements and to G. Lamb of the Goddard Space Flight Center for guidance on photo-etching.

Support for this work was provided by the U.S. A.F. Geophysics Lab., U.S.A.R.O., U.S. Army Metrology and Calibration Center, U.S. Army Night Vision Lab., and U.S. Naval Research Office.

References

- [1]. E. E. Russel and E. E. Bell, J. Opt. Soc. Am., 57, 543-4 (1967).
- [2]. E. V. Lowenstein, D. R. Smith, and R. L. Morgan, Appl. Opt., 12, 398-405, (1973).
- [3]. S. Roberts and D. D. Coon, J. Opt. Soc. Am., 57, 1023-29 (1962).
- [4]. M. L. Foster, R. E. Forsythe, J. M. Welch, J. M. Schuchardt, Technical Report, GT/EES Contract No. DAAK70-c-0108, August, 1980.

- [5] O. A. Simpson and R. A. Bohlander, Monthly Report No. 17, G. T. Contract DAAK70-C-0108, Feb., 1981.
- [6] J. M. Newton, D. J. Kozakoff, and J. M. Schuchardt, 15th Symposium on Electromagnetic Windows, Georgia Institute of Technology, June, 1980.
- [7] G. W. Chantry, H. M. Evans, J. W. Fleming, and H. A. Gebbie, Infrared Physics 9, 31-33 (1969).
- [8] M. N. Afsar, J. Chamberlain, and G. W. Chantry, IEEE Trans. Instrum. Meas. IM-25, 290-4 (1976) and J. Chamberlain, J. Haigh, M. J. Hine, Infrared Physics 11, 75-84 (1971).
- [9] R. Iwasaki, NELC, November, 1976.
- [10] P. A. R. Ade, A. E. Costley, C. T. Cunningham, C. L. Mok, G. F. Neill, and J. J. Parker, Infrared Physics 19, 599-601 (1978).

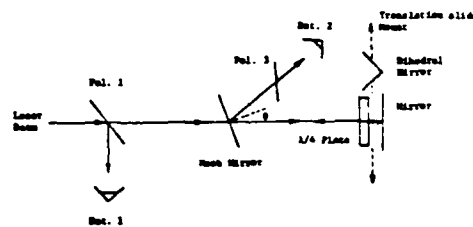


Fig. 1. Experimental arrangement for ellipsicity measurement. The angle $\theta = 10^\circ$; POL., polarizer; Det., detector.

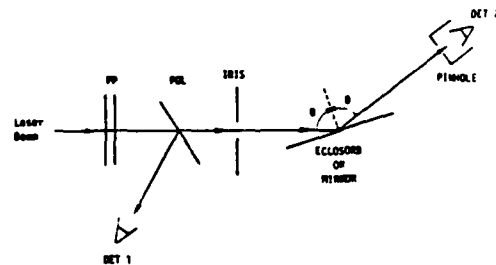


Figure 2. Experimental arrangement: FP, Fabry-Perot interferometer; POL, polarizer; DET, detector.

TABLE I

SAMPLE	MEASURED THICKNESS (cm)	λ (μm)	CALCULATED REFLECTANCE	MEAN TRANSMISSION	ABSORPTION COEFF. (cm^{-1})
Resonance	2.423	570.5	0.100	0.187	0.65
Resonance	2.405	1217	0.100	0.566	0.19
TPX	2.418	163	0.068	0.137	0.74
TPX	2.418	570.5	0.068	0.697	0.12
TPX	2.398	1217	0.068	0.936	0.00

TABLE II

λ (μm)	REFLECTANCE	θ° Brewster
163.0	0.04	80.0
254.0	0.02	80.0
570.5	0.12	70.0
1217.0	0.10	70.0

END

DATE

FILMED

7-88

Dtic